THE UNIVERSITY OF CHICAGO

SYNTHESIS AND APPLICATIONS OF SILICON NANOWIRES FOR STUDYING BIOINTERFACES

A DISSERTATION SUBMITTED TO

THE FACULTY OF THE DIVISION OF THE PHYSICAL SCIENCES

IN CANDIDACY FOR THE DEGREE OF

DOCTOR OF PHILOSOPHY

DEPARTMENT OF CHEMISTRY

BY

YOUJIN LEE

CHICAGO, ILLINOIS

JUNE 2020

Dedication

I dedicate my dissertation work to my grandmother, Lee BokHee yeosa (1920 – 2019). She was a true educator, serving Ewha Girls' High School for 37 years and living an exemplary life of seeing the best side of everyone. Her love and unconditional trust in me has empowered me throughout my life and academic journey. I will remember and live up to what she has shown me. 할머니의 가르침을 본받아 다른 사람을 사랑하는 삶을 살도록 노력할게요.

Table of Contents

List of Figures

List of Tables

Acknowledgments

I would like to thank my caring advisor, Professor Bozhi Tian, for being truly supportive about my success in my academic and future career. He gave me the freedom to pursue the research of my interest and reroute my research directions. He encouraged me to think independently and deeply about my research, while constantly reminding me to be positive and to “don’t worry”.

I was extremely lucky to have my two excellent collaborators/ research mentors, Dr. Yuxing Peng and Dr. David Wu, MD who guided me throughout my entire Ph.D. work. Dr. Yuxing devoted innumerous hours to solve various computational problems, advised me on image analysis, and thought me how to code and perform statistical analysis. Dr. David Wu gladly carved out time in his busy schedule to discuss and design both experiments and image analysis strategies. Every meeting with each of them was an intellectually stimulating and joyful interaction.

I would like to thank all of the other members of the Tian lab that I have overlapped with. Just to name a few: Dr. Johnny Zimmerman and Dr. Jaeseok Lee for providing me with mentorship in my junior years. Lingyuan Meng and Ellie Ostroff for showing reliable and pleasant teamwork in collaborating the multinucleated project. Dr. Hemi Rotenberg and Dr. Fei Pei for being great officemates. Finally, I would like to specifically thank Dr. Ramya Parameswaran and Dr. Andrew Phillips for our camaraderie and being the source of fun throughout the majority of my Ph.D.

I am thankful that I was able to join a wonderful cohort of Chemistry Ph.D. at the University of Chicago. I thank my roommate, Bodhi Vani, and my other female classmates,

Sarah Brown, Laura Watson, and Racheal Youngworth, and my first year office mate, Vlad Kamysbayev. I am grateful to have formed friendships with my Korean friends, Hyunki Kim, Hyosung Joo, Kiho Park, Injae Kim, Yechan Kwak, Sanghee Kim, and Dr. Donghyuk Suh. I would also like to thank my friends in Korea, Hong Kong, and other parts of the United States for encouraging me throughout my journey.

Lastly, I would like to thank my parents for their love, respect, and support. They have let me study abroad since I was fourteen years old and supported me in every possible way even from afar. I would like to thank my partner, Jacob Olshansky, for giving me moral support and being by my side through good times and bad. I would also like to thank him for extensively proof reading all my writing, including this very sentence.

Abstract

Given its interdisciplinary nature, nanomaterials research is conducted in a virtuous cycle. In this cycle, new materials are first synthesized, then characterized, and fit into and evaluated for appropriate applications, which in turn inform what type of new materials should be synthesized. Recently, with the advent of big data and machine learning, researchers are utilizing computational methods to aid in all aspects of this cycle. While covering all four aspects of the nanomaterials research cycle, my PhD work focuses specifically on kinked silicon nanowires with the aim of developing probes for bio-nano interfaces.

Prior to introducing my PhD work, to give context and motivations, I outline how nanomaterials are used to sense and modulate biological interfaces, such as to read the signals from neuronal cells and to pace cardiac cells. While focusing on semiconducting nanomaterials' applications in photo-induced bio-modulations, I point out the unique properties of nanomaterials, which make them suitable for such applications. In the remaining part of the thesis, I introduce my two main projects, in which I (1) synthesized multinucleated kinked silicon nanowires, and (2) developed a method of tracking the longitudinal rotation of a kinked silicon nanowire.

In my synthesis project, I devise a way to grow ultra thin silicon nanowire branches by inducing the main nanowire catalysts to diffuse down the nanowire sidewall. More interestingly, I demonstrate how these thin nanowire branches are restructured to spheroids *via* an Ostwald ripening-like process. This new synthetic strategy will allow one to synthesize semiconducting nanowires with multiple regions of increased surface area along the nanowire long axis, opening the door to a variety of applications.

In my tracking method development project, I first introduce the idea of utilizing the arm of the kinked nanowire to track the nanowire's longitudinal orientation, and thus rotational

motion along its long axis (i.e. rolling). Then, I explain the newly developed image analysis algorithms that can accurately and efficiently track the longitudinal orientation of the nanowire undergoing rolling. Finally, I demonstrate the use of the method in studying the nanowire interacting with a mammalian cell, suggesting the method's ability to reflect different types of biological behavior.

Collectively, these projects highlight all aspects of the cycle of nanomaterials research. I suggest how the multinucleated nanowire can serve as a more "complete" probe for tracking longitudinal rotation tracking.

1 Introduction

Nanomaterials research has grown tremendously in recent years owing to its potential to impact numerous industries from alternative energy technologies to medical applications. Nanomaterials research is inherently interdisciplinary, drawing on expertise from the traditional disciplines of chemistry, physics, biology, and engineering. As the field matures, new expertise and techniques have emerged to address the challenges of these unique materials. A broadly defined cycle of research has developed that connects the various facets of nanomaterials research. These include the synthesis and fabrication of nanomaterials, the characterization of these new nanomaterials, and finally the applications of these nanomaterials. These three tenets of nanomaterials research feed back into each other to aid in the development of novel nanomaterials with desired applications. This interplay is also supported by computational methods to quantitatively process the experimental data and to theoretically study the aforementioned areas (Figure 1-1).

In my Ph.D. work, I focus on the study of silicon (Si) nanowires, which are one-dimensional rod-like particles with nanometer-scale diameters and micrometer-scale lengths. My research is particularly focused on developing these materials for both probing and modulating biological systems. The potential implications of this research are broad, from better understanding biological systems on the nanoscale to providing clinically relevant tests. With these application goals in mind, my Ph.D. research took a broad approach, covering multiple aspects of the nanomaterials research cycle described above (synthesis, characterization, applications, and computation), while focusing specifically on the versatile materials system of Si nanowires.

In chapter 2, I give an overview of pertinent background information and provide some motivation for using nanomaterials to sense and modulate biological systems. I first outline different signaling mechanisms of living systems and how the signals are read out by traditional methods. Then, I discuss how nanomaterials can help overcome challenges of traditional sensing probes. I use Si-based nanomaterials to illustrate how nanoscale material properties are different from and advantageous compared to their bulk counterparts. I describe how these materials can be used to sense electrical, chemical, and mechanical information in biological systems. Next, I explain how nanomaterial-based devices can form tight interfaces with biological entities and expound on two distinct photo-induced biomodulation methods: photoelectrochemical and photothermal. I conclude the chapter by highlighting the importance of using free-standing nanomaterials for optical stimulation.

In chapter 3, I discuss my research efforts to access new and unique Si nanowire (SiNW) structures as well as synthetic mechanistic insights on their formation. First, I discuss how ultra-thin Si nanowires can be grown on a thick primary SiNW by inducing the catalyst's diffusion along the primary NW sidewall. Next, I describe how the ultra-thin SiNWs undergo conspicuous amounts of restructuring and offer my postulation on how the restructuring takes place. I showcase a variety of SiNW morphologies and offer insights on their synthetic control. Access to novel nanomaterial structures, such as the ones I describe, will give researchers new tools for developing nanomaterials applications.

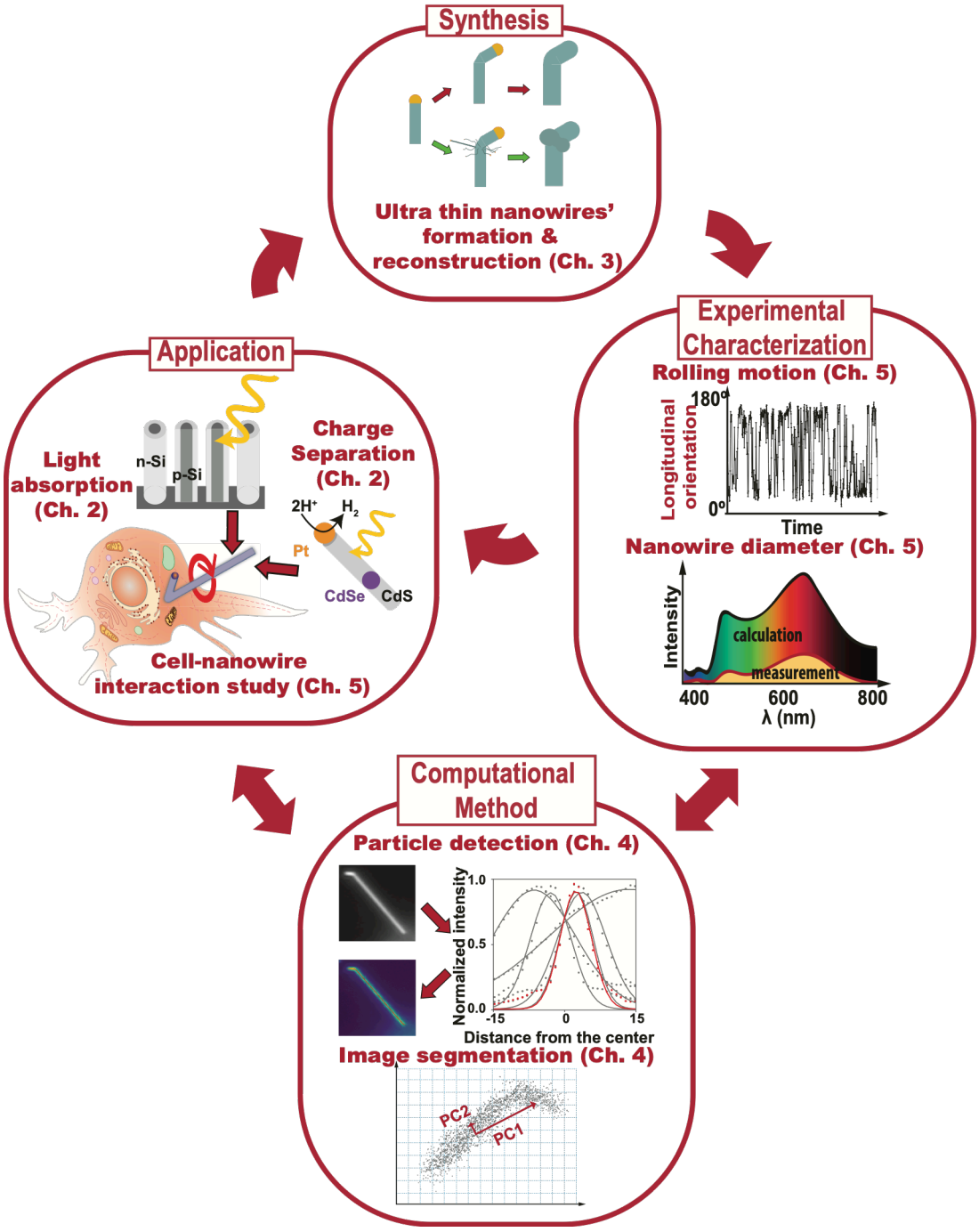

Figure 1-1. Overview of the Thesis. New synthetic method (top) can give rise to experimental methods (middle right). These experimental characterization methods can be applied for various studies (middle left). Computational methods (bottom) are needed for successful experimental characterization and are tailored to meet specific needs of an application. My PhD work includes synthetic study in ultra-thin nanowire formation and Si reconstruction (Chapter 3). I developed an experimental tool to track rolling motion of a nanoparticle and utilized scattering spectroscope to measure its diameter (Chapter 5). I developed image processing algorithms to process the data to track the rolling motion

(Figure 1-1 continued) (Chapter 4). The rolling tracker method was applied to study the interaction of a kinked-nanowire and a cell (Chapter 5). In the future, we look forward to incorporating the nanomaterial's ability to absorb light and charge separate for cell stimulation.

Switching gears, in Chapter 4 I present newly developed image analysis algorithms designed to improve identification and tracking of nanowires in a microscope. The first algorithm can resolve the true center of a nanomaterial that appears thicker than its physical size due to its highly scattering nature. The second algorithm segments the nanomaterial to its component parts. I explain the working principles by applying the algorithm to an optical image of a kinked-SiNW and identifying the NW's arm and main body. These image analysis techniques can be further extended to process nanomaterials of varying sizes and shapes. However, the current iteration is optimized to efficiently and reliable process the experimental data from the rotational tracking method presented in the subsequent chapter.

Finally, in Chapter 5 I introduce my newly developed experimental method that tracks the rolling motion of a SiNW. The rolling motion of nanomaterials can serve as a sensitive proxy to probe local microscopic environments. In my proof-of-concept demonstration of the method, I probe the interaction of the nanowire and a biological cell, as reflected in the nanowire's rolling dynamics. I find distinct dynamics when the cell is interacting vs. not interacting with the cell. This method can be used to yield insights into nano-mechanics in various biophysical and assembly processes.

In Chapter 6, I offer my perspectives on how the insights gained from my Ph.D. studies can contribute to nanomaterial sciences, especially in the context of bio-sensing and bio-modulation applications as overviewed in chapter 2.

2 Background

In this background chapter, I first explain the various signaling mechanisms by which biological processes function and how traditional methods have been sensing these processes (Section2.1). I explain the advantages of using Si-based materials and the importance of forming a strong nano-bio interface (Section2.2). I explore Si-based nano- and micro-scale devices that are used to sense electrical, biological, chemical, and mechanical signals in biological cells (Section2.3). I further introduce methods that cannot only sense but also modulate cellular electrical activities (Section 2.4). In the learning points sections, I explain the field effect transistors' working principle and the Debye screening phenomena.

2.1 Biological Processes and Traditional Methods

2.1.1 Sensing Electrical Signal

A primary goal of cellular biology has been to understand how cells process and use electrical, chemical, and biological signals both within cells (intracellular signaling) and between cells (intercellular signaling). In particular, electrical signaling is ubiquitous in biological cells. Cells that can generate electrical signals, specifically action potentials, are termed excitable cells and include muscle fibers that initiate contraction, and nerve cells, i.e. neurons, that transmit electrical signals to communicate. All cells, including the ones that are not excitable, have a membrane potential, which is established by a concentration difference of sodium and potassium ions between the cell membrane and extracellular matrix. For example, the resting membrane potential of excitable cells is typically -70 mV. During cell-to-cell communication, this membrane potential fluctuates, often with a rapid upward spike to about 40 mV followed by a rapid downward spike below past the resting potential of -70 mV. This phenomenon is known as an action potential, fired by the excitable cells.

The patch-clamp technique is a traditional electrophysiology tool used to record intracellular electrical currents. In this technique, a thin glass micropipette with a recording microelectrode inside is filled with an electrolyte and inserted into a cell. A reference electrode is inserted into the solution surrounding the cell and ionic currents are recorded between the electrodes. Even though the technique can yield high spatial resolution—up to single ion channel recording—with high signal-to-noise ratio, it has nontrivial setbacks, such as the highly invasive nature and spatial and temporal resolution trade-off.[1] For example, while decreasing the size of the micropipette is crucial for increasing the spatial resolution, small micropipettes will give high impedance between the micropipette and the cell interior, resulting in reduced temporal resolution as well as low signal-to-noise ratio.[2] Another set of techniques used for probing cellular electrical activities include voltage- and calcium-sensitive dyes, which display high temporal and spatial resolution.[3,4] The dye-based techniques however, suffer from challenges such as photobleaching, cytotoxicity from the dye, and differential dye loading efficiency.

In later sections, I explore how a Si-based nanomaterial that can sense and even register electrical signals from both individual cells and groups of cells can address the limitations of these traditional techniques.

2.1.2 Sensing Chemical and Biological Signals

Modulating biochemical and biophysical processes ideally requires a method to sense changes to these natural mechanisms. When designing sensor for chemical and biological signals, consideration should be given to the type of cellular regulation involved in the biological effect. For instance, if an induced change to cellular physiology is caused by an alteration of gene expression, this result could likely be assayed at the level of gene expression by quantifying changes in messenger RNA by methods such as real-time quantitative polymerase chain reaction

(RT-PCR) or RNA sequencing (RNA-Seq). Alternatively, if the modulated gene encodes for a protein, protein quantification could be used to quantify the effect induced on the cell. A widely used protein quantification method is Western blotting. There are more sophisticated proteomics methods such as stable isotope labeling with amino acids in cell culture (SILAC) and isobaric tags for relative and absolute quantitation (iTRAQ).[5] However, proteomics methods and Western blotting are typically destructive to the cell, which would not be suitable for many applications. Non-invasive methods for protein detection and quantification use fluorescently-labeled antibodies specific to proteins of interest. In this method, permeabilization and staining techniques allow for protein quantification without killing the cells. Nucleic acids can similarly be quantified using complementary nucleic acid hairpin structures containing a fluorescent dye and a quencher.[6,7] These probes exhibit turn-on fluorescence when the complementary nucleic acid sequence binds the probe and subsequently spatially separates the fluorophore and quencher, turning off Förster resonance energy transfer from the dye to the quencher, restoring fluorescence to the dye. A variety of small molecule fluorophores that have a specific interaction with an analyte, resulting in a detectable spectral change, can also be used for live-cell imaging. Calcium imaging using Fura-2 is a popular method to visualize calcium fluxes in live cells, which can be correlated to electrical activity.[8]

As cellular perturbations could affect only existing populations of biomolecules in the cell during the perturbation event, it is important to consider which populations a given assay actually measures and which are the relevant populations to interrogate. Many extracellular signals—e.g. soluble molecules, insoluble biopolymers, mechanical forces, temperature, and ion concentrations—are mediated by signal transduction pathways, and connect exterior cues to physiological changes inside the cell. When considering effects of cellular stimulation mediated

by signal transduction pathways, secondary messengers should be quantified using appropriate methods, as controls.

2.2 Silicon materials and Rational Designs

Silicon nanowires (SiNWs) are grown in a chemical-vapor-deposition (CVD) system via the vapor-liquid-solid (VLS) mechanism. First, gold nanoparticles (AuNPs) are deposited on a silicon (Si) wafer, which is placed in a CVD chamber at high temperature and low pressure. A Si precursor gas, silane (SiH_4) in my case, and a dopant precursor gas - either phosphine (PH_3) for n-type doping or borane (B_2H_6) for p-type doping - are introduced, which break down at high temperatures on the AuNPs surface. The gaseous Si atom dissolves in the AuNP, forming a Au-Si alloy. Once the Si concentration in the alloy reaches its maximum solubility, solid Si precipitates out at the alloy-Si substrate interface, nucleating SiNW growth. The precipitation allows more Si atoms to be dissolved in the AuNPs and leads to further growth of the SiNWs.

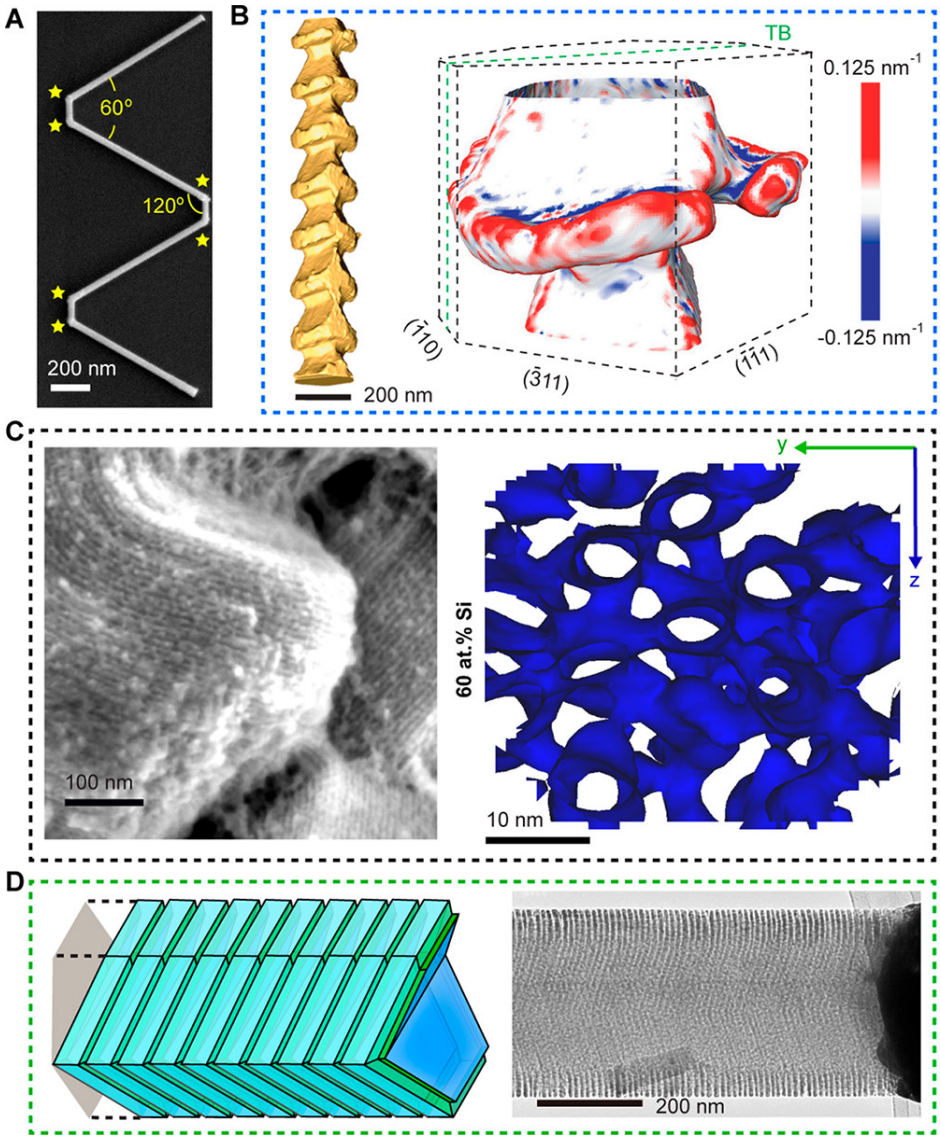

Figure 2-1. Various Si-based nanostructures. A. Scanning electron microscope (SEM) image of a SiNW with six 120 ° angle kinks (stars). B. Scanning transmission electron microscopy tomography of a spicule-like SiNW (left). 3D curvature map of an individual segment with concave (blue) and convex (red) surfaces. TB denotes twin plane. C. Mesoporous Si structure has a periodic assembly of SiNWs as shown in the SEM image (left) that is interconnected with microbridges as shown in the atom probe tomography (APT) isosurface images(right). D. A schematic diagram (left) and a transmission electron microscopy (TEM) image of an etched SiNW with porous sidewall grooves. Reprinted with permission from reference 9. 2018 American Chemical Society.

In this growth process, numerous parameters such as temperature, total pressure, gas composition, and pressure can be controlled, giving flexibility in synthesis. To synthesize thicker NWs, larger AuNPs are used. The length of the NWs is controlled by the growth time. To introduce a kink, the CVD reaction chamber is purged for 15 seconds by turning on the vacuum pump. The purge step introduces drastic pressure changes in the reaction chamber and destabilize the Au-Si alloy (Figure 2-1 A).[10] The abrupt decrease in pressure introduces a 120° turn at the SiNW-AuNP catalyst interface in the following steps: first, growth cease as the reactant concentration drops during the purge, next, new nucleation of Si occurs upon re-introduction of the reactant, from which SiNW will resume its growth. The particular angle is due to the fast growth direction switching from <112> to <110> orientation, and then back to <112>, which can be explained by thermodynamic stability. By throttling the pressure twice within a short growth interval, the SiNWs will develop two 120° kinks, effectively a forming a 60° angle joint.

Based on the dopant pattern imprinted along the NW during the VLS growth, SiNWs can be selectively etched to yield various morphologies along their long axis. Kim *et al*. modulated the p-type dopant level during the growth and selectively etched the doped region with hydrochloric acid post-synthesis (Figure 2-2).[11] In addition to varying the dopant concentration level, Au diffusion along the SiNW sidewall can also be controlled. Luo *et al.* embedded a periodic pattern of atomic Au by modulating the system pressure during the synthesis (Figure 2-1 B).[12]Subsequent potassium hydroxide etching selectively etched the non-Au diffused regions of the SiNW as the Au pattern acts as an etchant resist. Similarly, Fang *et al.* engraved parallel Au rings along the SiNW sidewalls with spacing as low as 5 nm (Figure 2-1 D).

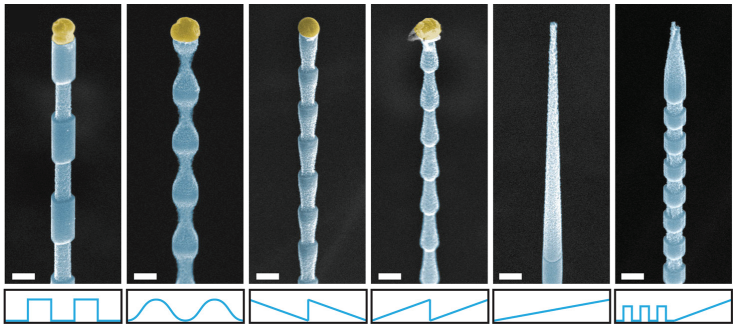

Figure 2-2. Various morphologies of SiNWs achieved with dopant modulation and dopant-dependent etching. Falsely colored SEM images (top) of the SiNWs of various diameters along their longitudinal axis (Au: yellow; Si: blue). N-type-doped regions of the NWs were etched by buffered hydrofluoric acid. Scale bars: 200 nm, Pressure profiles (bottom) of n-type dopant precursor gas corresponding to the final 1 μm growth of above NW. Adapted with permission from reference 11. 2017 American Chemical Society.

In addition to the VLS longitudinal growth, SiNWs can also grow radially via the vapor-solid (VS) mechanism. Through the VS deposition of shell, core-shell SiNW structure can be achieved, reminiscent of core-shell semiconducting nanocrystals. For example, Tian *et al.* synthesized p-i-n coaxial SiNWs comprising of a p-type core, an intrinsic inner shell, and an n-type outer shell.[13] Here, p-type SiNW cores were grown by the VLS mechanism. Then, the shells were deposited at a higher temperature to prevent further axial growth of the NW. This one-dimensional p-i-n nanostructure has shown effective charge separation upon light absorption, making it suitable as a photovoltaic material. The concept of nanomaterial-enabled charge separation and the application of the p-i-n SiNW are discussed in section2.4.

Apart from SiNWs, Jiang *et al.* developed a nanoporous Si mesostrcture (Figure 2-1 C). This nanoporous Si matches the mechanical properties of soft biological cells and tissue and exhibits a Young's modulus of 1.84 GPa, which is approximately two orders of magnitude lower than bulk Si with a Young's modulus of 160 GPa. The material can be made softer by immersing it in phosphate buffered saline solution, which results in a Young's modulus of 0.41 GPa,

comparable to hydrated collagen fibers.[14] Such matching of mechanical property is critical for biological application (as introduced in section 2.3, 2.4) because (1) it better represent the cellular environment when used as an in-vitro support to grow cells and (2) is less likely to cause an autoimmune response when integrated in biological systems.

2.3 Sensing Probes

2.3.1 Electrical Signal and FET

2.3.1.1 Learning point 1: basics of transistor and field effect transistor

Transistors are semiconductor devices that can gate electronic signals dependent on input signals. First practically implemented by John Bardeen, Walter Brattain, and William Shockley in 1947, they have become an integral part of circuits found in almost all modern electronic devices.[15] Transistors usually have at least three terminals and are made of Si. Transistors are categorized into two groups: current-controlled bipolar junction transistors (BJTs) and voltage-controlled field-effect transistors (FETs). BJTs use both holes and electrons for conductance, while FETs utilize either solely electrons or solely holes. For this chapter, we will focus on the FET, which is more common in practice.

FETs consist of three terminals: the source, the gate, and the drain. Charge carriers—either electrons or holes—flow through a channel from the source to the drain. The carrier density, or the conductivity, of the channel is modulated by the electric field generated by the voltage across the gate and the source (see Figure 2-3).

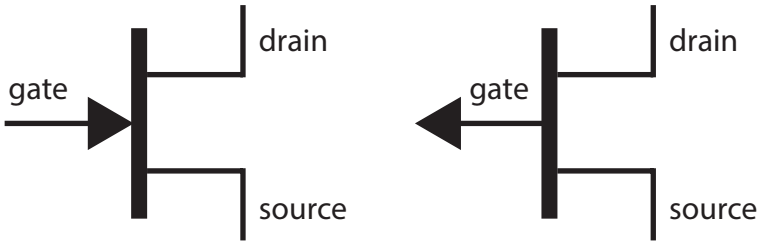

Figure 2-3. Schematic electric symbol diagram of FET. FET with n-channel (left) and FET with p-channel (right) comprising three terminals: drain, source, and gate.

FETs are sensitive to small voltage differences across the gate and source, so they can significantly amplify signals in the current readout. With the same device principle, sensing of electrical/chemical/biological signal can be done on a much smaller scale. For such applications, SiNWs have been an excellent material due to their one-dimensional structure, nano-scale size comparable to biological systems, and synthetic tunability. Compared to a bulk or planar material, one-dimensional SiNWs have a high surface-to-volume ratio. The one-dimensional nature of NWs make them intrinsically sensitive since any signal imposed on the NW surface will translate to the entirety of its volume as opposed to being attenuated by the large volume in a planar FET channel. For example, a heavily doped SiNW was used as a channel in a planar nanowire FET (NW-FET) (Figure 2-4).

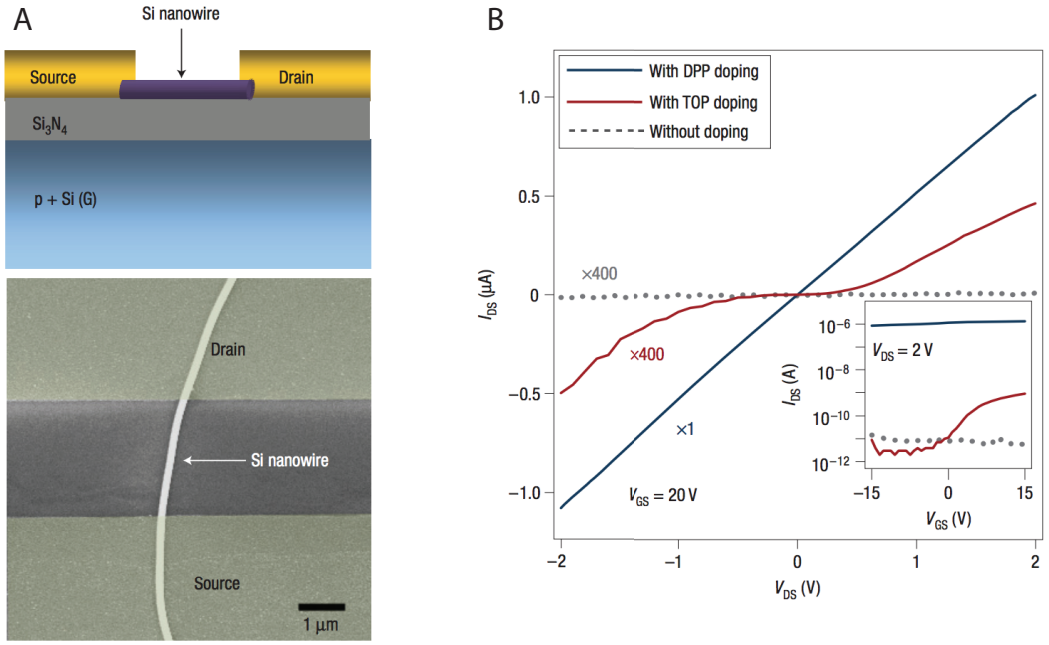

Figure 2-4. A back-gated SiNW-based FET. A. Schematics diagram of the device, where a SiNW is used as a channel, silicon nitride as an insulating layer, and a Si wafer as a back-gating material (top). Falsely colored SEM image of the device (bottom). B. Source-drain current versus source-drain voltage measured with FET devices with an undoped and doped SiNW. Different precursors were used for monolayer doping: diethyl 1-propylphosphonate (DPP) and trioctylphosphine oxide (TOP). Adapted with permission from reference 16. 2008 Nature Publishing Group.

To quantitatively explain the properties of NW-FETs, we must understand the relationship between the change in conductance (ΔG) and the change in the electrostatic potential ($\Delta\varphi_{Si}$) (Equation 2-1). A comprehensive derivation is provided by Gao *et al.*[17]

$$\Delta G = q\mu \int_0^R 2\pi r \Delta p dr \qquad \textbf{(Equation 2-1)}$$

Here, q is the elementary charge; μ, the carrier mobility; and r, the distance from the NW center. R is the NW radius and p is the majority carrier density.

In one limiting case, either when the NW radius is much less than the Debye length (defined in section 2.3.2.1), or when the dopant concentration of the NW is very low, the conductance change varies exponentially with surface charge change. (Equation 2-2)

$$\Delta G = q\mu\pi R^2 p\left[e^{-q\Delta\varphi_{Si}/K_B T} - 1\right] \quad \textbf{(Equation 2-2)}$$

In the other limiting case, when the NW is heavily doped or thick, where the NW radius is much greater than the Debye length, the conductance change depends linearly on the change in surface charge. (Equation 2-3)

$$\Delta G = 2\pi R p \lambda_D \frac{q^2 \Delta\varphi_{Si}}{K_B T} \qquad \textbf{(Equation 2-3)}$$

Because the conductance change responds to changes in the surface charge differently based on the NW dopant level, NW dopant modulation can further localize the detection area. For example, the p-n junction of an axially-doped, kinked NW was used as a point-like FET detector.[18]

2.3.1.2 FET principal applied to sensing mechanism

This dopant-level-dependent response property along with established surface modification techniques makes SiNWs an excellent material to be used as a high-sensitivity nano-biosensor in FET-like devices. The native silicon oxide layer on the NW surface can be modified to transform NW-based FET devices into biosensors that can detect chemical and biomolecules. For example, n-doped SiNWs functionalized with amines and oxide species were used in a nanosensor to detect the environment's pH as well as protein binding.[19] In this example, 3-aminopropyltriethoxysilane (APTES) ligated on the SiNWs' surface will affect surface charge state based on the protonation and deprotonation based on the pH change of the environment. Therefore, changes in pH regulate the surface charges of APTES-modified SiNWs,

which enables it to act as a chemical gate. In summary, a pH change is read out as a change in the current flow through the NW nanosensor. Surface modification techniques that enable biomolecule detection will be further explored in section 2.3.2.

2.3.1.3 Extracellular signal recording

SiNW-FETs can be used for extracellular field potential sensing. Unlike its bulk counterpart, nanometer thick SiNWs are flexible and can be made into flexible devices to interface with biological systems that typically have low Young's moduli. Cohen-Karni *et al*. fabricated a multiplexed SiNW-FET array that can resolve a propagation of extracellular potential spikes in a cardiomyocyte monolayer.[20] The recording was possible due to its flexible and robust interface between the NW-FET device and cells, as well as the comparable length scales of the NW and the biological system. To achieve a high signal-to-noise ratio, a strong interface between the device and biological sample is crucial. Further discussion about the FET-biological sample interfacing will continue in section 2.4.1.

2.3.1.4 Intracellular signal recording

Compared to extra cellular potentials, intracellular signals are harder to measure, since the probe has to be inserted into the cell. Extracellular sensors cannot detect intracellular signals as the lipid membrane has electrical resistance and capacitance, thus acting as an electrical barrier. Intracellular electric signal recording can contain rich information and can help reveal sub-cellular information flow and cell physiology.

A traditional method, such as the patch clamp technique, is mechanically invasive and their operation and set up are not trivial. NW-FET probes, on the other hand, present a less invasive alternative for such measurements. Tian *et al*. integrated a multiply-kinked SiNW into a metal-polymer based support to form a flexible NW-FET device (Figure 2-5).[21] The probing tip has two 120° kinks that are only about 160 nm apart. This pointy morphology facilitates the

insertion of the probe into the cell and is less invasive due to its small penetration cross section. In addition, the probe was coated with a phospholipid bilayer that was critical for successfully inserting the NW through the membrane to access the intracellular region. The kinked NW had a varying dopant concentration: a lightly doped region was sandwiched between heavily doped arms. In this case, the heavily doped arms acted as the source and drain terminals while the lightly doped region in between them acted as a gate. The point-like detection area is advantageous as it increases both the signal-to-noise ratio of the FET device and the spatial resolution. The localization was possible because the surface-charge-dependent FET conductance change is sensitive to local dopant level. The device was able to read the intracellular potential while being minimally destructive for the cell, from both chemical and mechanical standpoints.

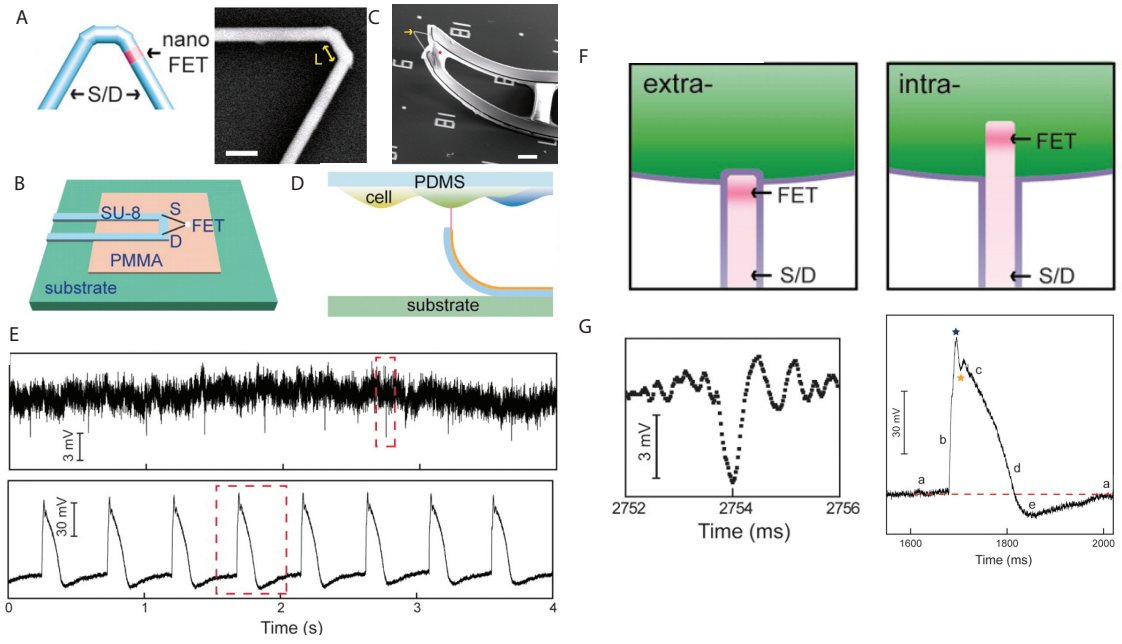

Figure 2-5. 3D kinked SiNW probes and electrical recording of cardiomyocytes. A. Schematic diagram of 60_ doubly kinked nanowire (left) and the SEM image of a cis-doubly kinked nanowire (right). L is the distance between the two kinks. Scale bar: 200 nm, B. a schematic diagram of the fabricated device. Poly(methyl methacrylate) (PMMA) was used as a sacrificial layer and SU-8 microribbons as a flexible support. C. SEM image of the device.

(**Figure 2-5 continued)** Yellow arrow points to the NW-FET and the pink star is drawn on the SU-8 support. D. Schematic diagram setups for recording beating cardiomyocytes on polydimethylsiloxane (PDMS) (left) E. electrical beating readout for extracellular recording (top) and intracellular recording (bottom), F. schematic diagram of NW-FET device and cell interface for extracellular recording (left) and intracellular recording (right). The purple outline marks the cell membrane and the lipid bilayer coating of the FET device, G. zoomed-in recording of the red-dashed boxes in extracellular recording (left) and intracellular recording (right). Adapted with permission from reference 21. 2010 The American Association for the Advancement of Science.

2.3.2 Bio-molecular Signal and FET

SiNWs have been designed to detect a variety of biomolecules, including DNA,[22] viruses,[23] proteins,[19,24] and biologically relevant ions.[25] Key to any sensor is its selectivity—a measure of how well the sensor can discriminate the desired analytes versus other interfering species.[26] Analytes serve as the gate in SiNW FETs by modulating the SiNW surface charge and thus conductivity, the output signal. This means that analyte selectivity can easily be designed into SiNW FETs by taking advantage of the plethora of known biomolecular interactions. Examples of these includes antibodies, nucleic acids and aptamers, all of which can have extremely low dissociation constant (K_D) values, engendering highly specific sensing without needing to design new sensory mechanisms, given the inherent self-signaling mechanism of FETs.

This strategy involves surface modifying the SiNW with a receptor specific for the desired analyte to detect. In this case, when the analyte meets the complementary receptor bound to the SiNW, the surface charge of the SiNW would be altered, transducing this biochemical interaction into an electrical output signal, in real time and in a label-free fashion. Additionally, given that SiNW FETs can be fabricated in an individually addressable manner, multiplexed biosensing is possible.[24]

Silicon and silicon dioxide surfaces have been the subject of much study over the past century. Alkoxysilanes and chlorosilanes, in particular, are commonly used reagents that condense on silica to form Si-O-Si bonds, imparting whatever functional group is present on the original silane. Many different functionalized silanes are commercially available, allowing for facile introduction of functional groups like amines, carboxylic acids, aldehydes, and thiols, enabling easy conjugation with biomolecules to serve as the receptor in the SiNW FET. Figure 2-6 details a common scheme used by Patolsky *et al*.[27] for surface-modifying SiNW-FET devices with an antibody to introduce specificity to the complementary analyte. First, the prepared FET devices are subjected to an oxygen plasma to remove any organic contaminants on the silicon dioxide surface, and to expose free silanols. Next, a functional alkoxysilane, in this case 3-(trimethoxysilyl)propyl aldehyde is used to introduce an aldehyde functional group on the SiNW surface. This enables antibody attachment to the SiNW via a reductive amination mechanism, wherein an imine is initially formed from the surface aldehyde with a native amine on the antibody, followed by reduction with sodium cyanoborohydride to afford a stable amine linkage. Unreacted silanes were similarly blocked using ethanolamine via reductive amination.[28] Similar approaches to introduce specificity elements have been accomplished using carbodiimide chemistry.[29]

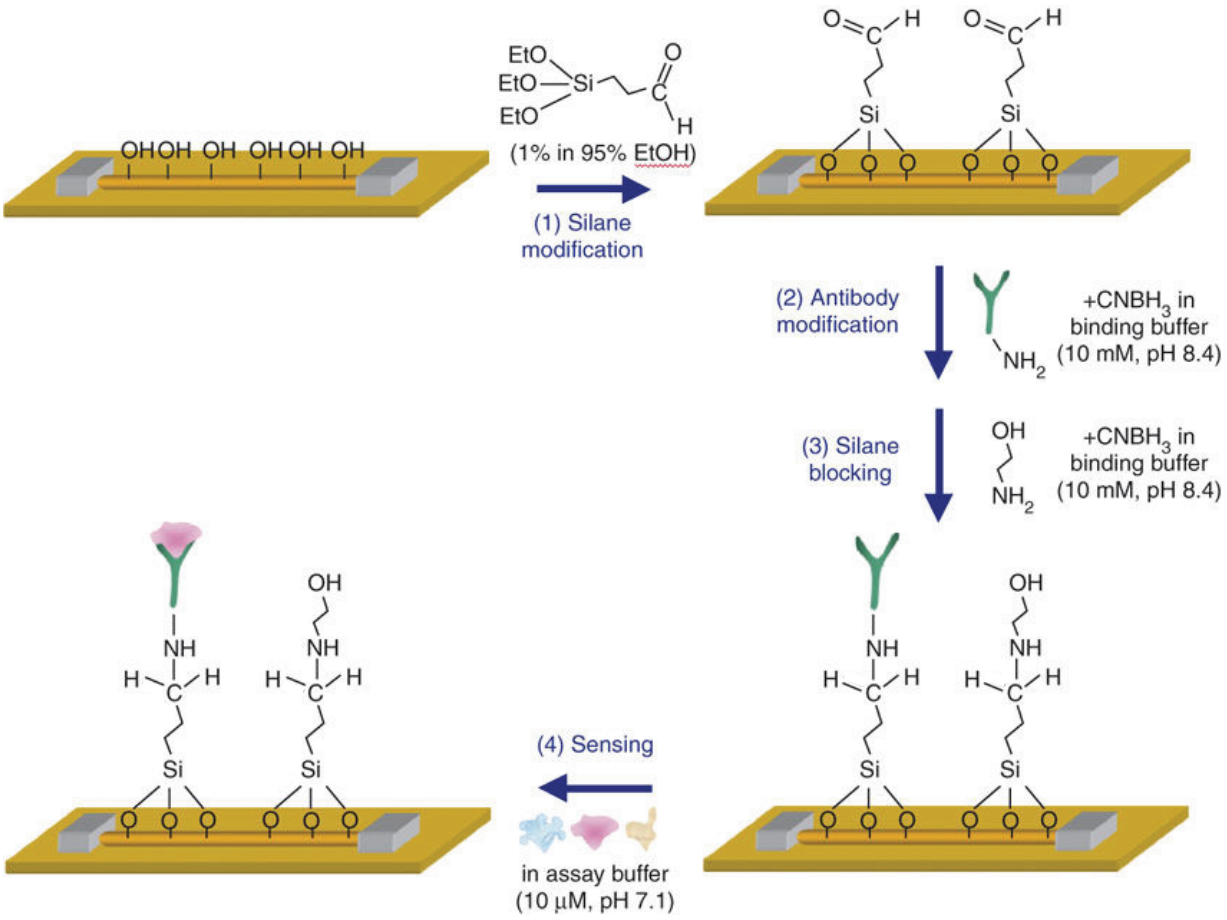

Figure 2-6. Surface functionalization of SiNW FET with an antibody to make a BioFET. SiNW are first treated with oxygen plasma to form surface silanol groups. (1) SiNW are immersed in a solution of a functionalized silane. (2) An antibody with a functional group complementary to the functional silane is added. (3) Silanes that did not react with the antibody are blocked. (4) The antibody binds its complementary analyte during operation of the BioFET as a sensor. Adapted with permission from reference 28.2007 Nature Publishing Group.

2.3.2.1 Learning point 2: Debye screening and detection limit

When placed in an electrolyte, the charged surface of a nanowire will attract counter ions, forming a double ion layer. This phenomenon, known as Debye screening, limits the detection range of the NW since charged species that are farther than the Debye screening length from the NW will not gate the NW-FET.

The double ion layer electrical potential (ψ) exponentially decays as a function of distance from the surface (y) over the Debye length (λ_D) (Equation 2-4).

$$\psi(y) \sim e^{(-y/\lambda_D)} \qquad \textbf{(Equation 2-4)}$$

The Debye length measures how well charges, often ions, in solution screen electric fields resultant from other charged species. It is a function of the dielectric constant (ε_r), the permittivity of free space (ε_0), the Boltzmann constant (k_B), and temperature in Kelvin (T) (Equation 2-5). N_A is Avogadro's number, q is the elementary charge, and C is the ionic concentration of the electrolyte.

$$\lambda_D = \sqrt{\frac{\varepsilon_r \varepsilon_0 k_B T}{2 N_A q^2 C}} \qquad \textbf{(Equation 2-5)}$$

The electric potential will decrease by 1/e for every Debye length. Thus, electrolyte solutions with higher ionic concentration have shorter Debye lengths. As a point of reference, in physiological environments (e.g. 1X PBS), the Debye length is 0.7 nm.

This short Debye length present in physiological environments presents challenges to FET-based biosensors since charged biomolecules that are 0.7 nm or further away from the device will be effectively screened and not be able to modulate the device conductance. One obvious way to overcome this challenge is to decrease the salt content of the solution. This can be accomplished by using microfluidic chambers to purify samples or by using the dialysis method to desalinate the sample. Altering the ionic strength of the solution can however affect the behavior of bimolecular species. Therefore other methods are being explored. For example, alternating current signals were used in drain-source voltage to extend Debye length by breaking down the electric-double-layer around the FET channel surface.[30] In 2017, Chu *et al*. used antibody and aptamer to immobilize electrodes of AlGaN/GaN high electron mobility transistor to overcome the Debye screening and to detect proteins in 1X PBS.[31]

The Debye screening can, on the other hand, screen out the bulk of the species in solution that are outside of the Debye sphere and increase the signal-to-noise ratio in some cases. For instance, in the case of monitoring binding and unbinding of bimolecular species to the NW, charge screening of other charged species farther away from the NW will decrease the background noise.

2.3.3 Mechanical Signal and Free-standing Nanowire

While the roles of biochemical and electrical cues in biological cells have been studied in many aspects in depth, those of mechanical cues have only begun to be understood. Mechanical cues, however, are ubiquitous in cells and play significant roles, such as in regulating apoptosis, proliferation, differentiation, wound healing and even antigen formation in B cells.[32–34] There are studies on force-sensitive proteins but there have not been many probes that can directly measure the forces exerted on cells by the environment.[35]

Zimmerman *et al*. used kinked SiNW to probe intercellular and intracellular force dynamics (Figure 2-7).[36] When the kinked SiNW is internalized in a cell, contraction or deformation of the cell bends the NW. The bending of the NW is quantified by modeling the kinked SiNW as a simply supported beam using Euler-Bernoulli beam theory. The SiNW and cell can be imaged concurrently using an optical microscope in a scatter-enhanced phase-contrast mode. An internal lamp was used in bright-field mode with a phase-contrast filter to image the cells while a ring LED (attached to the microscope condenser to emulate the light source in a backscattered mode) was used to image the SiNW. Silicon materials efficiently scatter light, meaning they be easily visualized in both bright- and dark-field modes.

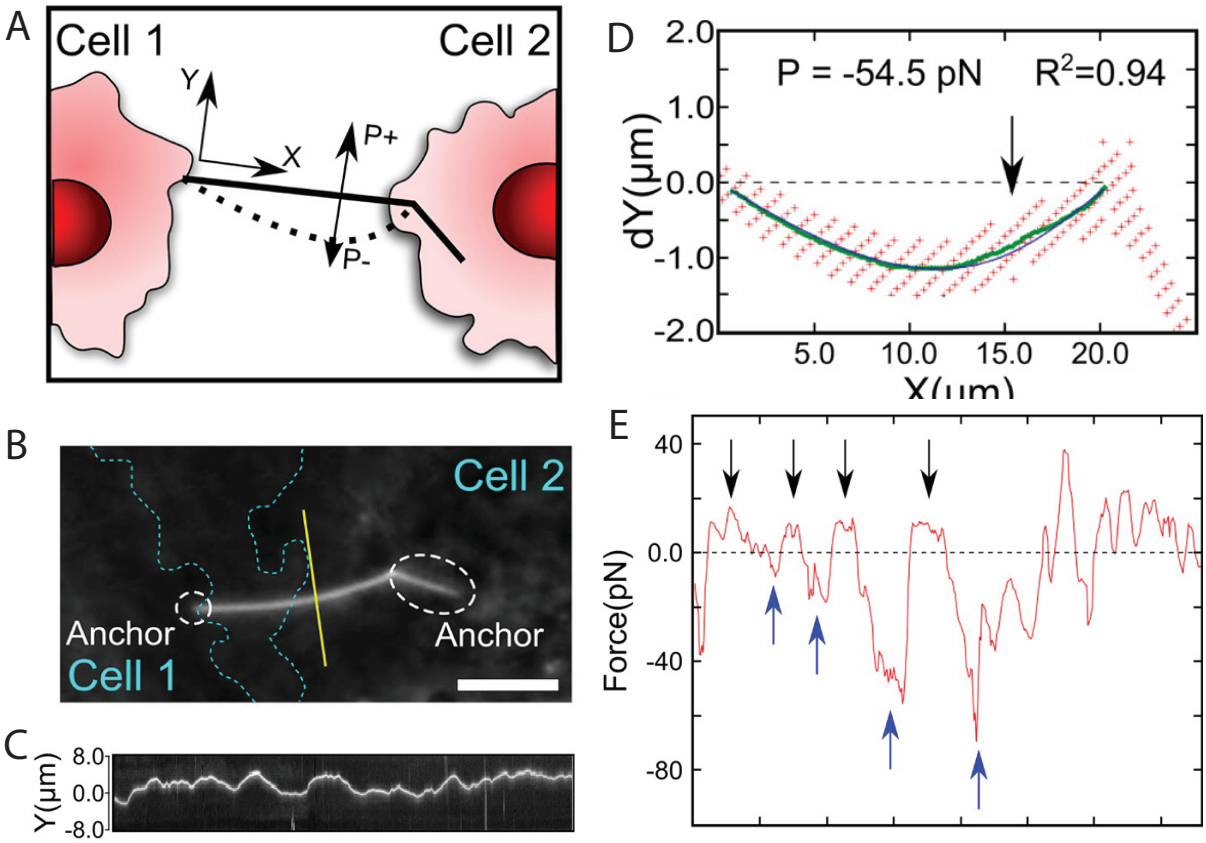

Figure 2-7. Kinked SiNW as a freestanding force probe. A. Schematics of human umbilical vein cells (HUVECs) and kinked SiNW, B. optical micrograph image of the HUVECs and a bent kinked SiNW. The cyan dashed line indicates the outline of two cell membranes, (scale bar 5 μm) C. A kymograph of the NW positions from the yellow line in (B), D. An example force fitting data of bent kinked SiNW. Red dots indicate the detected region of the NW and the green curve indicates the fitted centerline of the detected region. The arrow indicates the calculated load position, E. Calculated graph of bending force over time. The black and blue arrows indicate ratcheting peaks in the force plot. Adapted with permission from reference 36. 2015 American Chemical Society.

This particular study focused on investigating individual cells that had not necessarily reach confluency. With kinked SiNWs as a tool, further studies on systems that mimic biological environments, for example where cells are under constant shear forces, such as by blood flow, will be interesting.

2.3.4 Multiplexing and Tissue-level Devices

Lieber and coworkers extended the concept of recording from cells cultured on planar devices by integrating stimulation with recording. In a seminal paper, they fabricated arrays of SiNW-FETs and patterned regions of polylysine to promote desired cell growth orientations. To stimulate the cells, they used conventional glass microelectrodes to inject current. With their device, they were able to record intracellular potentials using extracellularly-placed FETs and observed action potentials.[27]

In later work, Lieber and coworkers developed tissue-scaffold-mimicking 3D arrays of FETs with stimulating electrodes.[37,38] The material was designed to be mimetic—in terms of the dimensions and mechanical properties to synthetic materials used as cardiac tissue engineering scaffolds, such as electrospun, biodegradable poly(lactic-co-glycolic acid) (PLGA) fibers. They initially fabricated a 2D free-standing mesh, and folded this material on top of itself to form a 3D structure. The material can have up to 64 individually addressable SiNW-FETs and four stimulation electrodes constructed from platinum/palladium.[38] To this 3D folded material, they seeded neonatal rat ventricular cells and cultured them inside the scaffold. This platform was then utilized to map and manipulated electrophysiology of 3D tissue in real time. The nanoelectronic scaffold enabled the mapping of conduction pathways in developing cardiac tissue with sub-milisecond resolution, in 3D. Further, using the four electrodes, they demonstrated stimulation of the culture.[38]

2.3.5 Future Directions

The biggest challenges for nanoscale FET-based devices are in increasing their signal-to-noise ratios and overcoming the Debye screening phenomena. Additionally, there is a need for nanoscale techniques that can accurately measure mechanical stresses at the intracellular and subcellular levels.

2.4 Modulation Probes [*]

The ability to synthesize nanomaterials in a controlled, precise manner has dramatically expanded the device possibilities for solar energy conversion. These advancements have driven decades of intense research, yielding both new basic science insights and immediately applicable breakthroughs. Researchers have exploited the unique features of nanomaterials, such as their high surface-to-volume ratio, ability to support surface plasmons, and synthetic tunability, in their application of cellular modulations. The applications in this area can be broadly grouped into three categories: solar-to-electricity, solar-to-thermal, and solar-to-chemical. Understanding photon conversion in these processes at the nanoscale in other fields has provided researchers with new approaches to target diverse research problems, among which is modulation of cellular behaviors. In this section, I will highlight how the general principles from energy science can be applied for biointerface studies, and in particular, how nanomaterials serve as light transducers in biological modulation.

Light energy conversion is the central role of modulation probes. Broadly, light energy science concerns, first, the absorption and conversion of the light energy and second, the extraction and storage of this new converted form of energy (i.e. electricity, heat, or fuel). While many lessons can be gleaned from nature's way of storing energy (e.g. photosynthesis), a key to optimizing light-matter interaction – light absorption and conversion – resides in artificially synthesized nanostructures. Here, I will explain why employing nanomaterials is crucial for successful light-matter interaction given the following advantages of nanomaterials. I will first

---

[*] A portion of this text has been adapted from Lee, Y.V. and Tian, B. *Nano Lett.* **19**, 2189-2197 (2019), with permission from the American Chemical Society.

describe how nanowires have been used in light to electricity conversion and then how they have been applied for light to chemical conversion applications.

Employing nanowire structures, in contrast with bulk materials, can increase the efficiency of photoinduced charge carrier collection because the carriers have shorter distances to travel (Figure 2-8 A). First generation solar cells required high quality crystalline silicon wafers as the minority carrier that would otherwise be trapped by defects before reaching the surface for successful charge extraction.[39] Such high purities are not required for SiNW or microwire arrays, as the photon absorption length and the charge collection distance can be decoupled; the minority charge carriers can travel radially to reach the surface while photons can be absorbed along the long axis of the nanowires or microwires.[40] While bulk measurements on many NWs or microwires can provide important insights that relate the material geometry (*e.g.*, spacing, diameter, length, *etc.*) to its photovoltaic efficiency,[41–43] optical and electric characterization down to single nanostructures can elucidate the fundamental limits and potentials of using nanostructures in solar-driven applications.[44] For example, Lieber and coworkers used the metal-catalyzed vapor-liquid-solid method to synthesize p-i-n coaxial SiNWs, and studied their photovoltaic characteristics and potential applications as the power source for nanoelectronics.[13] Similar to the carrier separation and collection in microwire arrays, the holes can travel to the p-type core, and the electrons, to the n-type shell. The nanowire length, intrinsic-shell thickness, and shell crystallinity can be controlled to vary the open-circuit voltage, short-circuit current and energy conversion efficiency of the single nanostructures.[13,45]

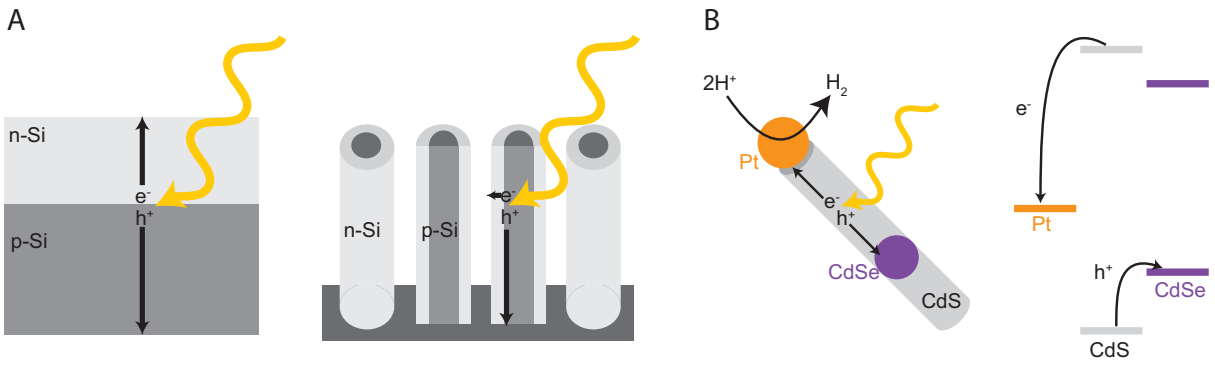

Figure 2-8. Using nanostructures can enhance the efficiency of solar-energy conversion processes. A. Schematic diagram of a Si-based photovoltaic device. Charger carriers are generated at the p-n junction and travel across the entire n-type (electron) or p-type (hole) thickness to reach the surface, achieving charge separation (left). In a nanowire photovoltaic device (right), electrons travel a shorter distance radially to reach the n-type surface, while the entire length of the nanowire can still absorb incident light. B. Schematic diagram (left) of a multicomponent nanodevice designed for photocatalysis. The CdS nanorod generates charge carriers upon light absorption. The CdSe seed localizes holes that are scavenged by solution species and the Pt catalyst uses the photogenerated electrons to drive the hydrogen production reaction. Energy level diagram (right) of different components showing the movement of the photogenerated charges in this system. Adapted with permission from reference 46. Copyright 2010 American Chemical Society.

Next, compared to the photon-to-electricity conversion, photon-to-chemical conversion (i.e. photocatalysis) requires additional charge transfer steps to drive redox reactions at the semiconductor-electrolyte interface.[47] These steps require a fine-tuning of the materials' surface properties as well as an increase in the lifetime of the charge-separated state. Nanomaterials provide unique advantages since their increased surface-to-volume ratio, as compared to planar devices, 1) provides more surfaces for the reactions to take place, and 2) reduces activation overpotentials that arise from the kinetic inefficiencies associated with low surface area materials.[48] In addition, the size, composition, and morphological control in the syntheses of colloidal nanocrystals or other nanostructures have opened additional avenues for photoelectrochemical processes. For example, Alivisatos and coworkers have designed a

multicomponent heterostructure– Pt-tipped CdS nanorod with an CdSe seed for photocatalytic hydrogen production.[46, 49] The photoexcited electron migrates from CdS to the Pt tip to be used in the H^+ reduction, while the hole moves to the CdSe seed (Figure 2-8 B). Spectroscopic studies on the electron[50] and hole[51] transfer dynamics in nanomaterial photosynthetic systems have yielded important insights on how to improve efficiencies.[52,53] Studies on catalysts coverage and photoabsorber architecture, have also identified the optimal photocathode design to minimize the trade-off between optical absorption and catalytic activity of opaque catalyst.[54]

Furthermore, several techniques have been developed for fabricating multifunctional or integrated devices. For example, Yang *et al.* synthesized a high-performing water-splitting photocatalytic device by coating the silicon photoanode with $Co_3O_4/Co(OH)_2$ biphasic thin-films *via* plasmon-enhanced atomic layer deposition.[55] In these multifunctional thin-films, the Co_3O_4 nanocrystalline spinel protects the Si substrate and provide durable catalyst/substrate interface while $Co(OH)_2$ promotes catalytic activities. As another example of integrated devices, Segev *et al.* combined photoelectrochemical and photovoltaic cells, such that the surplus photogenerated charge carriers (not consumed in fuel production) are collected to produce electrical power.[56]

We can easily imagine the utility of photoinitiated nanomaterial-assisted production of chemicals such as to produce reactive oxygen species.[57] While challenging, the ability to photocatalyze specific biochemical reactions has the potential to revolutionize nanomedicine by enabling the control needed for clinical translations.[58] To this end, I will discuss how nanostructured light absorbers and advanced fabrication techniques can be used to form close contacts with living systems (section 2.4.1) and modulate cellular behaviors via different types of photo-conversion (section 2.4.2).

2.4.1 Bio-Nano Interfacing for Cell Modulation

2.4.1.1 Cell Membrane-Material Interaction

Bianxiao Cui's and Yi Cui's groups have examined the cell-nanopillar interface in detail, showing that nanopillar arrays can pin embryonic cortical neurons from rats. They have shown an intimate interaction between nanopillars and neurons, causing the pillars to deflect and the pinned cells to have vastly reduced migration. Their studies have shown asymmetric membrane responses toward nanostructures, in that cell membranes easily deform inward to wrap around nanoscale objects and rarely deform outward.[59,60] Similar work was carried out by Yang and coworkers, culturing human hepatic stellate (LX-2) and a liver hepatocellular carcinoma cell line (Hep G2) on arrays of vertically-aligned SiNWs, demonstrating that cell spreading was restricted, compared to cells grown on silicon wafers. They showed that cells cultured on SiNW arrays interface with the substrate through filopodia and qualitatively demonstrated through centrifugation that cells more strongly adhered to NW arrays than to flat silicon wafers. Using Western immunoblotting, they also showed that collagen I and α-actin were down-regulated in cells cultured on SiNW arrays, relative to flat wafers, potentially consistent with the reduced spreading on SiNW arrays. Integrin and focal adhesion kinase were seen to be upregulated on SiNW arrays, compared to flat wafers, consistent with the stronger adhesion of the cells to the SiNW arrays, relative to flat wafers.[61]

It is perhaps instructive to consider interactions of cells with highly anisotropic topographical features as a form of mechanical stimulation. Bianxiao Cui's group and others have looked at the effect of such topography on intracellular signaling. Cells naturally contain mechanisms to sense and alter membrane curvature. These mechanisms are relevant for cellular processes involving vesicle formation and fusion, like endocytosis and exocystosis. As Cui's group describes what they call the curvature hypothesis, the same proteins involved in

endogenous curvature-recognizing mechanisms are activated by artificial sources of curvature; namely, inward deformations of the cell membrane around anisotropic materials. Further, mechanical stimulation of the nucleus by anisotropic structures can also affect gene expression.[62]

Besides nanoscale features, ones at the mesoscale can also affect biointerfaces. The anisotropic structure of the skeleton-like SiNW[12] (Figure 2-1 B) makes the retraction of the SiNW from collagen hydrogels harder compared to the initial insertion of the SiNW. Such anisotropic interaction is similar to the case of a bee-stinger that falls off the bee once inserted into a matrix. Due to its anisotropic structure, the SiNW has the potential to form a tight and semi-irreversible interface with soft biological samples such as biological tissues.

2.4.1.2 Wired-probe Design

Si has long been used as the working material in traditional electrodes for recording and stimulating electrically excitable tissue, such as neuronal tissue. The most common of these are planar microelectrode arrays, such as the Michigan and Utah arrays, which are still frequently used in the neural interface community and have been used in highly advanced brain-computer interfaces in humans. Multielectrode arrays, however, are on the order of microns to millimeters in thickness and millimeters in length, meaning that there is a limit to their spatial precision—that is, the volume of tissue stimulated or recorded from is rather large, leading to spatial under-sampling, and making single-cell resolution challenging with traditional electrode arrays.[63] Their bulky size and their need to be wired to computers for signal processing also mean that they are highly invasive. In addition to the short-term immune response resulting from their surgical implantation, the mechanical mismatch of silicon electrodes and the host brain tissue means that there is chronic inflammation due to micro-motions of the brain. This leads to glial scarring at the implantation site, attenuating signals over time.[64]

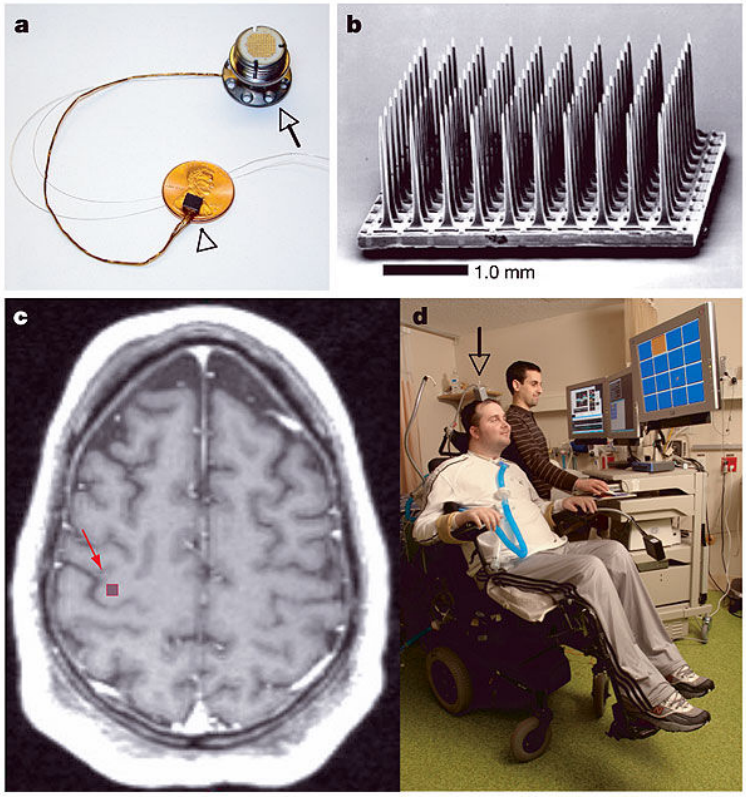

Figure 2-9. The BrainGate sensor. The BrainGate sensor, depicted by the arrow head, is shown in relation to a US penny. a. It is connected to a titanium pedestal, depicted by the arrow, affixed to the patients' skull. b. A scanning electron micrograph of the sensor portion of the BrainGate, showing the 10 × 10 array of 100 microneedle electrodes, each 1 mm long with a pitch of 400 μm. c. Preoperative magnetic resonance imaging scan (T1-weighted), showing the implantation site in the precentral gyrus of Participant 1's brain. Participant 1 in the BrainGate trial (MN). The arrow shows the location of the connection of the sensor, through the titanium pedestal, to the amplifier and signal conditioning hardware d. Reprinted with permission from reference 65. 2018 American Chemical Society.

Figure 2-9 shows the BrainGate sensor, a multielectrode array of 100 electrodes used to enable the user to control an external system by recording their thoughts, decoding them, and transducing this into an action. Figure 2-9 panels a and b shows the active sensor portion in comparison to a US penny, showing its relatively large size. Figure 2-9 d shows the external wiring required to attach the sensor to the computers for signal processing and decoding.[65]

As the fundamental unit of the brain is increasingly understood to be neural circuits, the ideal tools to probe these structures should be on similar length scales.[66] To assess the activity and function of neural circuits, then, probes should be able to sense and stimulate with spatial resolution on the order of the individual components of neural circuits: neurons. The requirement of single-cell resolution naturally suggests the nano- or meso-length scales, given that cells are on the order of microns. Advances in nanoscale fabrication of semiconductors, developed for the electronics industry, have enabled the creation of arrays of nano- and meso-scale probes for biological systems, and these arrays are uniquely suited to probing large circuits of cells with single-cell resolution.

2.4.2 Freestanding Probes

Freestanding probes not attached to substrates are attractive as they are more versatile tools than their substrate-bound counterparts. Free particles could conceivably be delivered in a drug-like fashion in ways that surfaces cannot, meaning that these free-standing probes could have therapeutic merit, whereas surface-bound devices are likely better suited as tools for fundamental cellular and tissue studies

Here we survey different approaches in which nanomaterials are used to elicit electrical or mechanical changes in single cells or cellular assemblies *via* photoelectrochemical or photothermal processes. Various recent works will be introduced to elucidate how nanomaterials can be used to optically modulate cells and tissues for potential treatment of neural degenerative diseases or cardiac conduction disorders. Excitable cells, such as neurons and muscle cells, fire action potentials for intercellular communication. Studies have shown that different cues, whether chemical, electrical, thermal[67], or mechanical[68], can instigate the firing of action potentials. Optical stimulations of excitable cells typically involve photoelectrochemical[69] or

photothermal[14] processes. These processes can either redistribute ions near the nano-bio interfaces or alter the biophysical properties of membranes.

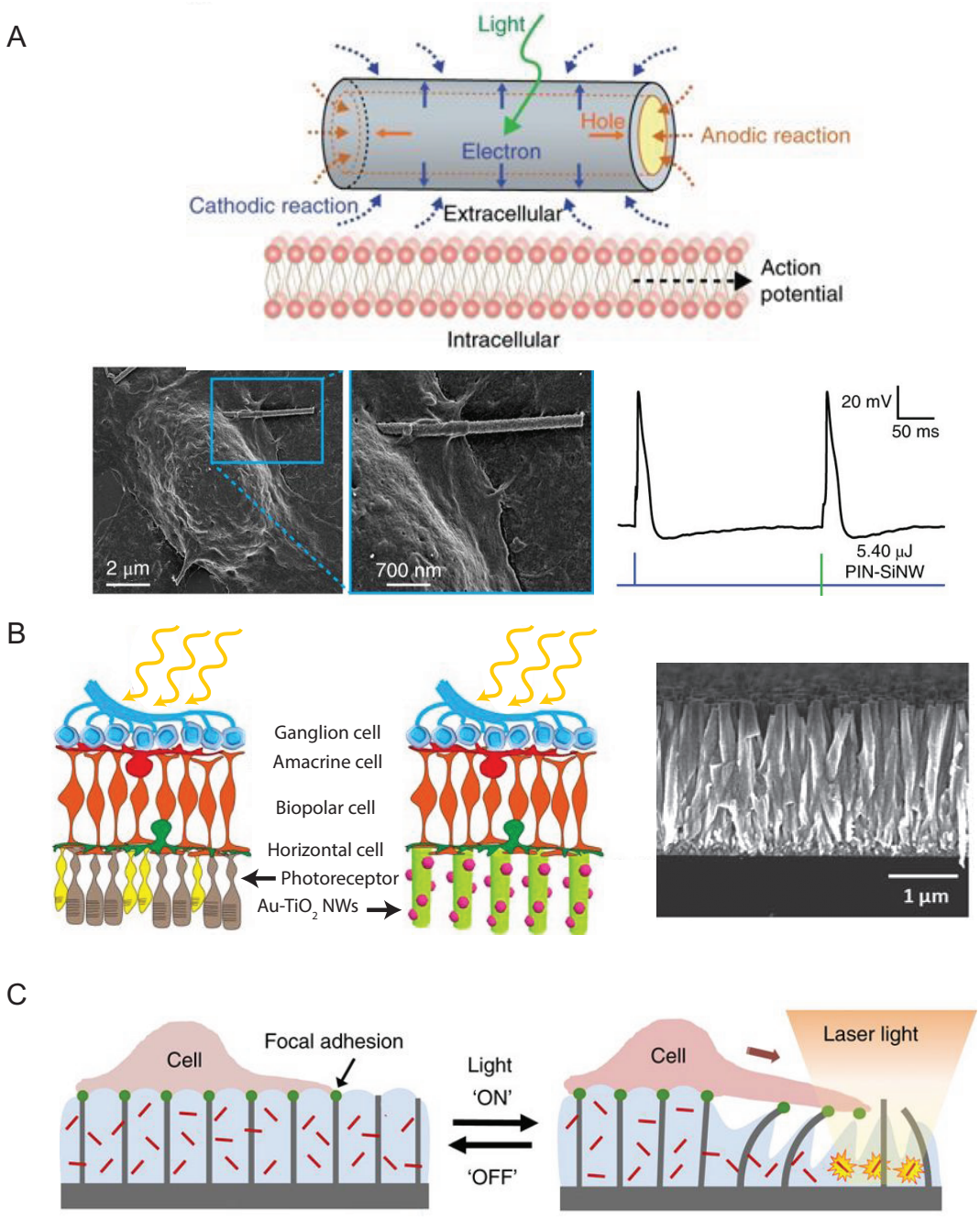

Figure 2-10. Nanomaterials can be interfaced with eukaryotic cells to modulate the cells' electrical or mechanical behaviors. A. Schematic diagram (top) of a p-i-n SiNW sitting near a cell membrane. Photogenerated electrons diffuse to the n-type shell and induce membrane polarization via the cathodic electrochemical effect (blue dotted line). This process is proposed to

(**Figure 2-10 continued)** induce action potentials. Photogenerated holes travel along the p-type core (anodic reaction represented by the orange dotted line). SEM image (bottom left) of a single p-i-n SiNW sitting on a DRG neuron and a zoomed-in image showing the interface. A trace (bottom right) of a DRG neuron membrane potential recorded by a current-clamp path-clamp technique. The neuron is stimulated first, by a current injection (blue pulse) and then, by a laser pulse (green bar). Reprinted with permission from ref 45. Copyright 2018 The Authors. B. Architectural similarity observed in biological and artificial photoabsorbers. Schematic diagram of a retina (left), and a Au-TiO_2 NW array interfaced retina (middle). Adapted with permission from ref 32. Copyright 2018 Springer Nature. SEM image (right) of InGaN NW array used in photovoltaic devices. Reprinted with permission from ref 71. Copyright 2012 American Chemical Society. C. Schematic diagram of a cell sitting on a microstructure composite containing a photoresponsive hydrogel and Au nanorods (represented as red rods). Upon a light trigger, the hydrogel contracts, bending the microstructure and stretching the portion of a cell adhered to the microstructure tips. Reprinted with permission from reference 57. 2017 Springer Nature.

2.4.2.1 Photoelectrochemical Stimulation

Optically modulating cellular behaviors with semiconductors can directly incorporate material designs from solar energy conversion research. Parameswaran *et al*. recently reported a freestanding photoelectrochemical modulation platform using SiNWs. Drawing inspiration from the solar cell literature, they synthesized core-shell SiNWs fabricated into nanoscale diodes with a p-type core, intrinsic shell, and a n-type outer shell. They interface the p-i-n SiNWs with primary dorsal root ganglion neurons and demonstrated that action potentials could be produced in a manner indistinguishable from those elicited by traditional patch clamp methods.[70] The presence of diffused atomic Au on the NW surface was an integral part of photoelectrochemical current generation, as the Au species can catalyze the photocathodic current that locally depolarized neurons (Figure 2-10 A). In detail, the mechanism was reported to be light-induced production of electrons and holes in the material, with the built-in electric field of the diode enhancing charge separation. Photoexcited electrons move to the n-type shell and participate in a cathodic process at the semiconductor-electrolyte interface. The authors also examined the role

of atomic gold on the NW surface. Between the core and shell growths, they intentionally diffused the gold catalyst down the sidewalls of the nanowire at low pressure, resulting in atomic gold-induced surface states. Despite most considerations of gold as a source of deep traps in silicon, the authors showed that the atomic gold was necessary to elicit action potentials. The effect of the gold was attributed to alteration of silicon surface states, such that the impedance of the NWs in aqueous solutions was reduced, which would enhance the faradaic currents that depolarized the cells. The measured photoelectrochemical currents were unipolar in nature. This interesting phenomenon was suggested to be due to the larger exposed area of the n-type shell, relative to the p-type core exposed at the ends of the nanowires. The photoanodic reaction would be expected to occur at the p-type core-electrolyte interface due to the built-in electric field of the diode accelerating holes to this region. The authors also hypothesized that the non-equilibrium current production was in part due to the surface states altered by the atomic gold.

By controlling the laser power, duration, and frequency, trains of action potential can be generated, obeying up to the intrinsic limit of the neurons. As the material could be dropcast on cells without any pre-treatment, this freestanding semiconductor nanomaterial-based optical modulation offers the prospect for target-specific cellular control at the single-cell level.

In contrast to freestanding single nanowires, multiple nano- or microscale semiconductor components can be assembled/fabricated into macroscopic devices for larger scale tissue or organ-level stimulation. Parameswaran and Koehler *et al.* have used a fibronectin-coated SU-8/p-i-n SiNW mesh to optically stimulate and train rat heart *ex vivo* to beat at the frequency of applied optical pulse.[71] In an earlier pioneering example, Palanker and coworkers implanted silicon photodiode microarrays into the subretinal region of a rat's eye to restore the vision of rat, where the devices replace the damaged photoreceptors.[72]. In practical applications, a video

camera can capture the original images, followed by image processing in a mini-computer, signal transduction into a goggle, and projection of NIR pulses onto an eye. In a related study, Tang *et al.* interfaced a gold nanoparticle (AuNP) decorated titania nanowire (TiO_2 NW) array with the retina to restore vision in blind mice.[73] Because pure TiO_2 NW absorbs primarily in the UV region, having AuNPs is necessary to enhance the photo-absorption efficiency in the visible region (the absorption of ~10 nm AuNPs peaks around 550 nm). Along with the excellent biocompatibility and stability of this nanomaterial, the orientation of highly anisotropic NWs that resemble the architecture of a photoreceptor is advantageous as it imparts efficient light absorption and charge transportation. The similarity in architecture among the photoreceptors, the AuNP-TiO_2 array, and the aforementioned Si nanowire array suggests how the geometries of nanostructures can be leveraged for light-triggered biological processes.

2.4.2.2 Photothermal-bioelectric Stimulation

The photothermal effect refers to the process by which light energy is absorbed and converted to heat, typically within metals or small bandgap semiconductors that display more efficient electron-phonon coupling. [74,75] Recent areas of research utilize the plasmonic effect: the phenomenon in which mobile charges within metals or heavily doped semiconductors oscillate resonantly with incoming photons.[76] In addition to enhancing the light absorptivity in photovoltaic and photocatalytic devices,[77] the plasmonic effect seen in nanoparticles can enable localized photothermal processes as the oscillating electrons de-excite and couple their energy to vibrations in the local chemical environment. Spectroscopic studies have been performed to better understand the heat transfer dynamics from the plasmonic particles to their surrounding environment,[78] as well as the local heating mechanism through light scattering.[79]

Analogous to using photoelectrochemical effect to restore vision, researchers explored the photothermal process to restore hearing. Stoddart and coworkers used plasmonic heating of Au nanorods to modulate auditory neurons.[80] Traditional infrared neural stimulation results in a limited photothermal effect as water is the primary source of heating.[81] By adding the Au nanorods, biologically transparent near infrared lasers (with a 780 nm wavelength) can be utilized and deeper tissues can be reached. Recent studies have suggested two mechanisms for photothermal neuromodulation: 1) production of capacitive current across cell membranes,[82] and 2) activation of thermosensitive ion channels.[83] Benzanilla and coworkers used the photothermal effect of AuNPs to elicit action potentials in DRG neurons through the change of membrane electrical capacitance.[84] It was experimentally revealed that the rapid change in local temperature induces a capacitive current due to the change in membrane capacitance,[82,85], which depolarizes the cells and elicits action potentials. Additionally, the ligation of AuNPs' surface with antibody-conjugates provides ways to target specific cell phenotypes.[84] Besides using plasmonic heating, Jiang *et al.* have used the photothermal effect of amorphous Si mesostructures to trigger action potentials of DRG neurons,[14] where the multi-scale structural heterogeneities softened the materials and enhanced the light adsorption.

2.4.2.3 Photothermal-biochemical Stimulation

Hybridizing the plasmonic nanomaterials with temperature sensitive polymers can open up a plethora of new applications by leveraging the polymers' mechanical responses.[86] Poly(N-isopropylacrylamide) (PNIPAm) is particularly suitable because of its high thermal responsiveness with a sharp phase transition.[87] Sutton *et al.* incorporated Au nanorods into a PNIPAm hydrogel to mechanically modulate cell morphology through light triggering (Figure

3G).[88] The hydrogel containing the plasmonic particles sit on a microstructure, to which cells were attached. Irradiating the structure with a NIR laser causes the hydrogel to contract due to the heating from Au nanorods. Subsequently, the contraction bent the microstructures and deformed the cells, elongating the cells to 140% of their unperturbed length. Given the facts that 1) cells attach to various microstructures,[89] and 2) plasmonic nanostructures have shape- and size-dependent resonance absorption peaks[88], this photothermal mechanomodulation platform can potentially produce a large variety of cellular responses with light.

Introducing nanomaterials into cells that can convert light energy into heat can also mechanically perturb the intracellular environment. Jiang *et al.* introduced a novel intracellular mechanical manipulation tool by optically stimulating a SiNW internalized in an endothelial cell.[14] Upon illuminating the SiNW, the microtubule that entangled the NW was immediately repelled, forming a void near the NW. The authors suggested that this void was formed by a photoacoustic mechanism. In this process, a shock-wave was generated as a result of local heating, which drove the mechanical depolymerization of the microtubule network around the SiNW. In addition to this cytoskeletal response, it was also hypothesized that the local photothermal effect from SiNWs could transiently perforate organelles, such as the endoplasmic reticulum and mitochondria, thus triggering intracellular calcium ion release.

Jiang *et al.* also demonstrated photothermal stimulation using nanoporous silicon particles (Figure 2-1 C) to depolarize dorsal root ganglia neurons. They used a nanocasting approach, wherein an ordered, nanoporous silica material was used to template the decomposition of silane into amorphous silicon, followed by etching of the silica template, affording an all-silicon material. The material was drop-cast on cell membranes and was shown to depolarize neurons by heating the cell and changing the membrane capacitance.[14] The photothermal mechanism of the

nanoporous silicon particles, as well as bulk silicon, is due to the indirect bandgap of silicon, wherein optical excitations thermally decay, radiating heat.[90] Further, given the nanoporous nature of the particles, they have degradation kinetics on the order of days, meaning they could be used for transient biological modulation.[14]

At the extracellular level, mechanical stimulation is only recently being appreciated as an important biological process, despite having been known about for several decades (Figure 2-11). We predict that intracellular and extracellular mechanical stimulation of cells will therefore become important cellular modulation tools. We envision free-standing probes to be able to mechanically modulate cells, both in extracellular and intracellular fashions, which will be an important next-step in the direction of biological modulation for various clinical applications.

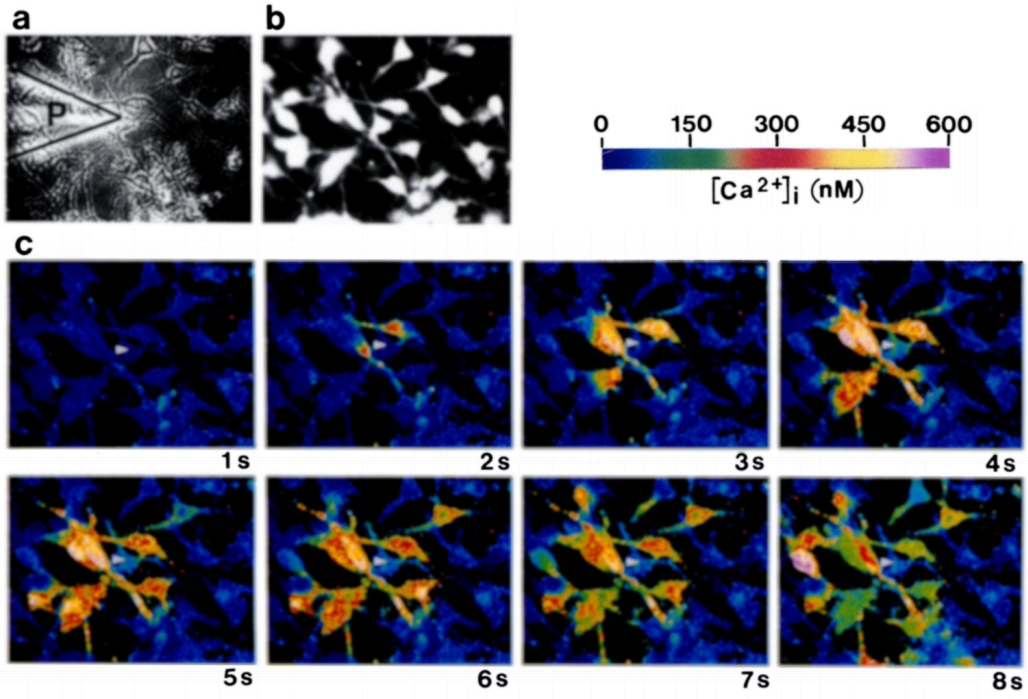

Figure 2-11. Mechanical stimulation response of glial culture. a. Phase-contrast micrograph of 7-day-old mixed glial culture. Single-cell mechanical stimulation is achieved with a micropipette (P). b. Ca^{2+} imaging of the same field of cells in (a) using Fura-2. c. Sequential time

(**Figure 2-11 continue** **d)** points of the same field of cells in after mechanical stimulation of one cell, showing Ca2+ wave propagation to other cells, in all directions. All images are scaled to 155 μm vertically by 210 μm horizontally. Reprinted with permission from reference 91. 1991 Elsevier.

The examples shown in the previous sections highlight some recent advances in using nanomaterials for non-genetic cellular sensing and modulation. Specifically, the highlighted photoelectrochemical or photothermal methods do not induce permanent changes to the cell, as in genetic manipulation. Additionally, some of the interfacing materials such as Si can degrade over time under physiological conditions[92], and subsequently get cleared out from the biological system. Further discussion on establishing a strong biointerface for cellular modulation[9] and the advantage of using a non-genetic method[93] can be found in other reviews.

3 Synthetic Insights in Multi-nucleated Nanowires

3.1 Introduction

Before jumping into this chapter, I would like to reiterate the basics of silicon (Si) nanowire growth mechanisms (section 2.2), which applies to the growth of many other semiconducting nanowire materials. First, the nanowire is grown via the vapor-liquid-solid (VLS) mechanism (Figure 2-1). Above the eutectic temperature of gold (Au) and silicon (Si), silane (SiH_4) gas decomposes to a Si atom and two hydrogen (H_2) molecules or multiple single hydrogen (H) atoms on the Au catalyst surface. The Si atom in the vapor phase is dissolved into Au liquid catalysts, forming a Au-Si alloy. Once the concentration of Si reaches the saturation point, the Si precipitates out, forming a solid Si nanowire. As this process continues, aided by the continuous flow of SiH_4, the nanowire grows longitudinally moving away from the growth substrate. Once the desired length is reached, the nanowire core can grow radially via the vapor-solid (VS) mechanism. In the VS mechanism, the Si gas atoms directly deposit onto the Si nanowire sidewall, skipping the liquid phase of dissolving into the Au-Si alloy. As a result, the nanowire does not elongate but instead grows radially, increasing the width of the nanowire. The rate of VLS growth versus the VS growth and vice versa can be controlled by adjusting the temperature, pressure, and flow rate of the precursor gas, SiH_4, as described in the Materials & Methods section.

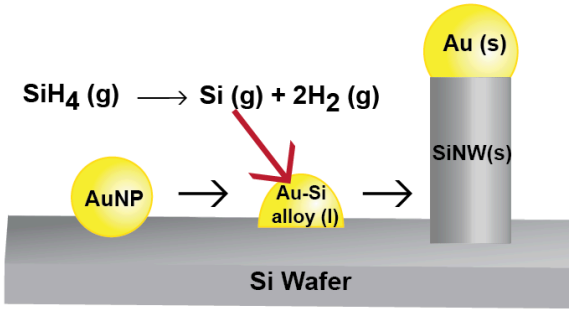

Figure 3-1. Schematic explaining the VLS mechanism of a SiNW growth. Si (g) dissolve in to Au-Si alloy (l) and eventually precipitate out to for SiNW (s).

Various synthetic studies focus on diameter modulation along the longitudinal axis of the nanowire. The diameter of silicon nanowires can be controlled through preferential etching post-synthesis. For example, Luo *et al.* patterned Au along the Si nanowire sidewall by modulating the pressure during the nanowire's longitudinal growth. In the post-synthesis etching process, the diffused Au-pattern acted as an etchant-resist, and left a skeleton-like Si morphology.[12] In another study, phosphorous dopant concentration was modulated during nanowire growth to encode the morphology that appears after dopant-dependent wet chemical etching along the nanowire long axis.[11] Different from post-growth etching, another study demonstrated diameter modulation of Ge nanowires by controlling the surface passivation of the sidewall during VLS-growth, thus inducing VS sidewall growth in the absence of surface passivation.[94]

In this chapter, I present a unique strategy in which I introduce multiple spheroids near the kink of kinked-Si nanowires. Our multi-nucleated nanowire involves two key synthesis steps: Au island formation and Si restructuring. As shown in Figure 3-2**,** our new nanowire synthesis deviates from the simple kinked-nanowire synthesis as Au islands separate out from the main Au-Si alloy catalyst during the prolonged purge step of more than 30 seconds. Once the growth is resumed, hair-like nanowires grow from these small Au islands along with the nanowire arm

from the main Au catalyst. During radial growth, the hair-like nanowires undergo considerable restructuring, forming spheroids by the kink. In the following sections, I will explain the interplay of growth conditions and Si and Au dynamics in the synthesis of these morphologically unique nanowires.

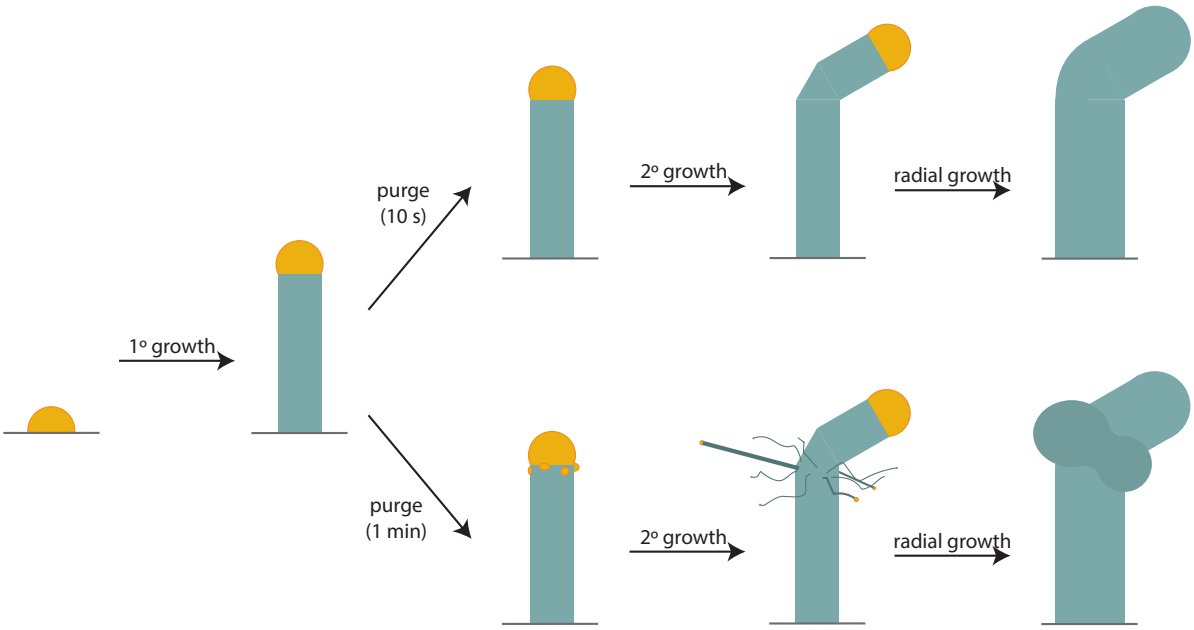

Figure 3-2. Schematics of the multi-nucleated nanowire growth. First, Au (yellow) nanoparticle catalysts are deposited on a Si wafer (grey). During the primary growth, the Si nanowire (teal) main body is grown. Depending on the purge duration, the resulting structures differ from each other. For a short purge (top), the nanowire arm grows in a different direction from the nanowire main body during the secondary growth, forming a kink. For a longer purge (bottom), Au islands/droplets separate out from the main Au catalyst. Once growth is resumed (secondary growth), along with the nanowire arm, the hair-like nanowires grow from the Au islands/droplets as their nucleation sites. During the radial growth, the hair-like nanowires restructure to form spheroids (darker teal) around the kink while the nanowire becomes thicker overall.

In this chapter, I use the following terms to refer to different parts of the nanowire:

- **Primary (or main) nanowire**: the nanowire grown from the main catalyst.
- **Main body**: The portion of the primary nanowire grown during the primary growth

- **Arm**: The portion of the primary nanowire grown during the secondary growth
- **Hair-like nanowire** (branches): the thin branches that are grown during the secondary growth from the isolated Au catalysts
- **Spheroids**: the hair-like nanowire branches that went through any duration of radial growth. Note that they appear more similar to the branches at the beginning of radial growth.

3.2 Results and Discussions

3.2.1 Au nucleation: separation from the main Au catalyst

To grow hair-like Si nanowire branches around the nanowire main body, we need the small Au catalysts for the branches to grow from. Previous studies have achieved synthesis of branched-Si nanowire structure in various ways. Gaboriau *et al.* spray-coated Si nanowires with aerosol Au nanoparticles, from which Si nano-branches grew, resulting in a tree-like nanostructure.[95] Jun and Jacobson used a focused ion beam to etch part of the Si nanowire sidewall and deposited Au on the etched area, from which the Si branches grew.[96] This process can also be accomplished without a separate *ex-situ* Au seeding step, as illustrated in a study performed by Doerk *et al*'s inter-growth annealing method. In this study, Si nanowire branches were grown by inducing Au-Si migration from the main catalyst to the nanowire sidewall then resuming the VLS growth (Figure 3-3).[97] Silicon branches grew from the Au surface along the primary Si nanowire's [111] direction.

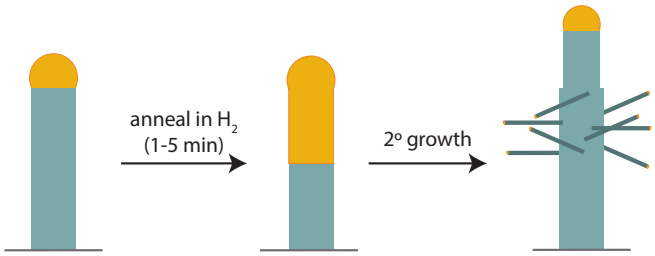

Figure 3-3. Schematics of branching Si nanowire synthesis via inter-growth annealing. After primary growth of the primary nanowire, the nanowire was annealed in H_2 for 1 - 5 min at 850 °C. Upon reintroduction of SiH_4, growth resumes and Si nanowire branches grow from the Au droplets.[97]

Similar to the inter-growth annealing method of Doerk *et al*'s, we also induce Au migration from the main Au catalyst to the nanowire sidewall to grow the hair-like branches. As illustrated in Figure 3-2 and Figure 3-3, the products are different in two ways: the presence or absence of a kink in the primary nanowire and the extent of Au migration. While almost all nanowires form a kink in our 1-minute purge step, no nanowires had a kink from the inter-growth annealing method. The absence of a kink in the inter-growth annealed sample can be attributed to the large size Au nanoparticles used as catalysts. A previous study has shown that smaller diameter Si nanowires have a higher tendency to form a kink than their larger counterparts because the relative Si concentration in the drop is larger for the smaller Au catalyst droplet given the fixed purge time.[98] The abrupt and relatively large change in the Au-Si alloy composition can destabilize the growth from interface, resulting in a kink formation. Given the fact that we used 50 nm diameter Au nanoparticles, as opposed to the 500 nm diameter Au nanoparticles used in the inter-growth annealed sample (Doerk *et al*.), such different results were not surprising.

Next, the lack of H_2 during the purge can explain the locality of our hair-like nanowires. While the Si nanowire branches of the inter-growth annealed sample are in a range of few micrometers along the primary Si nanowire, our hair-like nanowires are situated within 200 nm

from the kink. Our method differs from that of Doerk *et al.*'s in that we purge all the gas from the reaction chamber – including H_2 – while H_2 is present during Doerk *et al*.'s inter-growth annealing step. Doerk *et al.* claims that the presence of H_2 is crucial to induce Au migration during the inter-growth annealing as H_2 prevents the oxidation of Si sidewall; oxidized Si sidewall may impede Au-Si migration.[99] In our purge step, H_2 is effectively removed as the reaction tube reaches the pressure of 200 mTorr. We postulate that the Au islands were tightly distributed near the kink, given the slow migration rate.

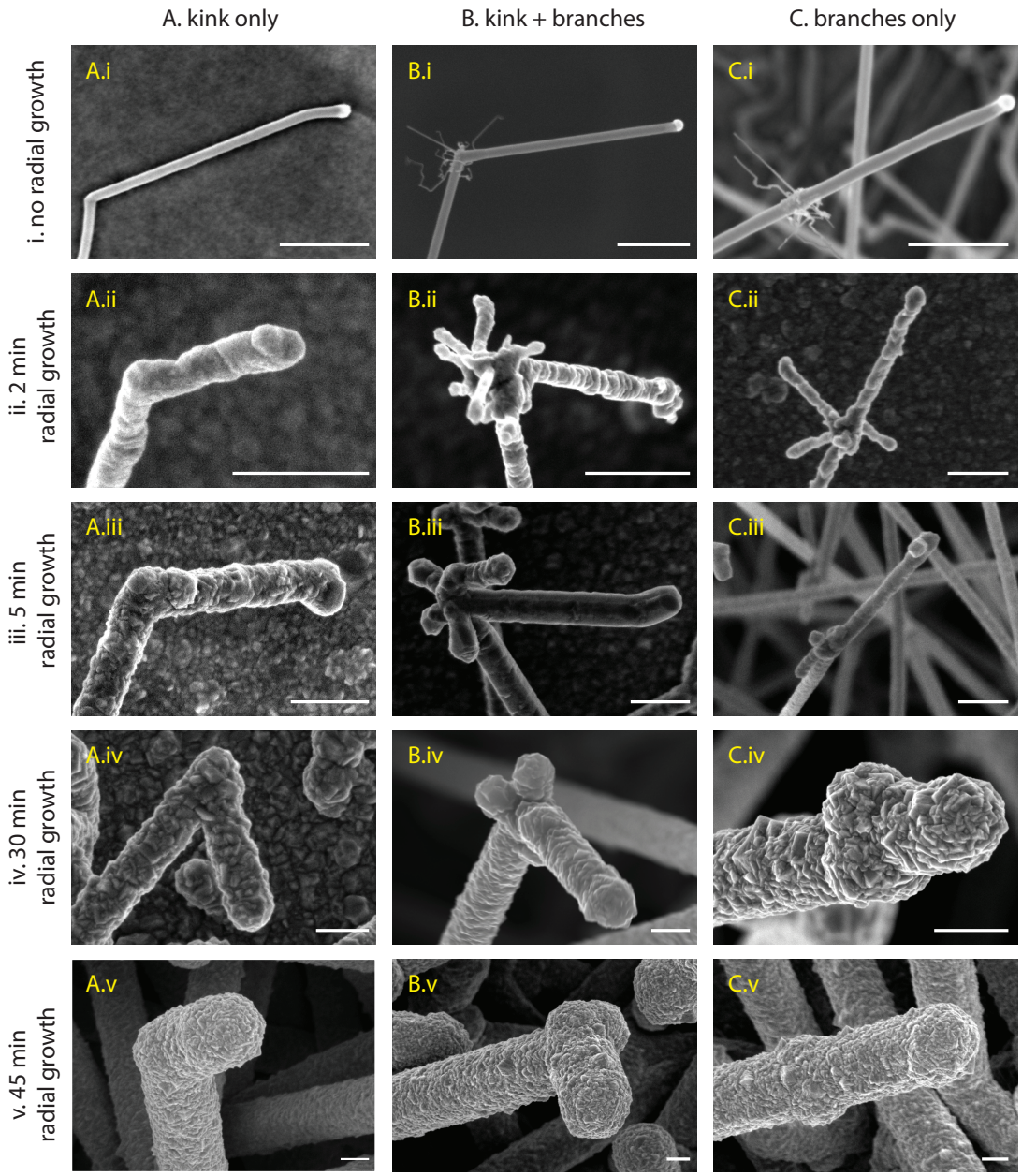

Figure 3-4. Representative SEM images of nanowires. Column A shows nanowires with only a kink, column B shows nanowires with a kink and branches, and column C shows nanowires with branches only. Row i shows nanowires without any radial growth. Rows ii, iii, iv, and v, show nanowires that underwent varying durations of radial growth of 2-, 5-, 30-, and 45-minutes, respectively. Note, that the nanowires in Figure 2 were all synthesized with 50 nm Au nanoparticles. All scale bars 500 nm

3.2.2 Secondary growth: arm and hair-like nanowire growth

Once the growth is resumed, hair-like nanowires and the arm grow from the Au islands and the main Au catalyst, respectively (Figure 3-4. row i). We observed on average 10 ± 4 hair-

like nanowires per primary nanowire (Figure 3-5 A). We expect to see more hair-like nanowires to nucleate from a primary nanowire with a larger diameter, assuming that the Au islands' size and density will not change with the primary nanowire's increased diameter and decreased curvature. On average, these hair-like nanowires were 15 ± 9 nm in diameter. We observed mostly thin (< 15 nm diameter) hair-like branches with one or zero thick (>20 nm diameter) hair-like branches for each primary nanowire. It is worth noting here that the diameter value of 15 nm, is likely to be an overestimated upper bound because the thin nanowire diameters are measured based on SEM images as opposed to TEM images; the thin nanowire appear thicker as it moves sideways when it gets bombarded with an electron beam in SEM. We did not see any obvious correlation between the thickness of the hair-like nanowires and the purge time. The length of each hair-like nanowire is dictated by the duration of the secondary growth time. It is worth noting that the length of these branches to eventually plateau to a certain range, as it is challenging to grow long nanowires from such a small Au catalyst; the Au catalyst will eventually deplete as it slowly diffuse down the Si sidewall during the VLS growth.[100]

The obvious benefit of this synthetic strategy is having the control over the structure's surface area-to-volume ratio. One can simply grow more bands of the hair-like nanowire branches to increase the overall surface area-to volume ratio as the ultra-thin nanowires have significantly larger surface area-to-volume ratio compared to the primary nanowire. The increased surface area-to-volume ratio can be beneficial when large surface area is needed for either loading other materials on the surface or making more points of contacts with a biological entity.

When nanostructures are used as vessels for drug delivery, heterogeneous catalysis, loading photo sensitizer, etc., having a large surface area-to-volume ratio is crucial. As described

in section 2.3.2, surface modification of Si is a well-established field and various Si-based materials, like nanoporous Si, have been used for the aforementioned purposes. In light of the nanopillars studies in which cell tightly wrapped around Si nanopillars (Chapter 2.4.1), the hair-like nanowire branches can help form tighter biointerface by having more number of adhesive points of contacts with a cell. For applications in bio-sensing and bio-modulation, it is crucial for the nanomaterial to form a strong biointerface with the bio system to have a high signal-to-noise sensing and to reliably pass along stimulus. In addition, the flexibility and softness of the ultra thin nanowires better matches the Young's modulus of the soft biological system than the thicker primary nanowires. This can help the nanomaterials more seamlessly integrate with the biological system by minimizing any immune response. Such thin Si nanowires, however, may not be suitable for long-term applications like implant devices because Si nanomaterials can degrade in physiological conditions. The insights gained from the thin nanowire synthesis are nonetheless applicable to other metal-catalyzed VLS grown 1-D nanomaterials and should be further studied.

3.2.3 Radial growth: restructuring of the hair-like nanowire

Longer vapor-solid (VS) deposition of Si on the nanowire sidewall results in radial growth of both the primary nanowire and the hair-like branches. More importantly, during radial growth, these hair-like nanowires undergo a conspicuous amount of restructuring. Specifically, we observe a drastic decrease in the number of the hair-like nanowires and a transformation of the long, hair-like nanowires into rounder spheroids (Figure 3-5.).

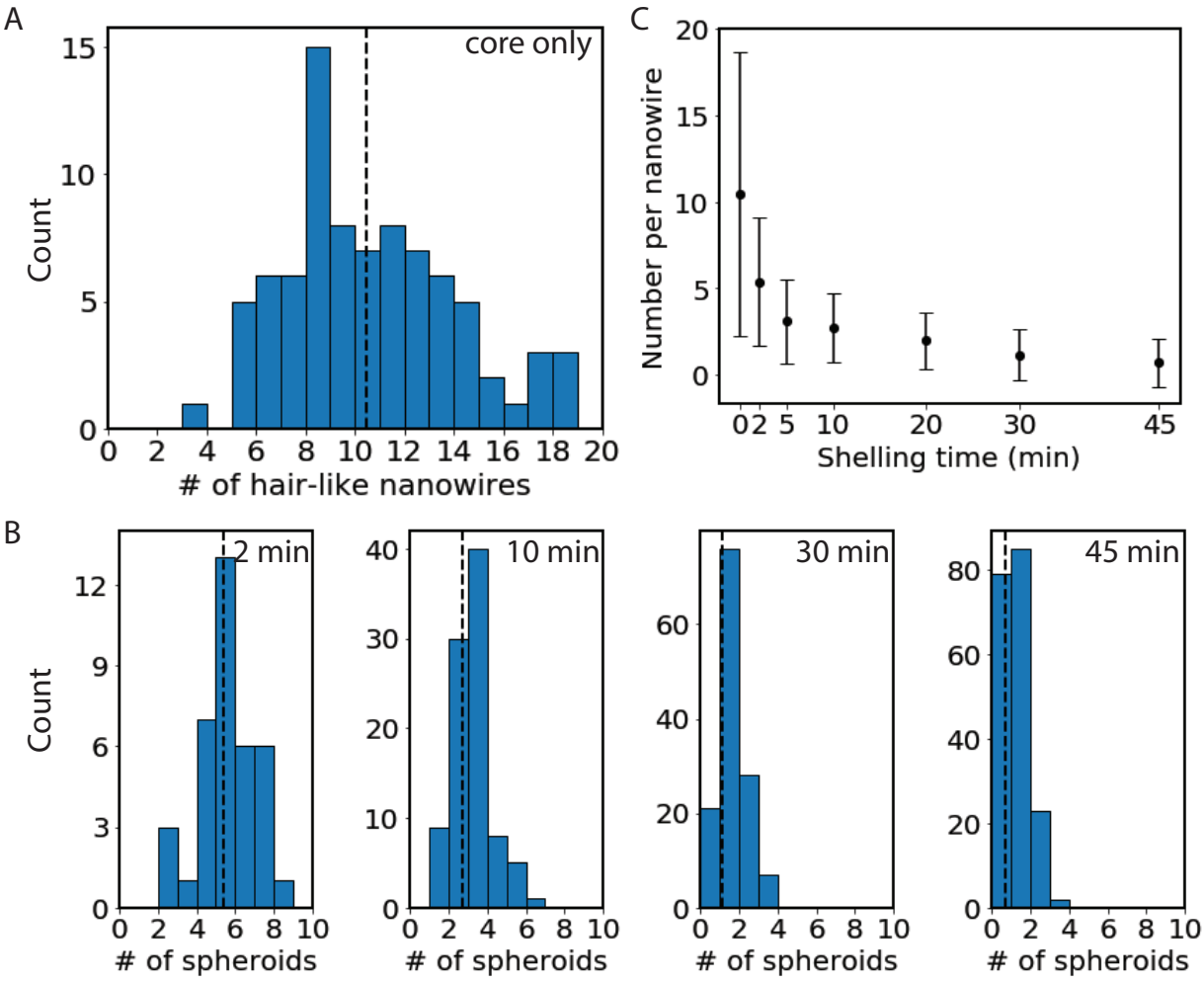

Figure 3-5. Effect of radial growth on the number of spheroids. A. Histogram of the number of hair-like nanowires. B. Histograms of the number of spheroids on the radially-grown nanowires, with 2min, 10 min, 30 min, and 45 min radial growth time (left to right). Vertical lines (dotted) indicate the average number of protrusions in each histogram. C. Plot of the average number of branches (hair-like nanowire and spheroids) over different radial growth times.

I have hypothesized three different mechanisms for the restructuring. First, neighboring hair-like nanowires could have coalesced to for the observed spheroids. As the branches grew thicker in diameter, their sidewalls could have come into contact and further VS Si deposition could have effectively enclosed the neighboring hair-like nanowires and made them into a single spheroid. Based on this theory, we would expect to observe a gradual coalescing from the base with tips of the branches sticking out, as individual parts. This is because the distance between

the hair-like branches is much further at the tip than at the base near the primary nanowire, as the branches grow on a curved surface. As experimental data does not show such signs (Figure 3-4. B. iii), I conclude that this explanation does not hold. The second hypothesis is that the shorter branches may have been enclosed by the radial growth of the primary nanowire. This explanation, however, was disproved by simple measurements. We compared the 2-minute radially grown multi-nucleated Si nanowires with their 5-minute radially grown counterparts, and between these two groups the number of spheroids decreased by more than 2 spheroids per nanowire on average (from 5.4 to 3.1). We found that the primary nanowire thickness increased by about 30 nm during the additional 3-minute radial growth. The shortest branch observed in the 2-minute sample was 38 nm in length (measured from its tip to the base, n = 100). These numbers clearly evidence that the radial growth of the primary nanowire is not thick enough to enclose even the shortest branch, disproving the second proposed hypothesis.

Finally, I concluded that an Ostwald ripening-like diffusion of Si atoms could explain the restructuring of the hair-like nanowires. Different from coalescence, Ostwald ripening diffusion involves dissolution of the Si atoms from the original structure via either a vapor-phase diffusion or sidewall diffusion to form larger and lower-curvature spheroids. This is not unexpected, as such diffusion is frequently observed during VLS growth of various semiconducting nanowires such as silicon nanowires,[101,102] magnesium oxide nanowires,[103] and germanium nanowires.[104] Ostwald ripening-like diffusion was also employed to form various nanostructures such as nanowhiskers,[105] rectangular nanoislands,[106] and nanospheres.[107] In this case, the Si diffusion could have happened either in vapor phase or via nanowire sidewall surface diffusion (Figure 3-6.).

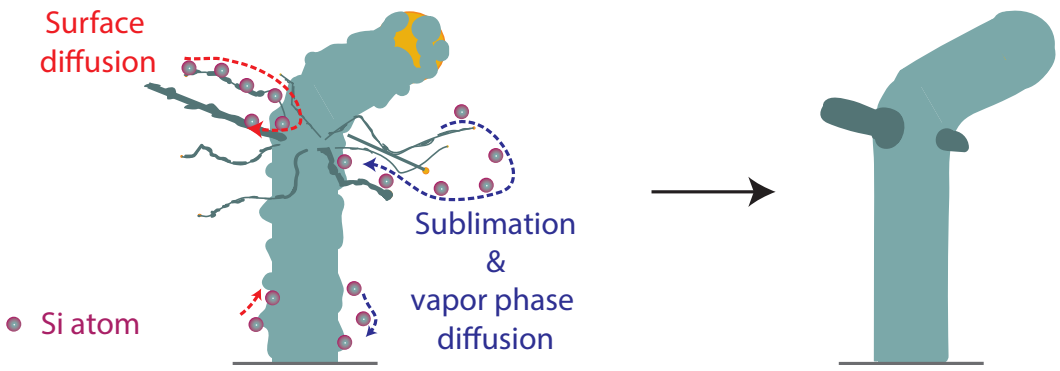

Figure 3-6.. Schematics illustrating the two diffusion routes of a restructuring. On the right, Si atoms diffuse along the surface of the spheroids and the primary nanowire and deposit in a thermodynamically stable site (red dotted line). Si atoms sublime (i.e. desorb) from the spheroids and the primary nanowire surfaces, diffuse in the vapor phase, and redeposit. The restructuring results in rounder spheroids and smoother primary Si nanowire sidewall (left).

To further confirm the Ostwald-ripening hypothesis, we conducted an annealing experiment in the absence of the Si precursor. Having the 2-minute radially grown sample as a control, we annealed another 2 minutes radially grown sample under H_2 at 850 °C for 60 minutes. Annealing produced three distinct changes that confirm the restructuring. After annealing, 1) the number of spheroids decreased, 2) each spheroid became rounder in shape, and 3) the primary nanowire surface became smoother (Figure 3-7). Because there was no influx of a new Si source, we can deduce that all of the above happened from the atoms in the thin hair-like nanowires and the high curvature bumps on the primary nanowire sidewall.

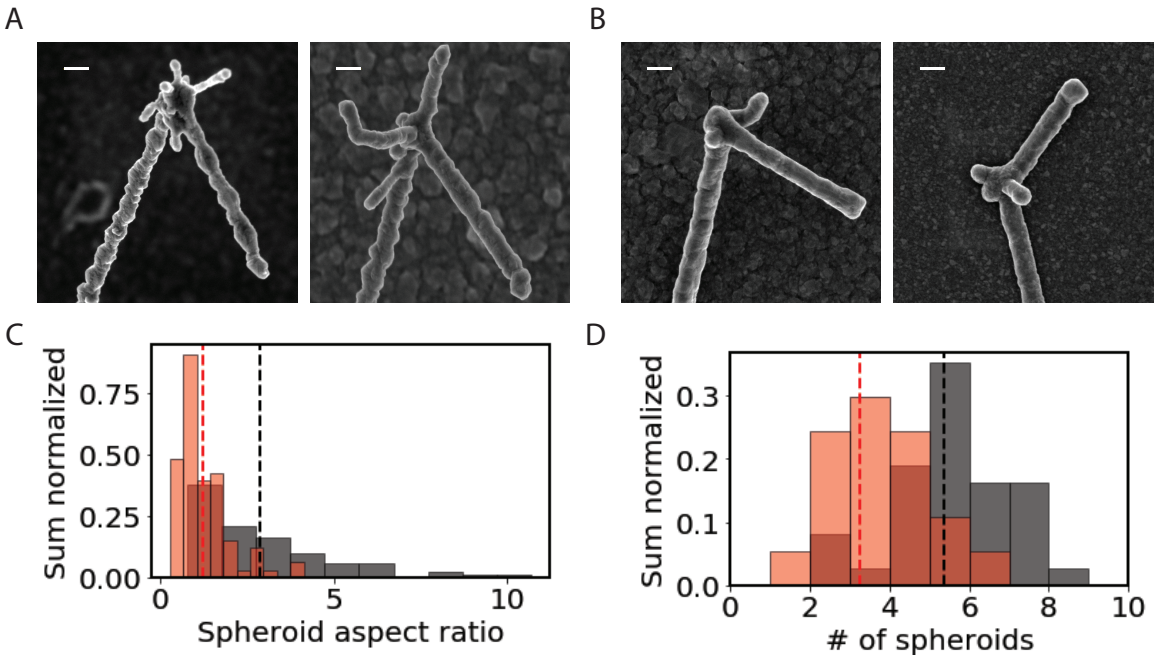

Figure 3-7. Effects of annealing after radial growth. SEM images of 2 min radially grown nanowires (A) and 2-min radially grown and 60-min annealed nanowires (B). Histogram of the spheroids' aspect ratio (spheroid length/ spheroid diameter), all scale bars 500nm (C) and a histogram of the number of spheroids per nanowire (D) of the 2-min radially grown (black) and 2-min radially grown and 60-min annealed (red) nanowires. The shifts in the histogram peaks towards the lower aspect ratio in C and towards the lesser number of protrusions in D show how annealing restructures the branches into spheroids.

3.3 Future Work & Conclusion

Given the fact that all synthetic steps are sequential and done *in situ*, most structural parameters can be controlled. The duration of the primary and secondary growth controls the length of the primary nanowire's main body and arm. The amount of restructuring, and thus the number of spheroids, can be controlled by both the duration of radial growth or an annealing time. Furthermore, the kink angle between the main body and the arm can be controlled either by modulating the growth kinetics[108] or by using etchants.[109] It will be of interest to test whether the spheroids' loci can be determined based on the kink angle. For example, for some kink angles, the space between the arm and the main body may be too limited, forcing the spheroids to face the direction opposite from the arm's orientation. In the opposite case, one can prevent the kink

formation altogether by using a large Au nanoparticle. With a shorter purge duration (i.e. 30 seconds) and radial growth, one can expect a straight Si nanowire with spheroids structure along the nanowire's long axis. In another variation, one can also combine our restructuring step with the inter-growth annealing method to have the spheroids populate a longer range of the primary Si nanowire.

Lastly, we would like to point out the possibility of introducing multiple regions with the hair-like nanowires along the primary nanowire long axis. The position of the hair-like nanowire nucleation can be determined by purging the system at different times during the nanowire's VLS growth. Based on the primary nanowire thickness and purge duration, the formation of kinks in the primary nanowire can also be controlled. This positioning of rings of nanobranches, with well-defined positions, along the length of the main nanowire body is unique to our nucleation strategy because we let the Au diffuse within a limited range and at a slow rate.

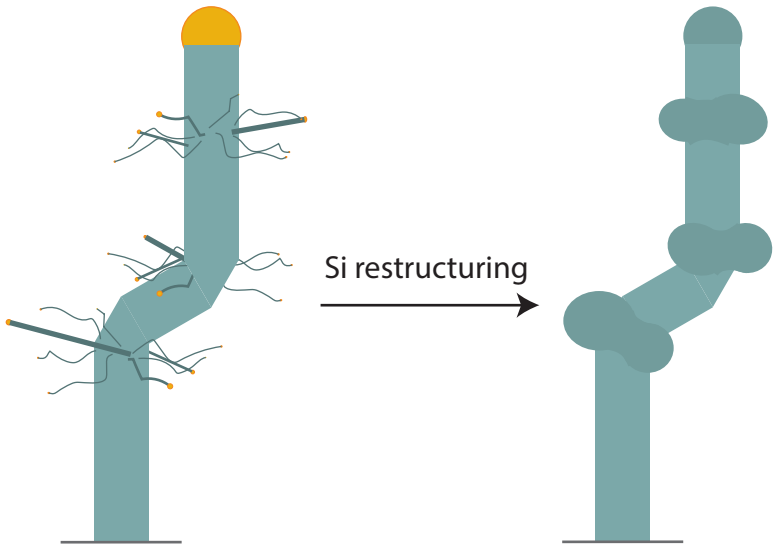

Figure 3-8. Schematic diagram of a nanowire with the rings of hair-like nanowire branches along its primary body and that after Si restructuring. Despite the different amount of secondary growth time, we expect the hair-like nanowire branches to display similar length, as the depletion of the small Au catalysts will limit the length of the thin nanowire.

In this work, we have systematically studied a way to first grow the hair-like nanowires and then reconstruct these thin nanowires into spheroids. We believe our insights into the Au diffusion during the purge step and the Si restructuring during the radial growth (i.e. VS deposition) can expand the range of Si and other semiconducting nanowire morphologies.

3.4 Materials & Methods

Nanowire synthesis. Multinucleated kinked Si nanowires were synthesized via the vapor-liquid-solid mechanism[110] with a home-built chemical vapor deposition (CVD) system. The CVD system consists of a temperature-controlled furnace, a quartz tube encased in the furnace, and a vacuum pump and gas manifold connected to the tube. Either in the beginning of the day or the night before the syntheses, the quartz tube was baked at 950 °C for at least two hours to keep the tube clean of contaminants. The quartz tubes were replaced after a few syntheses, especially when a long (>30 minutes) radial growth step was involved.

For each synthesis, either an n-type or a p-type <100> Si wafer (Nova Electronic Materials) was used as a growth substrate. The wafer was cleaned in buffered-hydrofluoric acid (BHF, 10 min) to remove the native oxide layer, washed with water, and dried with N_2 gas. 50 nm Au nanoparticles (Ted Pella, diluted with BHF in 1:1 v/v ratio) were deposited on the wafer (typically, 20 min), washed with water and dried with N_2 gas. The prepared wafer was placed in the center of the quartz tube.

The nanowires were synthesized in the following steps: primary growth (typically, 5 to 30 minutes) of the nanowire main body, purge (10 seconds for the kink-only samples, 1 minute for the kink and nuclei samples), and secondary growth (1 minute) of the nanowire arm. The nanowires were grown at 480 °C under 40 torr. Silane (SiH_4), phosphine (PH_3, 1,000 ppm in

H_2), and hydrogen (H_2) were used as the Si source, dopant source, and carrier gas, respectively. SiH_4, H_2, and PH_3 were flown in at the rate of 2, 2, and 60 standard cubic centimeters per minute, respectively. In between the primary and secondary growth, the quartz tube reactor was purged towards the based pressure of about 1 mTorr for 1 min to introduce a kink and the Au nuclei. In this step, some nanowires remain straight but still display the nuclei, as shown in Figure 2 row C. To introduce the kink without the Au nuclei, the system was purged for a shorter period of time. Finally, for radial growth of the longitudinally grown nanowires, the temperature was raised to 750 °C in a vacuum. Radial growth was done at 750 °C under 20 torr, with SiH_4, H_2, and PH_3 flowing at 0.3, 1.5, and 60 standard cubic centimeters per minute, respectively.

Structural characterization. All scanning electron microscope images of the nanowires were taken directly from the growth substrate with Carl Zeiss Merlin field-emission SEM. The nanowires' structural parameters (i.e. main body and nuclei thickness, nuclei base to tip length) were measured manually with the ImageJ program.

4 Image Analysis: Detection and Segmentation of Kinked Nanowires[†]

In this chapter, we introduce our newly developed particle detection algorithms that can precisely and efficiently detect and segment rod-like particles. We developed this algorithm specifically to be used in our rotational tracking method (Chapter 5) by detecting different parts of a kinked nanowire. For this application, it is crucial for the detection algorithm to reliably detect a kinked nanowire and its components, which are a main body and a short arm grown at the end of the main body. The end goal is to use this algorithm to measure the vertical distance from the arm end to the main body, which we refer to as the projected length of the nanowire arm (PL_{arm}).

We developed two key algorithms to measure the projected length of the nanowire arm (PL_{arm}): a *Gaussian centerline detection* algorithm to detect the nanowire center and a principal component analysis (PCA)-based algorithm to distinguish the arm from the nanowire main body (Figure 4-1). Prior to applying these algorithms, we used a simple threshold method to find a region containing the nanowire in each frame; nanowires are easily seen in dark field imaging, as they appear bright due to their high scattering efficiency. [111]

[†] A portion of this text has been adapted from Lee, Y.V. *et al. Nano Lett*. ASAP. DOI: 10.1021/acs.nanolett.0c00974, with permission from the American Chemical Society.

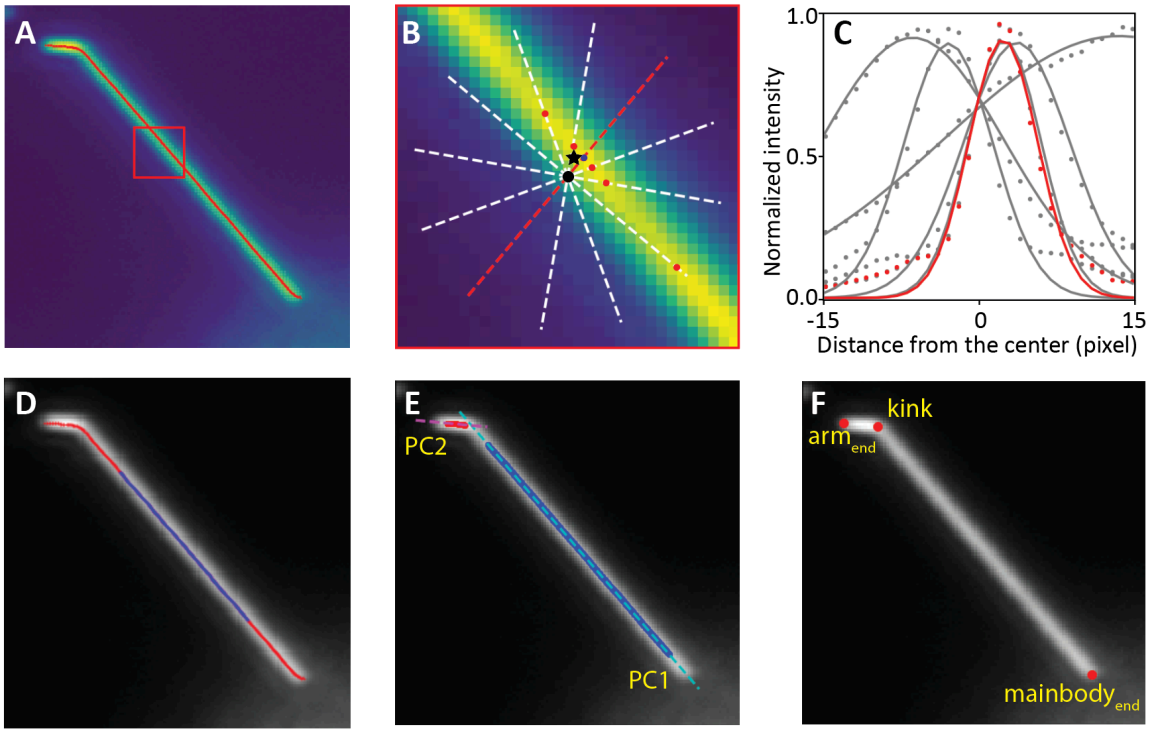

Figure 4-1. Particle detection algorithms. A-C Demonstration of the Gaussian Centerline detection algorithm: A. Optical microscope image of a kinked silicon nanowire (in color, based on the intensity) with the detected Gaussian centerline (red) overlay. Around each bright pixel, we selected a sub-image (red box) and applied the line filter algorithm. B. Zoomed-in image of area marked by the red box in A. The threshold-selected bright pixel (black dot) is fitted to a center (black star); 30-pixel long intensity profiles (dotted lines) centered on the coordinate of interest are fitted to their centers (red dot) every 30 degrees; and the selected intensity profile line (red) is roughly perpendicular to the nanowire main body. C. Normalized intensity profiles (dots) along the lines in B and their Gaussian-fitted lines (solid lines). The selected profile and fitted line are in red. D-F Demonstration of the PCA-based segmentation algorithm: D. Middle section of the Gaussian-selected center is selected (blue) for the initial fitting of the PC1. E. Fitted results: PC1 (dotted cyan line) fits the main body part based on the blue region. PC2 (dotted magenta line) fits the arm part based on the red region. F. The three coordinates (arm_{end}, kink, $main\ body_{end}$) are selected based on PC1 and PC2.

4.1 Gaussian centerline detection algorithm

To resolve the sub-diffraction center of the nanowire, we built a custom MATLAB and Python algorithm named *Gaussian centerline detection*. Inspired by single-molecule localization techniques,[112] we reasoned that a similar algorithm could be used to detect the center of a nanowire which is also a sub-diffraction-limited object in its longitudinal dimension. We also

adopted a line filter tool – inspired by retinal blood vessel detection – to detect the direction normal to the nanowire (Figure 4-1 top row).[113]

We implemented the algorithm in three steps: image restoration, finding the normal direction to the wire, and fitting for the sub-diffraction center of the nanowire in the longitudinal plane. In each step, every nanowire pixel selected in the previous step was re-centered to contribute to identification of the nanowire center. Around each pixel, we selected a sub-image of at least 7×7 pixels in and applied the line filter algorithm. We fitted the intensity profile of each line filter in the sub-image to a Gaussian. In most cases, the line fit with the narrowest Gaussian represented the best normal direction to the nanowire, whose Gaussian center was assigned as the true center of the pixel. This process was repeated for all pixels in the threshold-selected nanowire.

Application of the *Gaussian centerline detection* algorithm significantly improves the accuracy of the PCA-based arm detection in the next step. Due to their high scattering efficiency, silicon nanowires appear more than ten times thicker than their actual diameter under the optical microscope.[111] This apparent radius or thickness can result in an inaccurate measurement of PL_{arm} as shown in Figure 4-2.

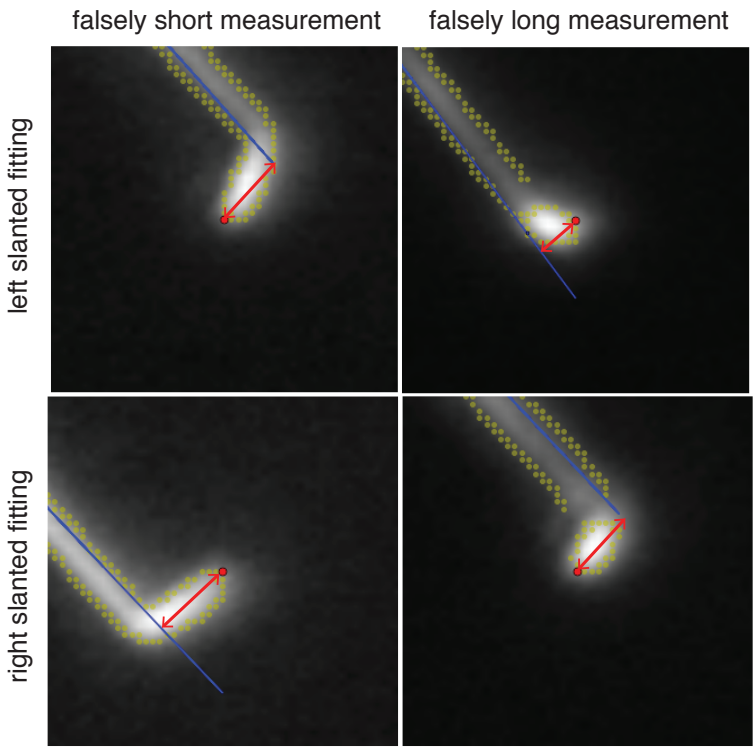

Figure 4-2. Inaccurate detection of PL_{arm} when not applying the *Gaussian centerline detection* algorithm. The yellow dots are the threshold-selected outline of the nanowire, the blue solid line is the fitted center of the nanowire main-body part, and the red doubled-sided arrow indicates the measured PL_{arm}.

The *Gaussian centerline detection* algorithm also addresses other problems presented by the non-zero apparent thickness of the nanowire, which are detrimental for the rotational tracking application in Chapter 5. First, when solving for the nanowire's longitudinal orientation (θ), the non-zero thickness of the nanowire image causes an ambiguity in PL_{arm} when the nanowire arm is lying nearly parallel to the substrate (defined as the longitudinal orientation near 0° and 180° in Chapter 5) (Figure 4-3). Second, when the nanowire arm is oriented perpendicular to the substrate (a near-90° longitudinal orientation as defined in Chapter 5), the arm aligns with the main body and becomes shadowed (Figure 4-3).

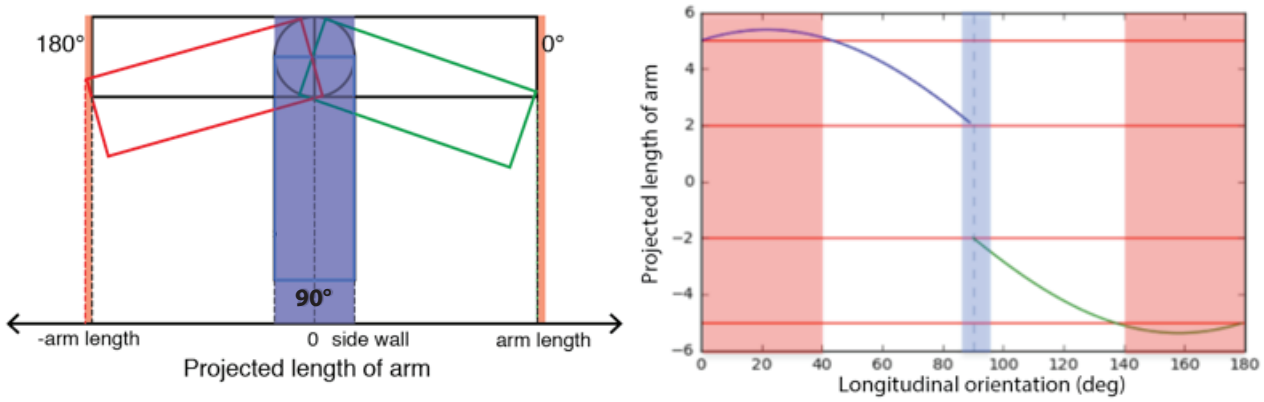

Figure 4-3. Ambiguous and shadowed ranges caused by the apparent thickness of the nanowire. Left: schematics of the nanowire arm in various orientations and their corresponding PL_{arm}. Right: plot of the PL_{arm}'s for every possible longitudinal orientation. Here, the apparent thickness of the nanowire (r) is 2 and the arm length is 4. Both: red regions are the ambiguous range, and blue regions are the shadowed range.

By narrowing the nanowire selection (i.e. making the apparent radius of the nanowire (***r***) almost negligible), the *Gaussian centerline detection* algorithm greatly reduces the ambiguous regions near 0° and 180° and the shadowed region near 90°. As a result, we utilized 80% of the non-interacting video and 98% of the cell-interacting video (Table **4-1**). Note that more frames were discarded for the non-interacting video as its nanowire rolled more vigorously and more frequently crossed the shadowed region.

Table 4-1. % utilization of the data

Experiment	Original # of frames	# of shadowed frames	# of ambiguous frames	Utilization rate for data processing (%)
Free-floating	1500	14	16	77
Cell-interacting	4500	80	5	98

4.2 Principal component analysis arm detection algorithm

We used a second custom Python algorithm, *PCA-arm detection*, to segment the nanowire into the main body and the arm by fitting the centerline coordinates to principal component 1 (PC1) and principal component 2 (PC2), respectively. In our application, the variables were x and y, and the observed data were the coordinates of the nanowire center.

We automated this PCA step and used the minimal number of hyper-parameters in order to minimize the introduction of artifacts and decrease processing time. First, we used a subgroup of coordinates near the centroid, which presumably does not contain the arm, to fit PC1. The subgroup was then reselected to encompass all the coordinates that fell within a certain distance of the previously fitted PC1. Based on the newly selected subgroup, PC1 was fitted again. These steps were iterated typically three times to ensure accuracy (Figure 4-1 D). Next, we used the remaining coordinates to fit PC2 in a similar fashion (Figure 4-1 E). Finally, we determined the PL_{arm}, by measuring the distance from the arm end point to PC1 (Figure 4-1 F).

In summary, we developed the *Gaussian centerline detection* algorithm and utilized principal component analysis to detect the longitudinal rotation of the nanowire efficiently and precisely. Furthermore, the versatility of these algorithms will allow them to be extended to the processing of other nanoscale objects with various geometries. Finally, while not shown in this thesis work, the tracking method presented in Chapter 5 can be extended to non-living systems, including the study of emergent phenomena of active matter [114,115] and nanoscale fluid dynamics, or applied as a general nanoscale probe of torque. To this end, we envision incorporating both convolutional and recurrent neural networks into our particle detection algorithm to enable multi-nanowire detection. The convolutional neural network is necessary for the identification of the nanowires from the background and the segmentation of each nanowire. The recurrent neural

network will be integral for indexing different particles that appear in a time-series data, i.e. video.

5 Tracking Longitudinal Rotation of Silicon Nanowires for Biointerfaces[‡]

The rolling motion (i.e. longitudinal rotation) of nanomaterials may serve as a proxy to probe local microscopic environments. Furthermore, nanoscale rotations in biological systems are common but difficult to measure. Here, we report the development of a widely applicable tool that measures rolling motion of nanowires modified with short arms. We show that the nanowires' rolling dynamics are significantly affected by their surroundings and showcase the probes' ability to reflect different cellular behaviors. A non-interacting nanowire undergoes rapid sub-diffusive rotation, while a cell-interacting nanowire exhibits slow sub-diffusive rotation when it is fully encompassed by the cell and super-diffusive unidirectional rotation when the cell actively interacts with the nanowire. Our method can be used to yield insights into nano-mechanics in various biophysical and assembly processes.

5.1 Introduction

Tracking the rotation of a microscopic particle can serve as a sensitive probe of the local environment in both biological and non-living systems. In three-dimensional space, rolling motion (i.e. longitudinal rotation) is arguably the subtlest and the most sensitive motion, generally requiring just nanoscale forces to actuate[116] – the other five degrees of freedom in motion being translations in the x, y, z directions, rotation in-plane, and rotation out-of-plane

[‡] A portion of this text has been adapted from Lee, Y.V. *et al. Nano Lett*. ASAP. DOI: 10.1021/acs.nanolett.0c00974, with permission from the American Chemical Society.

(Figure 1). We can examine how small the moment of inertia associated with the rolling motion is in relation to that associated with different types of rotations. For a thin rod with mass M, length l, and radius R:

Rotational inertias about center:

$$I = \frac{1}{12} M l^2$$

Rotational inertias about end:

$$I = \frac{1}{3} M l^2$$

Rotational inertias about its axis:

$$I = \frac{1}{2} M R^2$$

We see that the moment of inertia associated with a polar rotation is a function of the object's length squared while that of a rolling motion is a function of the object's radius squared. In case of a nanowire with 1:100 radius to length aspect ratio (similar to the nanowires used in the reported experiments), the torque of rolling motion is more three orders of magnitude smaller than that of in-plane rotation. Furthermore, compared to translations or planar rotations, rolling motion generally involves the least amount of free space, such that we are more likely to observe rolling motion in a crowded environment where other motions are constrained.

Tools to track rolling motion utilize either an optical or a structural asymmetry. In 2005, Yajima and Cross introduced a side arm (structural asymmetry) to a microtubule to

experimentally observe microtubule rotation induced by kinesin.[117] Following this, Yajima *et al* tracked microtubule rotation with higher precision by labeling microtubules with nanocrystals (optical asymmetry) and tracking the rotation with a three-dimensional microscopy.[118] The Yu group tracked the rolling motion of dual fluorescent labeled (optically asymmetric) Janus rods (~ 500 nm in diameter) bound to endosomes to study the rotational dynamics of endosomes during intracellular transport [119] and to study how the distribution of ligands on the Janus particle surface affects the cellular internalization process.[120] In a study of rolling motion in a non-living system, the Biswal group introduced a kink (structural asymmetry) in a chain of DNA-linked colloids (~1 μm diameter) and studied how the no-slip boundary condition affects the rolling diffusivity.[121] While these methods yield measurements of rolling motion with high precision, their applications are limited by the probes' significant thicknesses and complex fabrication.

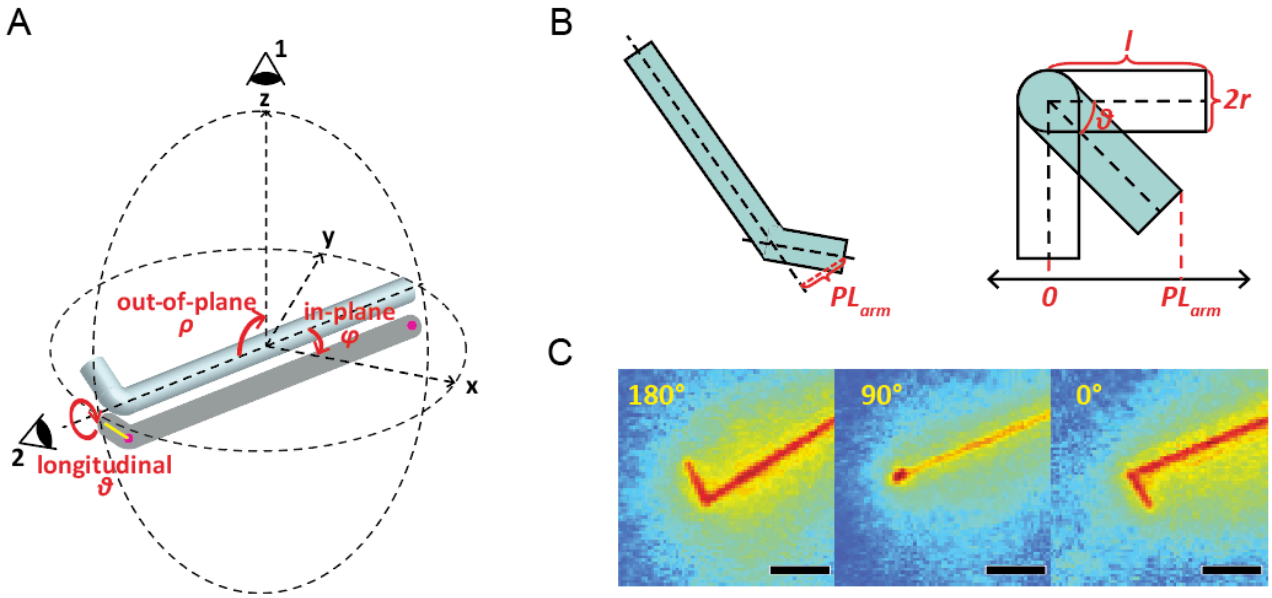

Figure 5-1. Overview of the rolling tracking method. A. Schematic diagram of a kinked silicon nanowire with its projection (gray) on the detection plane (xy plane). The nanowire can translate in three directions (x, y, z) and rotate longitudinally (θ), in-plane (φ), and out-of-plane (ρ). In the experiments, translation in z-axis and rotation out-of-plane are negligible, B. right: schematic diagram of the kinked silicon nanowire from the top (perspective 1 in A), left: schematic diagram of the arm (perspective 2 in A) with the arm length (l), apparent thickness

(2r), and longitudinal orientation (θ) annotated in red. C. Optical microscope images of a kinked silicon nanowire in different longitudinal orientations, Scale bar: 2 μm.

Here, we introduce a new method for tracking the rolling motion of a nanoscale L-shaped particle that is both structurally and optically robust, easy to synthesize, and synthetically tunable. Specifically, we track the rolling motion of a kinked nanowire by measuring the projected lengths of the nanowire arm on the microscope detection plane (Figure 5-1). While reminiscent of the bent microtubule, silicon nanowires provide better structural stability and tunable rigidity.

Given their high scattering efficiency, silicon nanowires can be seen in low magnification using either dark or bright field microscopy. Furthermore, since they do not require fluorescence staining, fluorescence measurements can be reserved for orthogonal measurements. In addition, they are synthesized in one-step *via* the vapor-liquid-solid growth mechanism using a chemical vapor deposition system to display a wide range of lengths, morphologies,[11,12,122] and thicknesses, from a few nanometers to a few micrometers. Most importantly, the option to have a narrow (i.e. small thickness) nanowire significantly expands our experimental toolset because it makes the probe sensitive to small mechanical perturbations as shown in the nanowire's cellular uptake [123] and intercellular force study.[36]

In our method, a short arm (structural asymmetry) is grown at the end of a straight nanowire to serve as a marker in tracking the wire's longitudinal orientation (θ). As the nanowire rotates along its long axis, the projected length of the arm (PL_{arm}) on the microscope detection plane changes according to Eq.1, where $\theta = 0°$ is defined as the orientation in which the arm lies parallel to the detection plane (Figure 5-1).

$$\boldsymbol{PL_{arm} = l\cos\theta + r\sin\theta} \quad \textbf{(Equation 5-1)}$$

While the projected length of the arm varies according to the θ, the actual length of the arm ($\boldsymbol{l}$) and the apparent radius of the nanowire (r) are measured constants (Methods and Materials). Longitudinal orientations are obtained by solving Equation 5-1.

As a proof of concept, we apply our technique to study the longitudinal rotation of a kinked nanowire floating in media with no cell contact and a cell-interacting kinked nanowire. We demonstrate that while the nanowire exhibits thermally activated (i.e. Brownian) random rolling motion in solution, the nanowire exhibits super- and sub-diffusive rolling motions when in contact with a mammalian cell.

5.2 Results

5.2.1 Non-interacting Experiment

To test the sensitivity of our tracking tool in a neutral setting, we let the nanowire float in a two-dimensional cell culture, where the nanowire had no interaction with the cell (Video S1). As it is crucial to have our nanowire stay in the focal plane of the microscope, we let the nanowire settle near the bottom of the substrate, where the out-of-plane rotation or z-axis translocation is minimized. (Methods and Materials) We quantified the nanowire's rotational dynamics by fitting the mean squared angular displacements in the longitudinal axis ($MSAD_{longitudinal}$) to a power function (Equation 5-2) with the anomalous exponent (α) and the diffusivity coefficient (D) (Figure 5-2 C, D).

$$\langle(\boldsymbol{\theta(t)} - \boldsymbol{\theta_0})^2\rangle = \boldsymbol{Dt^{\alpha}} \qquad \textbf{(Equation 5-2)}$$

Here, θ_0 is the longitudinal orientation of the nanowire at a reference frame, and $\theta(t)$ is that at a time *t* from the reference frame.

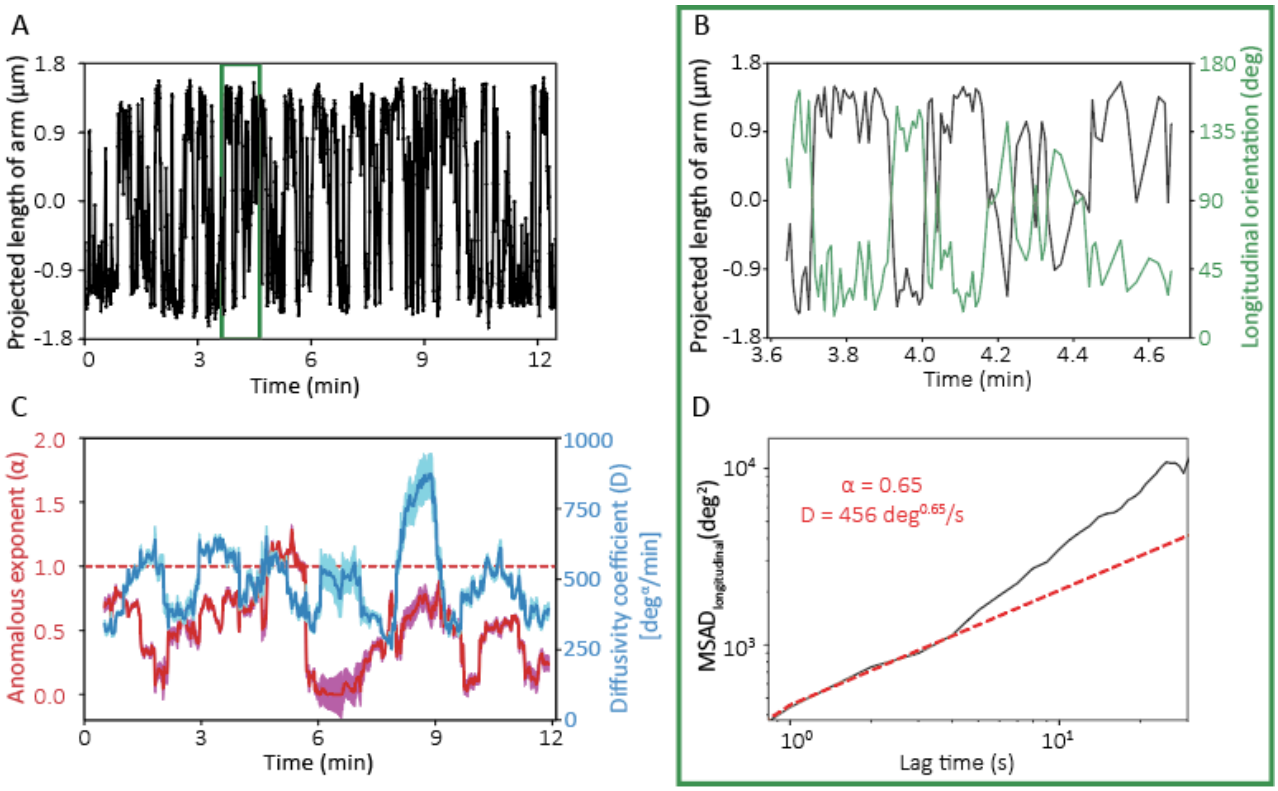

Figure 5-2. Extracting the rolling motion from the raw data. A. PL_{arm} vs. time plot from the non-interacting nanowire experiment, 100 data points (green box) are used to demonstrate how they are processed in B and D. B. PL_{arm} (black) and longitudinal orientation (green) vs. time plot of the 100 data points, C. Anomalous exponent (red) and diffusivity coefficient (blue) vs. time plots of the entire data shown in A with their respective errors bars (magenta, cyan), D. $MSAD_{longitudinal}$ vs. lag time of the 100 data points.

The non-interacting nanowire (Figure 5-2, Figure 5-3) showed a rapid and random rolling motion as characterized by the large diffusivity coefficient throughout the video (Figure 5-2 C, (Video S1). As expected, the rolling motion was much more conspicuous than the nanowire's translational or in-plane rotational motions. The predominantly sub-diffusive (i.e. $\alpha < 1$) rolling motion may be due to the movement of the nanowire in and out of the extracellular matrix or a no slip boundary condition. The variation in the anomalous exponent shown in Figure 5-2 C suggests that the nanowire was positioned in an inhomogeneous environment.

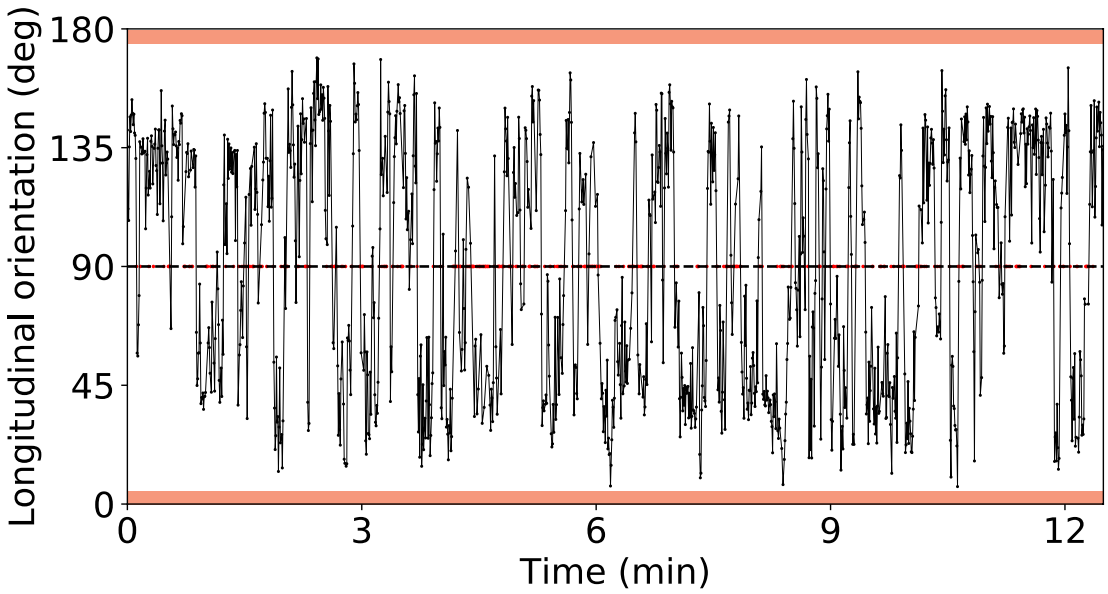

Figure 5-3. Longitudinal orientation trajectory of a non-interacting nanowire. The longitudinal orientation vs. time plot of the entire free-floating nanowire experiment. The red dots along the 90° horizontal line indicate the indices of removed frames due to either being ambiguous (when the nanowire is oriented near 0° or 180°) or being shadowed by the nanowire main body (when the nanowire is oriented near 90°). The red regions near 0° and 180° indicate the range where data points are removed to prevent under-estimation of the longitudinal rotation. For example, if the nanowire rotates from 358 ° to 3° (5 degrees of rotation), it will appear to have rotated from 2° to 3° (1 degree of rotation). Of note, these frames are already discarded as they also fall in the ambiguous region.

5.2.2 Cell-interacting Experiment

Next, we investigated the probe's ability to detect force from its environment by tracking the rolling motion of the nanowire upon interaction with a human umbilical vein endothelial cell (HUVEC), which is known to internalize silicon nanowires.[123] For the purposes of demonstrating our new method, we were interested in probing how the cellular behavior affects the probe's rolling dynamics. Based on the fact that the nanowire did not overlap with the cell's nucleus when fully encompassed (Videos S2, S3, S4) and HUVEC's tendency to internalize silicon nanowires,[123] we assume that the probe was internalized by the cell as opposed to lying on the membrane outside the cell. From its first contact with the cell to its complete internalization by the cell, the nanowire displayed a variety of longitudinal rotational behaviors, which were

sequentially categorized into three phases: *contact*, *static*, and *dynamic*. In the contact phase (0 - 8 min), the cell and the nanowire had their initial contact at the end of the nanowire's main body (Figure 5-4 i). The cell then encompassed the nanowire's main body, and subsequently the nanowire arm (Figure 5-4 ii – iv). In the static phase (8 - 42 min), once the nanowire was completely internalized, it displayed a negligible amount of longitudinal rotation. This *static* phase persisted for about 80 minutes. In the dynamic phase (110 - 122 min), the cell vigorously contracted and expanded, which induced the nanowire to roll (Videos S2, S3, S4).

In the static phase, the nanowire maintained an orientation, where its arm lay parallel to the cell culture substrate (i.e. 180°). In contrast, in the *contact* and *dynamic* phases, the nanowire underwent unidirectional super diffusive rolling motions (Figure 5-4). For example, in the *contact* phase, the anomalous exponent of the $MSAD_{longitudinal}$ increased to 1.61 ± 0.04. The observed active rolling of the nanowire is reminiscent of the active in-plane rotation of a Au nanorod observed during its endocytosis reported by Chen *et al*.,[124] suggesting the role of angular reorientation of the particle during the internalization process. In the *dynamic* phase, the nanowire also displayed a roughly unidirectional rotation, with the maximum anomalous exponent reaching 1.69 ± 0.05 upon cell contraction/expansion and migration. While the nanowires displayed randomness in rotational direction in every step for both experiments, the cell-interacting nanowire rolled much more slowly than the non-interacting nanowire as shown by the cell-interacting nanowire's diffusivity coefficients, which were two to three orders of magnitude smaller. The extreme sluggishness observed can be explained by the probe being stuck on the substrate at first (Figure 5-4 i) then by being inside the crowded cytoplasmic network.[125]

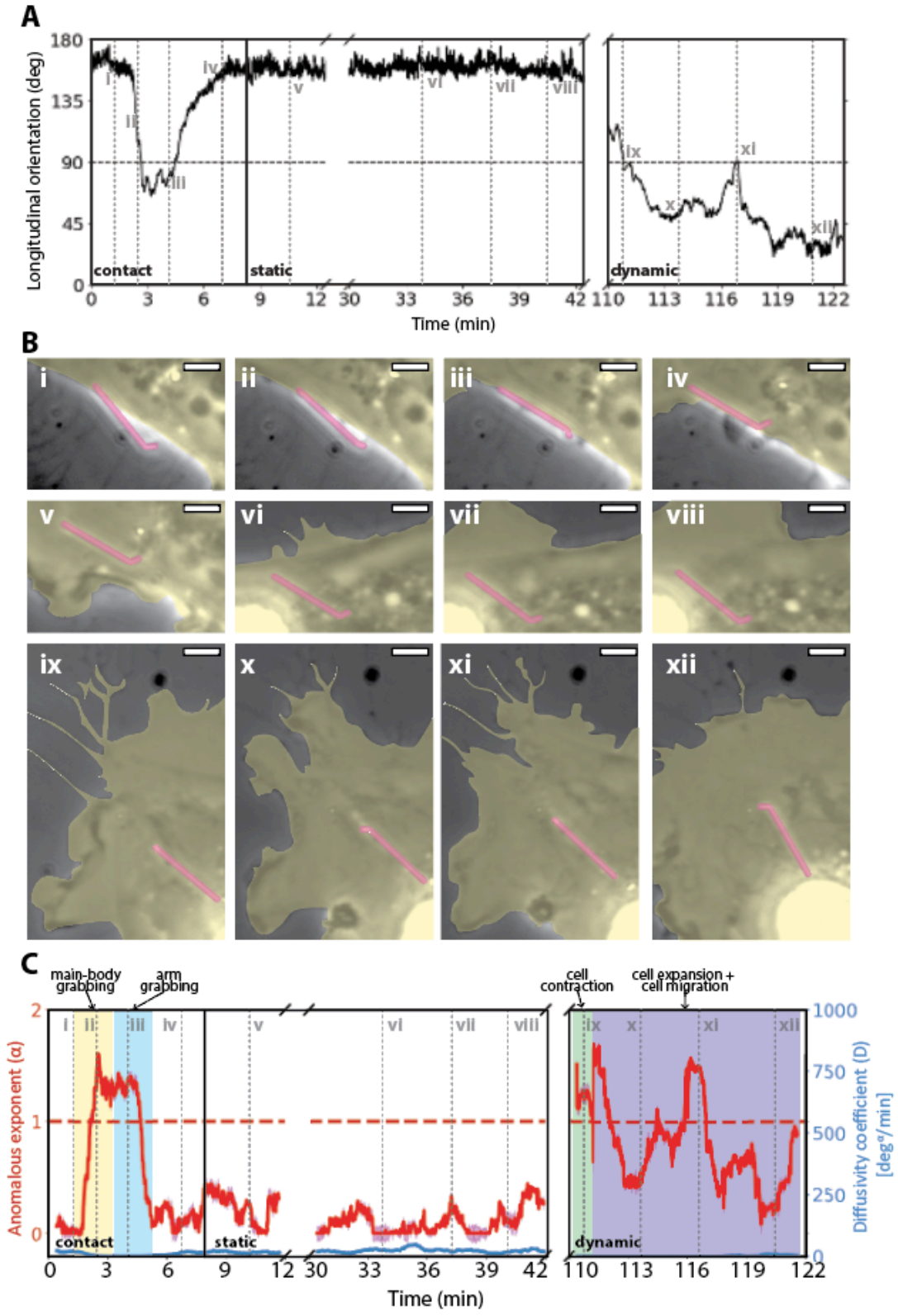

Figure 5-4. Nanowire-cell interacting experiments. A. Longitudinal orientation vs. time plots of three sequential experiments of the same nanowire interacting with the same cell, B. Time

(**Figure 5-4 continued)** series of optical microscope images, falsely colored are the cell (yellow) and the nanowire (pink), Note that the nanowire underwent in-plane orientation and translocated within the cell over the 70 minutes period between viii to ix during when the cell gradually moved and its membrane ruffled. Scale bar: 4 μm, C. Anomalous exponent (red) and diffusivity coefficient (blue) vs. time plots for the cell-interacting parts. Errors (magenta for anomalous exponent fitting error, cyan for diffusivity coefficient fitting error) are reported. Color blocks highlight different cellular behaviors: cell encompassing the nanowire main body (yellow), cell encompassing the nanowire arm (blue), cell contracting (green), cell expanding and migrating (purple); Roman numerals in A, B, and C indicate the same time points.

5.2.3 Discussion

We have demonstrated that our nanowire is a uniquely sensitive motional probe, which can potentially be used to measure torque acting on nanoparticles. Similar to the rotational probes used for measuring the DNA mechanics,[126] one can calculate the associated rotational inertia of microscopic particles based on their rolling dynamics with an additional parameter, the nanowire thickness. The thickness can be measured by taking the scattering spectrum as demonstrated in Figure 5-5..[127]

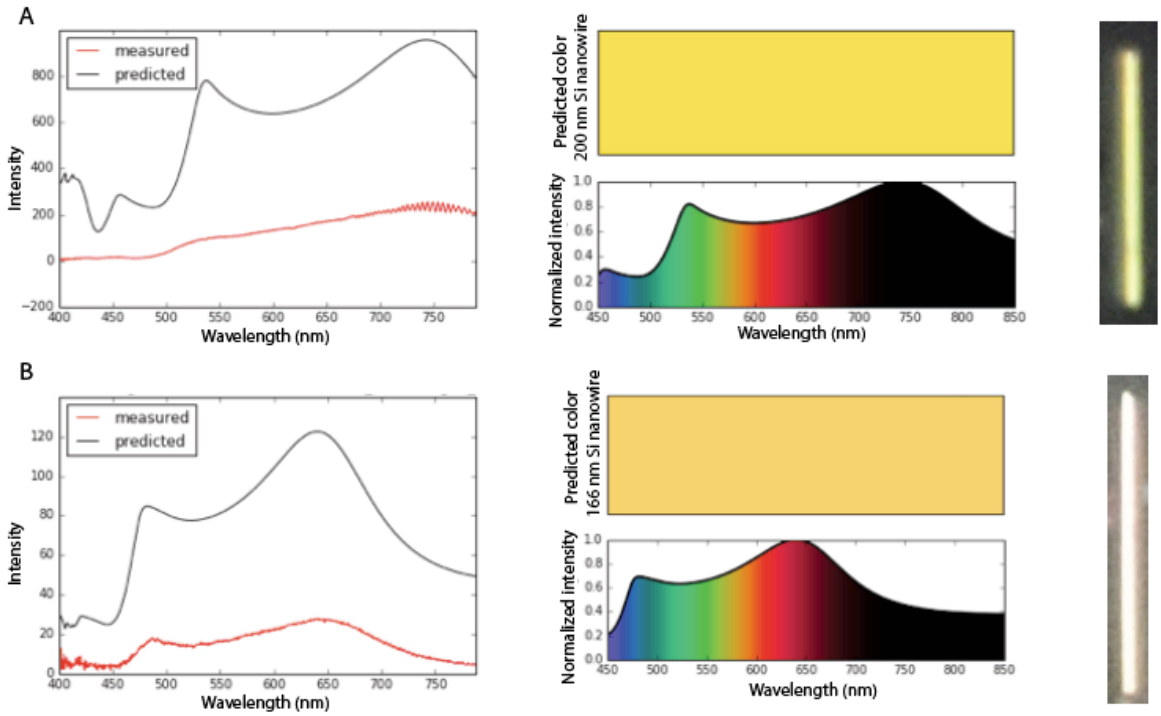

Figure 5-5. Nanowire thickness measurement. Using Fergie spectroscopy (Princeton Instrument), attached to the same microscope setup, we measured the nanowire thickness based

(**Figure 5-5 continued)** on the analysis illustrated in ref. 17 in the main text. Thickness of the probe can be measured concurrently with the video acquisition. Two sets of data are presented in panel A and B. In each panel, right is the measured spectrum and the closest matching calculated spectrum plotted over wavelength. In the middle are the calculated spectrum (bottom) and the color based on spectrum (top). On the right is a colored photography (iPhone6) taken through the microscope's eyepiece that matches the predicted color.

Depending on the system of interest, one can leverage the synthetic flexibility of crystalline SiNWs by tailoring the structural parameters – i.e. the length of the main body, the length of the arm, thickness of the nanowire, and the angle between the arm and the main body. For example, thin short nanowires offer greater sensitivity and locality than longer and thicker nanowires; however, thin nanowires can be bent even by intracellular forces,[36] which may complicate the interpretation of the rolling motion. It should be noted that the arm itself could alter the dynamics of the nanowire, as it is not an innocent observer. A large enough arm will cause the rolling motion of the nanowire to deviate from its straight counterpart, and therefore introduce artifacts. In our nanowire-cell interaction experiment, the arm of the probe caused the probe to remain predominantly in the 180° orientations where the arm stayed parallel to the substrate (Figure 5-4 A). In a two-dimensional culture, HUVECs are 3.5 μm thick at most near their nuclei and spread as thin as 200 *nm* at their peripheries.[123,128] Given the 1.7 μm long arm, the nanowire would have had no room to keep its arm upright near the cell periphery. In contrast, when the cell contracted drastically in the beginning of the *dynamic* phase (Video S4), the nanowire started to roll conspicuously as the bulged up interior of the cell provided enough space for the arm to roll around inside the cell. When the cell expanded again, thus flattening out, the nanowire went back to its parallel longitudinal orientation (i.e. near 0°).

The ability of our probe to reflect different cellular behaviors (e.g. nanowire internalization, contraction, expansion) suggests its potential use in different fields, including biophysics, hydrodynamics, and self-assembly. As a biological example, when studying the

health effects of airborne particulate matter, the particulates' rotational dynamics in different parts of the body such as the mucus lining of the lungs, the blood stream, and in individual cells will affect how the particulates translocate, accumulate, and are processed by the human body.[129,130] Within the field of self-assembly, researchers have tracked the translational diffusion dynamics of particles to determine how the interparticle forces play a role in different organizational processes.[131] It stands to reason that when studying the assembly processes of anisotropic particles– whether the anisotropy is in the particles' surface makeup or structure – researchers can now track particles' longitudinal rotational diffusion, and assess their role in interparticle dynamics and self-assembly. In fact, rolling motions played an integral role for ferromagnetic colloids that collectively show flocking and vortex phenomena.[114,132,133]

These proof-of-concept demonstrations now open the door for in-depth studies on nanoparticle-cell interactions with statistically significant sample sizes to draw biophysically relevant conclusions. For example, the unidirectional rolling motion in the *contact* phase (Figure 5-4) suggests that endocytotic mechanisms may exhibit rolling motions, which may either be due to cytoskeleton mechanics or perhaps rotations in membrane receptors.[134]

In this chapter, we have presented a new method of tracking nanoscale rolling motion using a kinked-nanowire. We developed the *Gaussian centerline detection* algorithm and utilized principal component analysis (Chapter 3) to detect the longitudinal rotation of the nanowire efficiently and precisely. In our non-interacting experiment, we observed how predominant longitudinal rotation is among other rotational and translational motions. And in the cell-interacting experiment, we demonstrated the probe's sensitivity to impart changes in a cellular environment (Figure 5-6). Given the biocompatibility,[123,135,136] the broad structural diversity, and

the simple experimental setup, we believe our kinked SiNW method will better equip researchers across many fields.

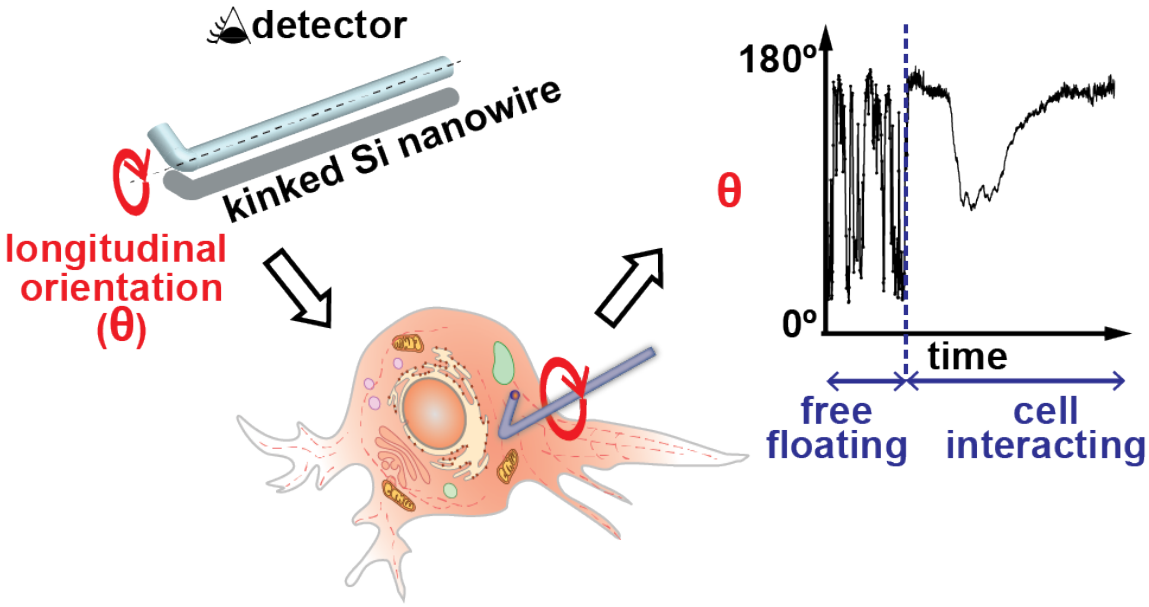

Figure 5-6. Schematic summarizing the rotational tracking method. Left: The projected view of the kinked SiNW is observed by the detection. Middle: The nanowire interacts with the cell. Right: Conspicuous difference is observed between the nanowire's rolling motions during its free-floating phase and cell-interacting phase.

5.2.4 Methods and Materials

Kinked-nanowires synthesis. Kinked SiNW were synthesized via the vapor-liquid-solid mechanism, using gold nanocrystals as catalysts. Au nanoparticles with 50 nm diameters (TedPella, diluted 9x with 10% HF solution) were deposited onto a Si <100> substrate (Nova Electronic Materials, n-type). The nanowire growth was carried out at 480 °C, and 40 torr in a home-built chemical vapor deposition system. Silane (SiH_4) was used as the Si source, hydrogen (H_2) as a carrier gas, and phosphine (PH_3, 1000 ppm in H_2) as the n-dopant source. SiH_4, H_2, and PH_3 were flown in at the rate of 60, 2, and 2 standard cubic centimeters per minute, respectively. To introduce a kink, the system was purged toward the based pressure of about 1 mTorr in between the growth of the arm and the main body part. The growth order was as follows: arm

growth for 45 s, system purge for 15 s, main body growth for 25 min, system purge for 15 s, and arm growth for 45 s. This synthesis resulted in nanowires with one or two kinks at each ends. Note, not all purge steps successfully introduced a kink. Nanowires used in the experiments had only one kink because nanowires often break at some part of the main body upon sonication, leaving only one kink per NW. Resulting nanowires were polydisperse: their diameters ranged from $10\ nm\ to\ 200\ nm$ (Figure 5-7).

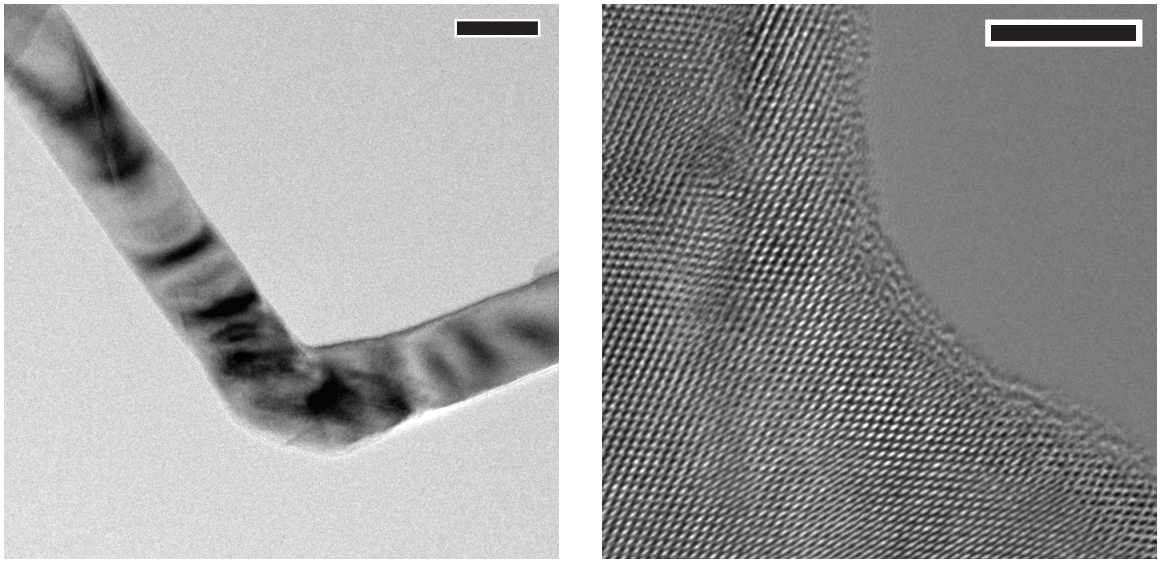

Figure 5-7. Transmission electron microscopy images of the kinked portion of the kinked SiNW. Left scale bar: 50 nm; right scale bar: 5 nm.

Cell culture. Human umbilical vein endothelial cells (HUVEC) were cultured using M200 growth media (Life Technologies) with Low Serum Growth Supplement (Thermo Fisher) and Antibiotic-Antimycotic (Thermo Fisher). Cell cultures were stored at 37°C and under 5% CO_2 in a sterile incubator. Cells at passage seven were used for the experiment.

Experiment setup. Because 3D motions of a nanowire complicate the tracking, we settled the nanowires near the substrate bottom or placed the nanowires in contact with a cell that was lying flat; this suppressed any significant out-of-plane rotations. We confirmed that the nanowire

remained in pseudo 2D space by measuring its body length: if the nanowire remains in the two-dimensional space, the projected length of the nanowire's main body part should be constant. (Table **5-2**)

i. Non-interacting case. The nanowire floated in media on top of the extracellular matrix: Nanowire-M200 media mixture was freshly prepared by sonicating the SiNWs into the media. After the original media was aspirated, the prepared nanowire-media mixture (~400 μL) was added to the cell culture in a 35 mm plastic Petri dish. The dish was placed in a preheated microincubator installed on the microscope. Videos of the nanowires were taken within the first five hours after the nanowire-media mixture was added. Due to the considerable time (> 3 hr) it takes for the nanowires to settle to the bottom of the dish, no observed nanowires were in contact with the cells on the bottom of the dish.

ii. Cell-interacting case. The nanowire was in contact with a HUVEC. Twenty-four hours prior to the experiment, the nanowire-media mixture (~400 μL) was added to an empty 35 mm Petri dish. The dish was stored in the 37°C sterile incubator overnight to allow the nanowires to settle at the bottom of the dish. On the day of the experiment, HUVEC were thawed and resuspended in the M200 media (1.4 mL). After aspirating media in the dish, leaving the nanowires behind, we seeded the HUVEC. We placed the dish inside a microincubator and started acquiring data immediately. Seeding the cells on top of the settled nanowires, as opposed to the other way around, ensures interaction between nanowire and cell, as the heavy cells settle down much faster than the nanowires.

Data acquisition. Videos of the nanowire motions were acquired using an IX71 inverted microscope (Olympus) and ORCA-R2 CCD (Hamamatsu) detector. During the data acquisition, the magnification of the objective lens was matched to pixel size such that the nanowire covered

at least five pixels in the longitudinal dimension, sufficient for Nyquist sampling [137]. Videos were acquired in two channels. We recorded the first channel in the scatter-enhanced phase contrast (SEPC) mode for visualizing both the cells and the nanowires [36]. In the SEPC mode, we used both the internal lamp and the LED-144-YK ring LED lamp (Amscope) mounted around the condenser. We recorded the second channel in the scatter-enhanced pseudo darkfield (SEPD) mode for visualizing only the nanowires. Here, only the ring LED lamp was turned on; turning off the internal lamp, thus minimizing signal from the cells, facilitated the nanowire detection in the data processing stage. During data acquisition, the sample dishes were kept inside an INUB-ONICS-F1 stage top microincubator (Tokai Hit, 37 °C, 5% CO2).

Image analysis (PL_{arm} detection). This process is explained in detail in Chapter 4.

Determination of the arm length and the nanowire thickness. As shown in Figure 5-1, the arm length (l) and the nanowire thickness (r) are the two measured parameters involved in the determination of the nanowire's longitudinal orientation based on the projected length of arm. For consistent data processing, we determine the two parameters in a systematic and logical way.

i. Determination of the nanowire's apparent radius (r). The nanowire radius is determined by taking the average of the absolute values of the measured radius of every frame in a video. In each frame, the radius is measured to be the maximum distance between the Gaussian centerline coordinates near the main-body end and the principal component. For consistency when processing multiple videos of the same nanowire, the minimum value of the nanowire radius from the videos is used. We use the minimum value because the measured value is likely to be an overestimation of the true radius.

ii. Determination of the arm length (l).

$$\boldsymbol{l = \sqrt{PL_{arm,max}{}^2 - r^2}} \qquad \textbf{(Equation 5-3)}$$

First, the top 1% of the largest absolute values of PL_{arm} are removed from the list of PL_{arm}. The removal of the largest values ensures removal of falsely large detections of PL_{arm}. Next, the largest of the remaining PL_{arm} is defined to be the $PL_{arm,max}$. Finally, the arm length can be calculated based on Equation 5-3. When more than one video of the same sample is taken, the largest of $PL_{arm,max}$ determined from each video is used as the $PL_{arm,max}$ for all the videos. Also, we make sure that the nanowires are oriented near their parallel orientations (near 0° or 180°) at least once in the observed time.

Calculation (Converting PL_{arm} to longitudinal rotation). We solved Equation 5-1 in the main text to convert PL_{arm} to longitudinal orientation. Based on the longitudinal orientations, we calculated longitudinal rotation. We defined the nanowire longitudinal orientation to range between 0° and 180° because we cannot distinguish whether the nanowire arm is pointing towards or away from the detector. To track rolling motion, we are interested in the relative orientations of the nanowire; therefore, our approach is not affected by an absence of absolute orientation measurements.

In order to prevent underestimation due to confining the $\theta(t)$ to span between 0° and 180°, we fit the $MSAD_{longitudinal}$ up to t = 0.5 s where the plot increases monotonically, meaning the observed time period is shorter than the relaxation time. Depending on the study in question, different ways of fitting the parameters can be considered, as discussed by Wu and Berland [138,139]. A particle's rotations can deviate from normal diffusion (α=1) to either super-diffusion (α>1) or sub-diffusion (α<1). In intracellular settings, these anomalous diffusions are often observed. For example, particles like organelles and vesicles undergo super-diffusive translations

when they are actively transported by molecular motors [140], actin, and microtubules in cytoplasm [141,142]. Particles also undergo sub-diffusive translations in a crowded environment or when they interact with stationary organelles [143,144]. Less attention has been paid to rotational motion compared to translational motion due to technical limitations of measuring rotation, but we expect to see non-normal diffusive behavior with rotation. While the diffusivity coefficient (D) roughly corresponds to the instantaneous speed of the rotation, a direct comparison of the diffusivity coefficient (D) is less meaningful than a direct comparison of the anomalous exponent due to the varying unit (deg^{α}/s), while the alpha parameter is unit-less.

Error Analysis. Based on the analysis of immobilized nanowires, we measured the 95% confidence interval of the projected length of the arm to be ± 0.66 pixels, which corresponds to ± 67 nm. This tracking inaccuracy translates to inaccuracy in longitudinal orientation according to Equation 5-1. Next, we calculated that the fitting errors associated with the anomalous exponents and the diffusivity coefficients were insignificant, as shown in the Figure 5-2 C and Figure 5-4 C.

Table 5-1 Fitting errors

Experiment	Anomalous exponent (α)	Diffusivity coefficient (D).
Free-floating	0.079 (13%)	66 (13%)
Cell-interacting	0.061 (11%)	0.90 (14%)

Values in the table are 95% confidence intervals (relative to the average values). The errors in fitting the $MSAD_{longitudinal}$ to $D\Delta t^{\alpha}$ were calculated for the two fitting parameters, anomalous exponent (α) and the diffusivity coefficient (D). We calculated the standard deviation errors by taking the square root of the covariance, which is given from scipy.optimize.curve_fit function in Python. We are reporting the two parameters' errors only when their anomalous exponent is

greater than 0.2. For a non-rolling nanowire, characterized by an anomalous exponent of less than 0.2, our model ($\mathrm{MSAD}_{\mathrm{longitudinal}} = D\Delta t^{\alpha}$) is inadequate because the $\mathrm{MSAD}_{\mathrm{longitudinal}}$ may not be monotonically increasing.

Table 5-2. Measurement of pseudo-two-dimensional confinements**.**

Experiment	MB average (μm)	MB SD (μm)	Maximum observed out-of-plane rotation (deg)
Free-floating	34.91	0.15	7.50
Cell-interacting_A	12.039	0.096	10.21
Cell-interacting_B	11.991	0.065	8.42
Cell-interacting_C	11.958	0.144	12.52

In order to determine whether the nanowire stays in the pseudo-two-dimensional space, we kept track of the projected length of the nanowires' main-body part (MB). Based on the negligible fluctuations in the length, we concluded that the two nanowires underwent minimal out-of-plane rotations, and stayed in pseudo-two-dimensional spaces.

For the free-floating experiment, the projected length of the nanowire's main-body was $34.91 \pm 0.15 \mu m$. To determine the maximum observed out-of-plane rotation, we first assumed the actual MB length to be the average MB length plus the standard deviation: 35.06 μm. Then, we considered the minimum observed main-body part length, which is the average MB length minus the standard deviation of 34.76 μm. Based on these assumptions, we concluded that the maximum out-of-plane rotation is 7.5 degrees for the free-floating experiment.

Similarly, the relevant observed MB lengths and the calculated out-of-plane rotations of each experiment are reported in the table. Note that these out-of-plane rotations are over-

estimations, as the standard deviation of the main-body lengths are within the detection fluctuations of the experiment. For example, the average main-body length varies by more than $0.1\mu m$ among the cell-interacting cases, which uses the same nanowire. The individual main-body length standard deviations are less than 0.1 μm.

6 Conclusion and Outlook

Insights gleaned from nanomaterials-based light energy conversion can be adapted to designs of biomodulation devices. Due to their size- and shape-dependent optical properties and excellent synthetic control, nanomaterials have shown unique technological advantages as the light absorbers or energy transducers. Biocompatible Si nanomaterials have also been incorporated into biological systems including biomolecules, bacteria and eukaryotic cells for a large collection of fundamental studies and applications.

6.1 Ultra-thin Nanowire Formation & Restructuring

In chapter 3, I introduced a method to grow ultra-thin hair-like nanowire branches with diameters mostly under 15 nm, that are populated close together within 200 nm of each other, forming a band of hair-like nanowires around a primary nanowire. This method enables researchers to control the overall and local surface area-to volume ratio of the structure because the band of nanobranches with high surface area-to-volume ratio can be introduced at different positions along the primary nanowire (Figure 3-8). One can imagine various fundamental studies using these nanostructures with varying degrees of surface area-to-volume by region.

In latter part of chapter 3, I show that subjecting these nanowires to annealing or shell growth conditions causes restructuring of the hair-like nanowire branches that can decrease the surface area-to-volume ratio, and more importantly, homogenize the overall structure and surface smoothness. Having a homogeneously structured nanoprobe with a clean and smooth surface is necessary when conducting biophysical experiments as variations in the probe can introduce artifacts in already variable biological systems. Furthermore, such homogeneous ensemble nanomaterials with anisotropic features (i.e. spheroids) can be used to study the effect of particles' anisotropy on various assembly processes .

6.2 Rod-like Particle Detection & Rotation Tracking Method

In chapter 4 and 5, I introduced the newly developed method to experimentally track the rolling motion using a kinked-nanowire along with the computational algorithms to efficiently process the tracking data. With the tracking method, one can track and analyze all six degrees of freedom in motion, which are translational motions in x-, y-, z-axis, azimuthal and polar rotations, and rotation along the long axis (i.e. rolling). The complete analysis of motion can be coupled with other photo-transducing ability of Si nanowires. For example, by having the tracking probe with a p-i-n core-shell structure, one can study the mechanical effect on phototransduction simultaneously.

Nano-bio interfaces is a rapidly growing area of research, and it promises to serve as a powerful tool for both fundamental biophysical studies and clinical applications. Looking forward, scientific advances in nanomaterial synthesis and experimental characterization may be integrated to promote further innovations in clinics and laboratories.

7 References

1. B Sakmann & Neher, and E. Patch Clamp Techniques for Studying Ionic Channels in Excitable Membranes. *Annual Review of Physiology* **46**, 455–472 (1984).

2. Prohaska, O. J., Olcaytug, F., Pfundner, P. & Dragaun, H. Thin-Film Multiple Electrode Probes: Possibilities and Limitations. *IEEE Transactions on Biomedical Engineering* **BME-33**, 223–229 (1986).

3. Grinvald, A. & Hildesheim, R. VSDI: a new era in functional imaging of cortical dynamics. *Nature Reviews Neuroscience* **5**, 874–885 (2004).

4. Rochefort, N. L., Jia, H. & Konnerth, A. Calcium imaging in the living brain: prospects for molecular medicine. *Trends in Molecular Medicine* **14**, 389–399 (2008).

5. Bantscheff, M., Schirle, M., Sweetman, G., Rick, J. & Kuster, B. Quantitative mass spectrometry in proteomics: a critical review. *Anal Bioanal Chem* **389**, 1017–1031 (2007).

6. Juskowiak, B. Nucleic acid-based fluorescent probes and their analytical potential. *Anal Bioanal Chem* **399**, 3157–3176 (2011).

7. Peng, H. *et al.* DNAzyme-Mediated Assays for Amplified Detection of Nucleic Acids and Proteins. *Anal. Chem.* **90**, 190–207 (2018).

8. Williams, D. A., Fogarty, K. E., Tsien, R. Y. & Fay, F. S. Calcium gradients in single smooth muscle cells revealed by the digital imaging microscope using Fura-2. *Nature* **318**, 558–561 (1985).

9. Parameswaran, R. & Tian, B. Rational Design of Semiconductor Nanostructures for Functional Subcellular Interfaces. *Accounts of Chemical Research* **51**, 1014–1022 (2018).

10. Tian, B., Xie, P., Kempa, T. J., Bell, D. C. & Lieber, C. M. Single-crystalline kinked semiconductor nanowire superstructures. *Nature Nanotechnology* **4**, 824–829 (2009).

11. Kim, S. *et al.* Designing Morphology in Epitaxial Silicon Nanowires: The Role of Gold, Surface Chemistry, and Phosphorus Doping. *ACS Nano* **11**, 4453–4462 (2017).

12. Luo, Z. *et al.* Atomic gold–enabled three-dimensional lithography for silicon mesostructures. *Science* **348**, 1451–1455 (2015).

13. Tian, B. *et al.* Coaxial silicon nanowires as solar cells and nanoelectronic power sources. *Nature* **449**, 885–889 (2007).

14. Jiang, Y. *et al.* Heterogeneous silicon mesostructures for lipid-supported bioelectric interfaces. *Nature Materials* **15**, 1023–1030 (2016).

15. The Nobel Prize in Physics 1956. https://www.nobelprize.org/nobel_prizes/physics/laureates/1956/.

16. Ho, J. C. *et al.* Controlled nanoscale doping of semiconductors via molecular monolayers. *Nature Mater* **7**, 62–67 (2008).

17. Gao, X. P. A., Zheng, G. & Lieber, C. M. Subthreshold Regime has the Optimal Sensitivity for Nanowire FET Biosensors. *Nano Lett.* **10**, 547–552 (2010).

18. Jiang, Z., Qing, Q., Xie, P., Gao, R. & Lieber, C. M. Kinked p–n Junction Nanowire Probes for High Spatial Resolution Sensing and Intracellular Recording. *Nano Lett.* **12**, 1711–1716 (2012).

19. Cui, Y., Wei, Q., Park, H. & Lieber, C. M. Nanowire Nanosensors for Highly Sensitive and Selective Detection of Biological and Chemical Species. *Science* **293**, 1289–1292 (2001).

20. Cohen-Karni, T., Timko, B. P., Weiss, L. E. & Lieber, C. M. Flexible electrical recording from cells using nanowire transistor arrays. *PNAS* **106**, 7309–7313 (2009).

21. Tian, B. *et al.* Three-Dimensional, Flexible Nanoscale Field-Effect Transistors as Localized Bioprobes. *Science* **329**, 830–834 (2010).

22. Hahm, J. & Lieber, C. M. Direct Ultrasensitive Electrical Detection of DNA and DNA Sequence Variations Using Nanowire Nanosensors. *Nano Lett.* **4**, 51–54 (2004).

23. Patolsky, F. *et al.* Electrical detection of single viruses. *PNAS* **101**, 14017–14022 (2004).

24. Zheng, G., Patolsky, F., Cui, Y., Wang, W. U. & Lieber, C. M. Multiplexed electrical detection of cancer markers with nanowire sensor arrays. *Nature Biotechnology* **23**, 1294–1301 (2005).

25. Anand, A. *et al.* Detection of K+ Efflux from Stimulated Cortical Neurons by an Aptamer-Modified Silicon Nanowire Field-Effect Transistor. *ACS Sens* **2**, 69–79 (2017).

26. Vessman, J. *et al.* Selectivity in analytical chemistry (IUPAC Recommendations 2001). *Pure and Applied Chemistry* **73**, 1381–1386 (2001).

27. Patolsky, F. *et al.* Detection, Stimulation, and Inhibition of Neuronal Signals with High-Density Nanowire Transistor Arrays. *Science* **313**, 1100–1104 (2006).

28. Patolsky, F., Zheng, G. & Lieber, C. M. Fabrication of silicon nanowire devices for ultrasensitive, label-free, real-time detection of biological and chemical species. *Nature Protocols* **1**, 1711–1724 (2006).

29. Lee, H.-S., Kim, K. S., Kim, C.-J., Hahn, S. K. & Jo, M.-H. Electrical detection of VEGFs for cancer diagnoses using anti-vascular endotherial growth factor aptamer-modified Si nanowire FETs. *Biosens Bioelectron* **24**, 1801–1805 (2009).

30. Munje, R. D., Muthukumar, S., Selvam, A. P. & Prasad, S. Flexible nanoporous tunable electrical double layer biosensors for sweat diagnostics. *Scientific Reports* **5**, 14586 (2015).

31. Chu, C.-H. *et al.* Beyond the Debye length in high ionic strength solution: direct protein detection with field-effect transistors (FETs) in human serum. *Scientific Reports* **7**, 5256 (2017).

32. Lafaurie-Janvore, J. *et al.* ESCRT-III Assembly and Cytokinetic Abscission Are Induced by Tension Release in the Intercellular Bridge. *Science* **339**, 1625–1629 (2013).

33. Moore, S. W., Roca-Cusachs, P. & Sheetz, M. P. Stretchy Proteins on Stretchy Substrates: The Important Elements of Integrin-Mediated Rigidity Sensing. *Developmental Cell* **19**, 194–206 (2010).

34. Natkanski, E. *et al.* B Cells Use Mechanical Energy to Discriminate Antigen Affinities. *Science* **340**, 1587–1590 (2013).

35. Yusko, E. C. & Asbury, C. L. Force is a signal that cells cannot ignore. *Mol Biol Cell* **25**, 3717–3725 (2014).

36. Zimmerman, J. F. *et al.* Free-Standing Kinked Silicon Nanowires for Probing Inter- and Intracellular Force Dynamics. *Nano Lett.* **15**, 5492–5498 (2015).

37. Tian, B. *et al.* Macroporous nanowire nanoelectronic scaffolds for synthetic tissues. *Nat Mater* **11**, 986–994 (2012).

38. Dai, X., Zhou, W., Gao, T., Liu, J. & Lieber, C. M. Three-dimensional mapping and regulation of action potential propagation in nanoelectronics-innervated tissues. *Nature Nanotechnology* **11**, 776–782 (2016).

39. Lewis, N. S. Research opportunities to advance solar energy utilization. *Science* **351**, aad1920–aad1920 (2016).

40. Kayes, B. M., Atwater, H. A. & Lewis, N. S. Comparison of the device physics principles of planar and radial p-n junction nanorod solar cells. *Journal of Applied Physics* **97**, 114302 (2005).

41. Boettcher, S. W. *et al.* Photoelectrochemical Hydrogen Evolution Using Si Microwire Arrays. *J. Am. Chem. Soc.* **133**, 1216–1219 (2011).

42. McKone, J. R. *et al.* Evaluation of Pt, Ni, and Ni–Mo electrocatalysts for hydrogen evolution on crystalline Si electrodes. *Energy Environ. Sci.* **4**, 3573–3583 (2011).

43. Lewis, N. S. Developing a scalable artificial photosynthesis technology through nanomaterials by design. *Nature Nanotechnology* **11**, 1010–1019 (2016).

44. Tian, B., Kempa, T. J. & Lieber, C. M. Single nanowire photovoltaics. *Chem. Soc. Rev.* **38**, 16–24 (2008).

45. Kempa, T. J. *et al.* Coaxial multishell nanowires with high-quality electronic interfaces and tunable optical cavities for ultrathin photovoltaics. *PNAS* **109**, 1407–1412 (2012).

46. Amirav, L. & Alivisatos, A. P. Photocatalytic Hydrogen Production with Tunable Nanorod Heterostructures. *J. Phys. Chem. Lett.* **1**, 1051–1054 (2010).

47. Walter, M. G. *et al.* Solar Water Splitting Cells. *Chem. Rev.* **110**, 6446–6473 (2010).

48. Dasgupta, N. P. & Yang, P. Semiconductor nanowires for photovoltaic and photoelectrochemical energy conversion. *Frontiers of Physics* **9**, 289–302 (2014).

49. Wilker, M. B., Schnitzenbaumer, K. J. & Dukovic, G. Recent Progress in Photocatalysis Mediated by Colloidal II-VI Nanocrystals. *Israel Journal of Chemistry* **52**, 1002–1015 (2012).

50. Lian, S., Kodaimati, M. S., Dolzhnikov, D. S., Calzada, R. & Weiss, E. A. Powering a CO2 Reduction Catalyst with Visible Light through Multiple Sub-picosecond Electron Transfers from a Quantum Dot. *J. Am. Chem. Soc.* **139**, 8931–8938 (2017).

51. Olshansky, J. H., Ding, T. X., Lee, Y. V., Leone, S. R. & Alivisatos, A. P. Hole Transfer from Photoexcited Quantum Dots: The Relationship between Driving Force and Rate. *J. Am. Chem. Soc.* **137**, 15567–15575 (2015).

52. Wu, K. & Lian, T. Quantum confined colloidal nanorod heterostructures for solar-to-fuel conversion. *Chem. Soc. Rev.* **45**, 3781–3810 (2016).

53. Harris, R. D. *et al.* Electronic Processes within Quantum Dot-Molecule Complexes. *Chem. Rev.* **116**, 12865–12919 (2016).

54. Vijselaar, W. *et al.* Spatial decoupling of light absorption and catalytic activity of Ni–Mo-loaded high-aspect-ratio silicon microwire photocathodes. *Nature Energy* **3**, 185–192 (2018).

55. Yang, J. *et al.* A multifunctional biphasic water splitting catalyst tailored for integration with high-performance semiconductor photoanodes. *Nature Materials* **16**, 335–341 (2017).

56. Segev, G., Beeman, J. W., Greenblatt, J. B. & Sharp, I. D. Hybrid photoelectrochemical and photovoltaic cells for simultaneous production of chemical fuels and electrical power. *Nature Materials* **17**, 1115–1121 (2018).

57. Antognazza, M. R., Abdel Aziz, I. & Lodola, F. Use of Exogenous and Endogenous Photomediators as Efficient ROS Modulation Tools: Results and Perspectives for Therapeutic Purposes. *Oxidative Medicine and Cellular Longevity* https://www.hindawi.com/journals/omcl/2019/2867516/ (2019) doi:https://doi.org/10.1155/2019/2867516.

58. Son, J. *et al.* Light-responsive nanomedicine for biophotonic imaging and targeted therapy. *Advanced Drug Delivery Reviews* **138**, 133–147 (2019).

59. Xie, C. *et al.* Noninvasive Neuron Pinning with Nanopillar Arrays. *Nano Lett.* **10**, 4020–4024 (2010).

60. Santoro, F. *et al.* Revealing the Cell–Material Interface with Nanometer Resolution by Focused Ion Beam/Scanning Electron Microscopy. *ACS Nano* **11**, 8320–8328 (2017).

61. Qi, S., Yi, C., Ji, S., Fong, C.-C. & Yang, M. Cell adhesion and spreading behavior on vertically aligned silicon nanowire arrays. *ACS Appl Mater Interfaces* **1**, 30–34 (2009).

62. Lou, H.-Y., Zhao, W., Zeng, Y. & Cui, B. The Role of Membrane Curvature in Nanoscale Topography-Induced Intracellular Signaling. *Acc. Chem. Res.* **51**, 1046–1053 (2018).

63. Tsai, D., Sawyer, D., Bradd, A., Yuste, R. & Shepard, K. L. A very large-scale microelectrode array for cellular-resolution electrophysiology. *Nature Communications* **8**, 1–11 (2017).

64. Prodanov, D. & Delbeke, J. Mechanical and Biological Interactions of Implants with the Brain and Their Impact on Implant Design. *Front Neurosci* **10**, (2016).

65. Hochberg, L. R. *et al.* Neuronal ensemble control of prosthetic devices by a human with tetraplegia. *Nature* **442**, 164–171 (2006).

66. *Neuroscience*. (Sinauer Associates, 2001).

67. Cesare, P., Moriondo, A., Vellani, V. & McNaughton, P. A. Ion channels gated by heat. *Proc Natl Acad Sci U S A* **96**, 7658–7663 (1999).

68. El Hady, A. & Machta, B. B. Mechanical surface waves accompany action potential propagation. *Nature Communications* **6**, 6697 (2015).

69. Pappas, T. C. *et al.* Nanoscale Engineering of a Cellular Interface with Semiconductor Nanoparticle Films for Photoelectric Stimulation of Neurons. *Nano Lett.* **7**, 513–519 (2007).

70. Parameswaran, R. *et al.* Photoelectrochemical modulation of neuronal activity with free-standing coaxial silicon nanowires. *Nature Nanotechnology* **13**, 260–266 (2018).

71. Parameswaran, R. *et al.* Optical stimulation of cardiac cells with a polymer-supported silicon nanowire matrix. *PNAS* **116**, 413–421 (2019).

72. Mathieson, K. *et al.* Photovoltaic retinal prosthesis with high pixel density. *Nature Photonics* **6**, 391–397 (2012).

73. Tang, J. *et al.* Nanowire arrays restore vision in blind mice. *Nature Communications* **9**, 786 (2018).

74. Zhu, L., Gao, M., Peh, C. K. N. & Ho, G. W. Solar-driven photothermal nanostructured materials designs and prerequisites for evaporation and catalysis applications. *Mater. Horiz.* **5**, 323–343 (2018).

75. Feng, F. *et al.* Highly Efficient Photothermal Effect by Atomic-Thickness Confinement in Two-Dimensional ZrNCl Nanosheets. *ACS Nano* **9**, 1683–1691 (2015).

76. Halas, N. J. & Nordlander, P. Plasmon-induced hot carrier science and technology. *Nature Nanotechnology* **10**, 25–34 (2015).

77. Atwater, H. A. & Polman, A. Plasmonics for improved photovoltaic devices. *Nature Materials* **9**, 205–213 (2010).

78. Nguyen, S. C. *et al.* Study of Heat Transfer Dynamics from Gold Nanorods to the Environment *via* Time-Resolved Infrared Spectroscopy. *ACS Nano* **10**, 2144–2151 (2016).

79. Hogan, N. J. *et al.* Nanoparticles Heat through Light Localization. *Nano Lett.* **14**, 4640–4645 (2014).

80. Yong, J. *et al.* Gold-Nanorod-Assisted Near-Infrared Stimulation of Primary Auditory Neurons. *Advanced Healthcare Materials* **3**, 1862–1868 (2014).

81. Richter, C.-P., Rajguru, S. & Bendett, M. Infrared neural stimulation in the cochlea. *Proc SPIE* **8565**, 85651Y (2013).

82. Shapiro, M. G., Homma, K., Villarreal, S., Richter, C.-P. & Bezanilla, F. Infrared light excites cells by changing their electrical capacitance. *Nature Communications* **3**, (2012).

83. Albert, E. S. *et al.* TRPV4 channels mediate the infrared laser-evoked response in sensory neurons. *Journal of Neurophysiology* **107**, 3227–3234 (2012).

84. Carvalho-de-Souza, J. L. *et al.* Photosensitivity of Neurons Enabled by Cell-Targeted Gold Nanoparticles. *Neuron* **86**, 207–217 (2015).

85. Carvalho-de-Souza, J. L., Pinto, B. I., Pepperberg, D. R. & Bezanilla, F. Optocapacitive Generation of Action Potentials by Microsecond Laser Pulses of Nanojoule Energy. *Biophysical Journal* **114**, 283–288 (2018).

86. Pastoriza-Santos, I., Kinnear, C., Pérez-Juste, J., Mulvaney, P. & Liz-Marzán, L. M. Plasmonic polymer nanocomposites. *Nature Reviews Materials* **3**, 375–391 (2018).

87. Schild, H. G. Poly(N-isopropylacrylamide): experiment, theory and application. *Progress in Polymer Science* **17**, 163–249 (1992).

88. Sutton, A. *et al.* Photothermally triggered actuation of hybrid materials as a new platform for *in vitro* cell manipulation. *Nature Communications* **8**, 14700 (2017).

89. Hanson, L. *et al.* Vertical nanopillars for *in situ* probing of nuclear mechanics in adherent cells. *Nature Nanotechnology* **10**, 554–562 (2015).

90. Roder, P. B., Smith, B. E., Davis, E. J. & Pauzauskie, P. J. Photothermal Heating of Nanowires. *J. Phys. Chem. C* **118**, 1407–1416 (2014).

91. Charles, A. C., Merrill, J. E., Dirksen, E. R. & Sandersont, M. J. Intercellular signaling in glial cells: Calcium waves and oscillations in response to mechanical stimulation and glutamate. *Neuron* **6**, 983–992 (1991).

92. Hwang, S.-W. *et al.* A Physically Transient Form of Silicon Electronics. *Science* **337**, 1640–1644 (2012).

93. Zimmerman, J. F. & Tian, B. Nongenetic Optical Methods for Measuring and Modulating Neuronal Response. *ACS Nano* **12**, 4086–4095 (2018).

94. Musin, I. R., Boyuk, D. S. & Filler, M. A. Surface chemistry controlled diameter-modulated semiconductor nanowire superstructures. *Journal of Vacuum Science & Technology B* **31**, 020603 (2013).

95. Gaboriau, D. *et al.* Silicon nanowires and nanotrees: elaboration and optimization of new 3D architectures for high performance on-chip supercapacitors. *RSC Advances* **6**, 81017–81027 (2016).

96. Jun, K. & Jacobson, J. M. Programmable Growth of Branched Silicon Nanowires Using a Focused Ion Beam. *Nano Letters* **10**, 2777–2782 (2010).

97. Doerk, G. S., Ferralis, N., Carraro, C. & Maboudian, R. Growth of branching Si nanowires seeded by Au–Si surface migration. *Journal of Materials Chemistry* **18**, 5376 (2008).

98. Tian, B., Xie, P., Kempa, T. J., Bell, D. C. & Lieber, C. M. Single-crystalline kinked semiconductor nanowire superstructures. *Nature Nanotech* **4**, 824–829 (2009).

99. Doerk, G. S., Radmilovic, V. & Maboudian, R. Branching induced faceting of Si nanotrees. *Appl. Phys. Lett.* **96**, 123117 (2010).

100. Hannon, J. B., Kodambaka, S., Ross, F. M. & Tromp, R. M. The influence of the surface migration of gold on the growth of silicon nanowires. *Nature* **440**, 69–71 (2006).

101. Sivakov, V. A. *et al.* Silicon nanowire oxidation: the influence of sidewall structure and gold distribution. *Nanotechnology* **20**, 405607 (2009).

102. Kim, B. J. *et al.* Au Transport in Catalyst Coarsening and Si Nanowire Formation. *Nano Lett.* **14**, 4554–4559 (2014).

103. Nagashima, K., Yanagida, T., Oka, K., Tanaka, H. & Kawai, T. Mechanism and control of sidewall growth and catalyst diffusion on oxide nanowire vapor-liquid-solid growth. *Appl. Phys. Lett.* **93**, 153103 (2008).

104. Lotty, O. *et al.* Self-Seeded Growth of Germanium Nanowires: Coalescence and Ostwald Ripening. *Chem. Mater.* **25**, 215–222 (2013).

105. Dubrovskii, V. G. *et al.* Diffusion-induced growth of GaAs nanowhiskers during molecular beam epitaxy: Theory and experiment. *Phys. Rev. B* **71**, 205325 (2005).

106. Zhu, Y. *et al.* From nanowires to nanoislands: Morphological evolutions of erbium silicide nanostructures formed on the vicinal Si(001) surface. *Journal of Applied Physics* **100**, 114312 (2006).

107. Ham, H., Park, N.-H., Kim, S. S. & Kim, H. W. Evidence of Ostwald ripening during evolution of micro-scale solid carbon spheres. *Scientific Reports* **4**, 1–4 (2014).

108. Madras, P., Dailey, E. & Drucker, J. Kinetically Induced Kinking of Vapor−Liquid−Solid Grown Epitaxial Si Nanowires. *Nano Lett.* **9**, 3826–3830 (2009).

109. Chen, Y. *et al.* Controlling Kink Geometry in Nanowires Fabricated by Alternating Metal-Assisted Chemical Etching. *Nano Lett.* **17**, 1014–1019 (2017).

110. Wu, Y. *et al.* Controlled Growth and Structures of Molecular-Scale Silicon Nanowires. *Nano Lett.* **4**, 433–436 (2004).

111. Brönstrup, G. *et al.* Optical Properties of Individual Silicon Nanowires for Photonic Devices. *ACS Nano* **4**, 7113–7122 (2010).

112. Qu, X., Wu, D., Mets, L. & Scherer, N. F. Nanometer-localized multiple single-molecule fluorescence microscopy. *PNAS* **101**, 11298–11303 (2004).

113. Nguyen, U. T. V., Bhuiyan, A., Park, L. A. F. & Ramamohanarao, K. An effective retinal blood vessel segmentation method using multi-scale line detection. *Pattern Recognition* **46**, 703–715 (2013).

114. Kumar, N., Soni, H., Ramaswamy, S. & Sood, A. K. Flocking at a distance in active granular matter. *Nat Commun* **5**, 4688 (2014).

115. Pieuchot, L. *et al.* Cellular Subcompartments through Cytoplasmic Streaming. *Developmental Cell* **34**, 410–420 (2015).

116. Falvo, M. R. *et al.* Nanometre-scale rolling and sliding of carbon nanotubes. *Nature* **397**, 236–238 (1999).

117. Yajima, J. & Cross, R. A. A torque component in the kinesin-1 power stroke. *Nature Chemical Biology* **1**, 338–341 (2005).

118. Yajima, J., Mizutani, K. & Nishizaka, T. A torque component present in mitotic kinesin Eg5 revealed by three-dimensional tracking. *Nat Struct Mol Biol* **15**, 1119–1121 (2008).

119. Gao, Y. *et al.* Single-Janus Rod Tracking Reveals the "Rock-and-Roll" of Endosomes in Living Cells. *Langmuir* (2017) doi:10.1021/acs.langmuir.7b02804.

120. Gao, Y. & Yu, Y. How Half-Coated Janus Particles Enter Cells. *Journal of the American Chemical Society* **135**, 19091–19094 (2013).

121. Li, D., Fakhri, N., Pasquali, M. & Biswal, S. L. Axial Thermal Rotation of Slender Rods. *Phys. Rev. Lett.* **106**, 188302 (2011).

122. Tian, B., Xie, P., Kempa, T. J., Bell, D. C. & Lieber, C. M. Single-crystalline kinked semiconductor nanowire superstructures. *Nat Nano* **4**, 824–829 (2009).

123. Zimmerman, J. F. *et al.* Cellular uptake and dynamics of unlabeled freestanding silicon nanowires. *Science Advances* **2**, e1601039 (2016).

124. Chen, K. *et al.* Characteristic rotational behaviors of rod-shaped cargo revealed by automated five-dimensional single particle tracking. *Nat Commun* **8**, 1–10 (2017).

125. Weiss, M., Elsner, M., Kartberg, F. & Nilsson, T. Anomalous Subdiffusion Is a Measure for Cytoplasmic Crowding in Living Cells. *Biophysical Journal* **87**, 3518–3524 (2004).

126. Bryant, Z., Oberstrass, F. C. & Basu, A. Recent developments in single-molecule DNA mechanics. *Curr Opin Struct Biol* **22**, 304–312 (2012).

127. Brönstrup, G. *et al.* A precise optical determination of nanoscale diameters of semiconductor nanowires. *Nanotechnology* **22**, 385201 (2011).

128. Xu, K., Babcock, H. P. & Zhuang, X. Dual-objective STORM reveals three-dimensional filament organization in the actin cytoskeleton. *Nature Methods* **9**, 185–188 (2012).

129. Miller, M. R. *et al.* Inhaled Nanoparticles Accumulate at Sites of Vascular Disease. *ACS Nano* **11**, 4542–4552 (2017).

130. Choi, H. S. *et al.* Rapid translocation of nanoparticles from the lung airspaces to the body. *Nature Biotechnology* **28**, 1300–1303 (2010).

131. Powers, A. S. *et al.* Tracking Nanoparticle Diffusion and Interaction during Self-Assembly in a Liquid Cell. *Nano Lett.* **17**, 15–20 (2017).

132. Bricard, A., Caussin, J.-B., Desreumaux, N., Dauchot, O. & Bartolo, D. Emergence of macroscopic directed motion in populations of motile colloids. *Nature* **503**, 95–98 (2013).

133. Kaiser, A., Snezhko, A. & Aranson, I. S. Flocking ferromagnetic colloids. *Science Advances* **3**, e1601469 (2017).

134. Maruyama, I. N. Activation of transmembrane cell-surface receptors via a common mechanism? The "rotation model". *Bioessays* **37**, 959–967 (2015).

135. Kim, W., Ng, J. K., Kunitake, M. E., Conklin, B. R. & Yang, P. Interfacing Silicon Nanowires with Mammalian Cells. *J. Am. Chem. Soc.* **129**, 7228–7229 (2007).

136. Prinz, C. N. Interactions between semiconductor nanowires and living cells. *J. Phys.: Condens. Matter* **27**, 233103 (2015).

137. Crocker, J. C. & Grier, D. G. Methods of Digital Video Microscopy for Colloidal Studies. *Journal of Colloid and Interface Science* **179**, 298–310 (1996).

138. Wu, J. & Berland, K. M. Propagators and Time-Dependent Diffusion Coefficients for Anomalous Diffusion. *Biophysical Journal* **95**, 2049–2052 (2008).

139. Kepten, E., Weron, A., Sikora, G., Burnecki, K. & Garini, Y. Guidelines for the Fitting of Anomalous Diffusion Mean Square Displacement Graphs from Single Particle Tracking Experiments. *PLoS One* **10**, (2015).

140. Mallik, R. & Gross, S. P. Molecular Motors: Strategies to Get Along. *Current Biology* **14**, R971–R982 (2004).

141. Reverey, J. F. *et al.* Superdiffusion dominates intracellular particle motion in the supercrowded cytoplasm of pathogenic Acanthamoeba castellanii. *Sci Rep* **5**, (2015).

142. Bruno, L., Levi, V., Brunstein, M. & Despósito, M. A. Transition to superdiffusive behavior in intracellular actin-based transport mediated by molecular motors. *Phys. Rev. E* **80**, 011912 (2009).

143. Otten, M. *et al.* Local Motion Analysis Reveals Impact of the Dynamic Cytoskeleton on Intracellular Subdiffusion. *Biophysical Journal* **102**, 758–767 (2012).

144. Katz, Z. B. *et al.* Mapping translation ‘hot-spots’ in live cells by tracking single molecules of mRNA and ribosomes. *eLife* **5**, e10415 (2016).

145. Rajendran, L., Knölker, H.-J. & Simons, K. Subcellular targeting strategies for drug design and delivery. *Nature Reviews Drug Discovery* **9**, 29–42 (2010).

146. Park, J.-H. Hybrid Nanoparticles for Detection and Treatment of Cancer. *Advanced Materials* **24**, 3779–3802 (2012).

147. Biju, V. Chemical modifications and bioconjugate reactions of nanomaterials for sensing, imaging, drug delivery and therapy. *Chem. Soc. Rev.* **43**, 744–764 (2014).

8 Appendix

8.1 Supplementary Video Captions

Video S1. MovieS1_free floating_50xRT.avi: Video of the non-cell-interacting silicon nanowire taken in the bright field phase mode. The playtime is 50 x the real time. The scale can be referred by the nanowire main body length, which is 35 μm.

Video S2. MovieS2_cell interacting_50xRT.avi: Video of a cell interacting silicon nanowire taken in the bright field phase mode. This video corresponds to the 0 to 12 min of the cell interacting data presented. The playtime is 50 x the real time. The scale can be referred by the nanowire main body length, which is 12 μm.

Video S3. MovieS3_cell interacting_50xRT.avi: Video of a cell interacting silicon nanowire taken in the bright field phase mode. This video corresponds to the 30 to 42 min of the cell interacting data presented. The playtime is 50 x the real time. The scale can be referred by the nanowire main body length, which is 12 μm.

Video S4. MovieS4_cell interacting_50xRT.avi: video of a cell interacting silicon nanowire taken in the bright field phase mode. This video corresponds to the 110 to 112 min of the cell interacting data presented. The playtime is 50 x the real time. The scale can be referred by the nanowire main body length, which is 12 μm.

Note: All videos are cropped and their resolutions were compromised in the process of converting PNG files to JPEG files.

8.2 Image Analysis Algorithms

__init__.py

```
#!/usr/bin/env python

def load_user_setting(default, user):

    for k in user:
        if k not in default:
            raise Exception('Unknown key of setting: %s' % (k))

        default[k] = user[k]

    return default


def log_progress(sequence, every=None, size=None, name='Items'):

    from ipywidgets import IntProgress, HTML, VBox
    from IPython.display import display

    is_iterator = False
    if size is None:
        try:
            size = len(sequence)
        except TypeError:
            is_iterator = True
    if size is not None:
        if every is None:
            if size <= 200:
                every = 1
            else:
                every = int(size / 200)     # every 0.5%
    else:
        assert every is not None, 'sequence is iterator, set every'

    if is_iterator:
        progress = IntProgress(min=0, max=1, value=1)
        progress.bar_style = 'info'
    else:
        progress = IntProgress(min=0, max=size, value=0)
    label = HTML()
    box = VBox(children=[label, progress])
    display(box)

    index = 0
```

```
    try:
        for index, record in enumerate(sequence, 1):
            if index == 1 or index % every == 0:
                if is_iterator:
                    label.value = '{name}: {index} / ?'.format(
                        name=name,
                        index=index
                    )
                else:
                    progress.value = index
                    label.value = u'{name}: {index} / {size}'.format(
                        name=name,
                        index=index,
                        size=size
                    )
            yield record
    except:
        progress.bar_style = 'danger'
        raise
    else:
        progress.bar_style = 'success'
        progress.value = index
        label.value = "{name}: {index}".format(
            name=name,
            index=str(index or '?')
        )

    return

from .Image import *
from .Animation import *
from .GSCenter import *
from .Nanowire import *
from .NWGeometry import *
from .Simulator import *
from .Experiment import *
```

Animation.py

```
#!/usr/bin/env python

from . import *

import matplotlib.pyplot as plt
from matplotlib import animation, rc
from IPython.display import HTML

class Animation:
    '''
    Display animations (movies) from a groups of images
    '''

    def __init__(self, file_names, iterator, interval = 50):

        plt.ioff()
        self.fig = plt.figure()
        self.ims = []

        for i in log_progress(iterator, every=1):

            im = plt.imshow(plt.imread(file_names % (i)), animated=True)
            self.ims.append([im])

        self.ani = animation.ArtistAnimation(self.fig, self.ims,
                interval=50, blit=True, repeat_delay=1000)

        return


    def show(self):

        return HTML(self.ani.to_html5_video())
```

Experiment.py

```
#!/usr/bin/env python

from . import *
from .Image import *
from .Finder import *
from .Nanowire import *

import os, re, pickle
import numpy as np

class Experiment:
    '''
    A workspace to handle a folder of image files from an experiment
    using this package.
    '''

    def __init__(self, name):

        if not re.match('^[0-9a-zA-Z_]{1,16}$', name):
            raise Exception('Illigal experiment name.')

        self.name = name
        self.frames = []
        self.sequence = []

        self.kink_length = []
        self.mainbody_length = []

        return

    def load_folder(self, folder, prefix, sequence, progress = False):

        for file in (sequence if not progress else log_progress(sequence, every=1, name="Images")):

            filename = folder + '/0_original/' + prefix + file + '.png'
            image = Image.read_file(filename)

            ptname = folder + '/1_threshold/' + file + 'XY.txt'
            points = np.loadtxt(ptname).astype(int)

            nw = Nanowire(image, points)
            nw.src_name = filename
            self.frames.append(nw)

        return
```

```
    def import_images(self, prefix, sequence, progress = False):

        fdr = Finder()

        for file in (sequence if not progress else log_progress(sequence, every=1, name="Images")):

            filename = prefix + file
            image = Image.read_file(filename)
            nw = fdr.locate_nanowire(image)
            nw.src_name = prefix + file
            self.frames.append(nw)

        return


    def process_images(self, progress = False):

        i = 0

        for nw in (self.frames if not progress else log_progress(self.frames, every=1,
name='Frames')):
            try:
                nw.generate_gs_centers()
                nw.generate_geometry()
                self.kink_length.append(nw.geometry.kink_length())
                self.mainbody_length.append(nw.geometry.mainbody_length())

                self.sequence.append(i)
                i += 1

            except:
                print('Error processing frame [%d]: %s' % (i, nw.src_name))
                continue

        return



    def frame_count(self):
        return len(self.sequence)
```

```
def save(self):
    pickle.dump(self, open(self.name + '.p', 'wb'))



@staticmethod
def load(name):
    return pickle.load(open(name + '.p', 'rb'))
```

Finder.py

```
#!/usr/bin/env python

from . import *
from .Nanowire import *

import numpy as np
import matplotlib.pyplot as plt
from scipy import ndimage
from skimage.morphology import remove_small_objects

finder_default_setting = {
   'nanowire_width': 4,
   'window_margin': 20,
   'uniform_filter_size': 4,
   'gs_filter_sigma': 1.0,
   'mask_threshold': 0.5,
   'mask_region_minsize': 200,
}

class Finder:
   '''
   Find out a group of bright pixels from an image that are belonging
   to the nanowire
   '''

   def __init__(self, setting = {}):

      self.setting = load_user_setting(finder_default_setting.copy(), setting)
      return



   def locate_nanowire(self, image, plot = False, args = {}):

      setting = self.setting

      for k in args:
         if k in setting:
            setting[k] = args[k]

      self.image_raw = image

      im_data = image.data

      self.im_smoothed = im_data
```

```
self.im_mask = self.im_smoothed > setting['mask_threshold']
self.im_mask = remove_small_objects(self.im_mask, setting['mask_region_minsize'])

size = im_data.shape
self.nanowire_pixels = pixels = np.array(np.nonzero(self.im_mask))
xmin, xmax = pixels[0].min() , pixels[0].max()
ymin, ymax = pixels[1].min(), pixels[1].max()

margin = setting['window_margin']
dT = margin - xmin if margin > xmin else 0
dB = xmax + margin - size[0] if xmax + margin > size[0] else 0
dL = margin - ymin if margin > ymin else 0
dR = ymax + margin - size[1] if ymax + margin > size[1] else 0

if plot:
    plt.imshow(self.im_mask)
    print(dT, dB, dL, dR)

self.image_nanowire = self.image_raw.sub_region([
    xmin - margin + dT, xmax + margin - dB,
    ymin - margin + dL, ymax + margin - dR
])

fill_w = max([dT, dB, dL, dR])
self.image_nanowire.fill_border(fill_w)
self.nanowire = Nanowire(self.image_nanowire,
                         pixels - [[xmin - margin + dT - fill_w], [ymin - margin + dL - fill_w]])

return self.nanowire
```

GSCenter.py

```
#!/usr/bin/env python

from . import *
from . import GSCurve
from .Image import *
import numpy as np

gc_default_setting = {
   'nstep' : 18
}

class GSCenter:
   '''
   Find out the Gaussian center to the centeral lines of the nanowire projected
   from a given point
   '''

   def __init__(self, im, center, width, setting = {}):
      '''
      Get the point and the image data
      '''
      self.setting = load_user_setting(gc_default_setting, setting)

      top, bottom = center[0] - width, center[0] + width + 1
      left, right = center[1] - width, center[1] + width + 1

      self.image = Image(data = im.data[top:bottom, left:right], world_position=[top, left])
      self.center = np.array([width, width])
      self.width = width

      return


   def analyze(self, rad, plot = False):
      '''
      Calculate the gaussian center from a given group of rads
      '''
      if plot:
         plt.figure(figsize = (10,20))
         plt.subplot(211)
         self.image.show()

         fitted_centers = []
         gs_lines = []
```

```
if not isinstance(rad, list):
    rad = [rad]

x = np.arange(1-self.width, self.width, 1.0)
res= []

min_se = 100.0

'''
Scan over a group of lines (from rad list) cross this point:
  1. Get the brightness profile across this line
  2. Fit a Gaussian distribution
Find out the line with the least variance.
The gaussian center is the center of this gaussian distribution.
'''

for r in rad:
    step = np.array([np.cos(r), np.sin(r)])

    y = self.image.profile_line(self.center, step, x, plot = plot)
    popt, pconv = GSCurve.fit(x, y, p0 = [1.0, 0, 2])
    fitted = GSCurve.gen(x, popt[0], popt[1], popt[2])
    fitted_center = step * popt[1] + self.center

    if popt[2] < min_se:
        min_se = popt[2]
        min_step = step

    if plot:
        gs_lines.append({
            'image_y' : y,
            'fitted_y' : fitted,
            'se' : popt[2]
        })

        fitted_centers.append(fitted_center)

    line = [self.center - step * self.width, self.center + step * self.width]
    res.append((popt[2], fitted_center, line, x, y, fitted))

if plot:

    pts = np.array([x * min_step[0], x * min_step[1]]) + [[self.center[0]], [self.center[1]]]

    if plot:
        plt.plot(pts[1], pts[0],'r--')
```

```
        fitted_centers = np.array(fitted_centers)
        plt.scatter(fitted_centers[:,1], fitted_centers[:,0], s = 40, c='r')
        plt.scatter(self.center[1], self.center[0], s = 75, c ='b')
        plt.subplot(212)

        for gsl in gs_lines:

            if gsl['se'] - min_se < 1.0e-6: color = 'red'
            else: color = 'gray'

            plt.scatter(x, gsl['image_y'], s=40, c=color)
            plt.plot(x, gsl['fitted_y'], c=color, linewidth=2)

    return res


def fit(self, plot = False):
    '''
    Find the gaussian center
    '''
    if plot:
        plt.figure(figsize = (12,5))
        plt.subplot(121)
        self.image.show()

    self.best_rad = 0.0
    self.sigma_min = self.width * 2

    for rad in np.arange(0, np.pi, np.pi/self.setting['nstep']):

        try:
            sigma, fc, line, x0, y0, yfitted = self.analyze(rad)[0]
        except:
            continue

        if plot:
            plt.plot(line[1], line[0], 'b--')

        if sigma < self.sigma_min:
            self.best_rad = rad
            self.sigma_min = sigma
            self.gs_center = fc
            self.best_line = line

    if not hasattr(self, 'gs_center'):
```

```
    return False

if plot:
    plt.scatter(self.center[1], self.center[0], s = 40, c ='w')
    plt.scatter(self.gs_center[1], self.gs_center[0], s = 40, c ='r')

world = self.image.world_position
return [self.gs_center[0] + world[0], self.gs_center[1] + world[1]]
```

GSCurve.py

```
#!/usr/bin/env python

from scipy.optimize import curve_fit
import numpy as np

'''
Mathematical model of the gaussian distribution
'''

def gen(x, a, x0, sigma):
    return a * np.exp(-(x - x0)**2 / (2 * sigma**2))

def fit(x, y, p0):
    return curve_fit(gen, x, y, p0)
```

Image.py

```
#!/usr/bin/env python

import os
import matplotlib.pyplot as plt
import numpy as np

from . import GSCurve


class Image:
    '''
    An object to store the data of an image or part of the image
    '''

    def __init__(self, data = False, world_position = [0.0, 0.0]):
        '''
        Create the image, of a region in the image defined by the shift
        to the world position.
        '''
        if isinstance(data, np.ndarray):

            self.data = data.copy()
            self.data -= self.data.min()
            self.data /= self.data.max()

        self.world_position = np.array(world_position)

        return


    @staticmethod
    def read_file(image_file):
        '''
        Read and create image data
        '''
        if not os.path.isfile(image_file):
            raise Exception("cannot open image file [%s]." % (image_file))

        data = plt.imread(image_file)

        if len(data.shape) > 2:
            data = data[:,:,0]

        return Image(data)
```

```
def fill_border(self, d):
    '''
    Build up a buffer border by padding
    '''
    im = self.data
    h, w = im.shape
    enlarged = np.zeros(shape=(h + 2 * d, w + 2 * d))

    enlarged[0:d, 0:d] = im[0:d, 0:d]
    enlarged[0:d, d:d+w] = im[0:d,:]
    enlarged[0:d, d+w:d*2+w] = im[0:d, w-d:w]

    enlarged[d:d+h, 0:d] = im[:, 0:d]
    enlarged[d:d+h, d:d+w] = im[:,:]
    enlarged[d:d+h, d+w:d*2+w] = im[:, w-d:w]

    enlarged[d+h:d*2+h, 0:d] = im[h-d:h, 0:d]
    enlarged[d+h:d*2+h, d:d+w] = im[h-d:h,:]
    enlarged[d+h:d*2+h, d+w:d*2+w] = im[h-d:h, w-d:w]

    self.data = enlarged
    self.world_position -= [d, d]
    return


def sub_region(self, box):
    '''
    Create a new image object from a sub region
    '''
    return Image(self.data[box[0]:box[1], box[2]:box[3]], world_position = [box[0], box[2]])


def show(self):
    '''
    plot the image
    '''
    plt.imshow(self.data)
    return


def analyze_contrast(self, plot = False):
    '''
    Analyze the distrutions of the signal strength across the brightness
    for both background and nanowire
```

```
        '''
        bins = 100
        hwhm_factor = 2.0 / 2.355
        max_iter = 2
        max_bk_center = 0.6

        hist = np.histogram(self.data.flatten(), bins, range=(0, 1.0), density=True)
        x = 0.5 * (hist[1][:-1] + hist[1][1:])
        y = hist[0]

        background_models = []
        y_residue = y

        for i in range(max_iter):
            imax = y_residue.argmax()
            if imax > max_bk_center * bins: break

            bound = int(imax * 1.1) + 1
            popt, pcov = GSCurve.fit(x[:bound], y_residue[:bound], p0=[y_residue[imax], x[imax],
x[imax] * hwhm_factor])
            fitted = GSCurve.gen(x, popt[0], popt[1], popt[2])
            if popt[2] > 0.1: break

            y_residue = (y_residue - fitted).clip(min = 0)
            res= np.square(y_residue).sum() / bins
            background_models.append({ 'args': popt, 'fitted': fitted, 'residue': res })
            if res < 0.01: break;

        popt = background_models[-1]['args']
        tail = int((popt[1] + 3.0 * popt[2] + 1.0) * 0.5 * bins)
        imax  = y_residue[tail:].argmax() + tail
        bound = imax - (bins - imax) // 8

        popt_nw, pcov = GSCurve.fit(x[bound:], y_residue[bound:], \
            p0=[y_residue[imax], x[imax], (1.0 - x[imax]) * hwhm_factor])

        fitted_nw = GSCurve.gen(x, popt_nw[0], popt_nw[1], popt_nw[2])
        y_residue = (y_residue - fitted_nw).clip(min = 0)

        if plot:

            plt.figure(figsize=(12,8))
            plt.subplot(221)
            plt.imshow(self.data)

            plt.subplot(222)
```

```
        plt.bar(x=x, height=y, width=1.0/bins, color=(0.2, 0.2, 0.85, 0.25))

        plt.subplot(223)
        plt.bar(x=x, height=y, width=1.0/bins, color=(0.2, 0.2, 0.85, 0.25))

        for model in background_models:
            plt.plot(x, model['fitted'])
            #print(model['args'], model['residue'])

        last_model = background_models[-1]
        tail = (x > last_model['args'][1] + 3.0 * last_model['args'][2])

        plt.subplot(224)
        plt.bar(x=x[tail], height=y[tail], width=1.0/bins, color=(0.2, 0.2, 0.85, 0.25))
        plt.plot(x[tail], y_residue[tail])
        plt.plot(x[tail], fitted_nw[tail])

    return {
        'histogram': hist,
        'noise_models': background_models,
        'nw_model': (popt_nw, fitted_nw)
    }

def intercept(self, pts):

    Z = []

    for x, y in pts:
        X0, Y0 = int(x), int(y)
        a, b = x - X0, y - Y0

        T1 = (self.data[X0 + 1, Y0] - self.data[X0, Y0]) * a + self.data[X0, Y0]
        T2 = (self.data[X0 + 1, Y0 + 1] - self.data [X0, Y0 + 1]) * a + self.data[X0, Y0 + 1]
        Z.append((T2 - T1) * b + T1)

    return Z


def profile_line(self, center, step, n, plot = False):

    pts = np.array([n * step[0], n * step[1]]) + [[center[0]], [center[1]]]

    if plot:
        plt.plot(pts[1], pts[0],'w--')

    return self.intercept(pts.transpose())
```

Nanowire.py

```
#!/usr/bin/env python

from .Image import *
from .NWGeometry import *
from .GSCenter import *

from . import PCAFitter
from . import GSCurve

import matplotlib.pyplot as plt
import numpy as np


class Nanowire:

    def __init__(self, image, points):

        self.src_name = 'Noname'
        self.image    = Image(image.data)
        self.points   = points.copy()
        self.centers  = points.copy()   # [2, N]
        self.width    = 4
        self.geometry = False
        return


    def fill_border(self, w):
        if self.geometry is not False:
            raise Exception('Cannot fill border after calucating geometry!')

        self.image.fill_border(w)
        self.points += np.full(self.points.shape, w)
        self.centers += np.full(self.points.shape, w)
        return


    def generate_geometry(self, fraction = 1.0, plot = False, pca_args = {}):

        if fraction<1.0:
            nn = len(self.centers[0])
            signals = [self.image.data[self.centers[0][i], self.centers[1][i]]
                    for i in np.arange(nn)]

            threshold = np.sort(signals)[int(nn * fraction)]
            #print('threshold = ', threshold)
```

```
        mask = signals > threshold
        centers = np.array([self.centers[0][mask], self.centers[1][mask]])
    else:
        centers = self.centers.copy()

    self.geometry = NWGeometry(PCAFitter.process(centers, args = pca_args),
                               self.image.world_position)

    if plot:
        f, ax = plt.subplots(2,2)
        f.set_size_inches(9, 8.5)

        ax[0, 0].imshow(self.image.data, cmap='gray')

        ax[0, 1].imshow(self.image.data, cmap='gray')
        ax[0, 1].plot(self.points[1,:], self.points[0,:], 'g.')

        ax[1, 0].imshow(self.image.data, cmap='gray')
        ax[1, 0].plot(centers[1,:], centers[0,:], 'r.')

        ax[1, 1].imshow(self.image.data, cmap='gray')
        pts = self.geometry.points
        ax[1, 1].plot(pts[0][1], pts[0][0], 'ro')
        ax[1, 1].plot(pts[1][1], pts[1][0], 'go')
        ax[1, 1].plot(pts[2][1], pts[2][0], 'yo')

    sec = self.cross_section()
    self.width = int(sec[1][2]) * 2

    return


def cross_section(self, sep = 0.1, plot = False):

    pts = self.geometry.points
    direction = pts[1] - pts[0]

    n = np.arange(0.2, 0.9, sep)
    centers = np.array([n * direction[0], n * direction[1]]) + [[pts[0][0]], [pts[0][1]]]

    step = np.array([direction[1], -direction[0]])
    step /= np.sqrt(np.sum(step**2))
    n = np.arange(-10, 11, 1)

    if plot:
```

```
        plt.figure(figsize=(12,4))
        plt.subplot(121)
        self.image.show()

    values = np.zeros(len(n))

    for i in range(centers.shape[1]):
        values += self.image.profile_line(centers[:, i], step, n, plot)

    values /= centers.shape[1]
    values -= values.min()

    popt, pconv = GSCurve.fit(n, values, p0 = [1.0, 0, 2])
    fitted = GSCurve.gen(n, popt[0], popt[1], popt[2])

    if plot:
        plt.subplot(122)
        plt.plot(n, values)
        plt.scatter(n, fitted, s=20, c='r')

    return (values, popt)


def generate_gs_centers(self, plot = False):

    gcs = []

    for pt in self.points.transpose():
        gc = GSCenter(self.image, pt, self.width * 2)
        center = gc.fit()
        if not center: continue
        gcs.append(center)

    self.centers = np.array(gcs).transpose()

    if plot:
        plt.figure(figsize=(8,8))
        self.image.show()
        plt.scatter(self.points[1], self.points[0], c='w', s=5, alpha=0.2, lw = 0)
        plt.scatter(self.centers[1], self.centers[0], c='r', s=5, alpha=1.0, lw = 0)

    return
```

NWGeometry.py

```
#!/usr/bin/env python

import numpy as np

class NWGeometry:
    '''
    Object represents a nanowire from an image
    '''

    def __init__(self, points, world):
        '''
        Paramters:

        points: group of coordinates define the nanowire
                points[0] - x, y of the main-body tip
                points[1] - x, y of the kink point
                points[2] - x, y of the kink tip
        world: the shift (dx, dy) of points to the original image.
        '''
        self.points = points.copy()
        self.mainbody_endpoint = points[0].copy()
        self.kink_point = points[1].copy()
        self.kink_endpoint = points[2].copy()
        self.points.transpose()
        self.world_position = world.copy()
        return


    def mainbody(self):
        '''
        Get the vector representing the main-body
        '''
        return self.mainbody_endpoint - self.kink_point

    def mainbody_length(self):
        '''
        Get the length of the main-body
        '''
        return np.linalg.norm(self.mainbody()) + 1

    def mainbody_orient(self):
        '''
        Get the tilt angle of the main-body
        '''
        mainbody = self.mainbody()
```

```
    return np.angle(np.complex(mainbody[0], mainbody[1]))


def kink(self):
    '''
    Get the vector representing the kink
    '''
    return self.kink_endpoint - self.kink_point

def kink_length(self):
    '''
    Get the length of the kink
    '''
    return np.linalg.norm(self.kink()) + 1

def kink_orient(self):
    '''
    Get the tilt angle of the kink
    '''
    kink = self.kink()
    return np.angle(np.complex(kink[0], kink[1]))

def kink_angle(self):
    '''
    Get the angle between main-body and kink
    '''
    return self.kink_orient() - self.mainbody_orient()

def PL_length(self):
    '''
    Get the length of protrusion length of the kink
    '''
    return self.kink_length() * np.sin(self.kink_angle())
```

PCAFitter.py

```
#!/usr/bin/env python

import numpy as np
import matplotlib.pyplot as plt
from sklearn import decomposition

coords_mainbody = None
coords_kink = None

def characterize(pca_mb, pca_kk, mainbody, kink):
    '''
    locate the three points definining the nanowire from the
    given PCA vectors and identified mainbody and kink part.
    '''

    dx = pca_kk.mean_[0] - pca_mb.mean_[0]
    dy = pca_kk.mean_[1] - pca_mb.mean_[1]
    k_mb = pca_mb.components_[0][1] / pca_mb.components_[0][0]
    k_kk = pca_kk.components_[0][1] / pca_kk.components_[0][0]

    X = pca_kk.mean_[0] + (k_mb * dx - dy) / (k_kk - k_mb)
    Y = pca_kk.mean_[1] + (k_mb * dx - dy) / (k_kk - k_mb) * k_kk
    X0 = np.array([X, Y])

    Xt = pca_mb.transform(mainbody)
    Xr = pca_mb.transform([[X, Y]])
    if Xr[0,0] > 0: A = Xt[:,0].min() + 0 * abs(Xt[:,1].max()/2)
    else: A = Xt[:,0].max() - 0 * abs(Xt[:,1].max()/2)
    XA = pca_mb.inverse_transform([A, 0])

    Xt = pca_kk.transform(kink)
    Xr = pca_kk.transform([[X, Y]])
    if Xr[0,0] > 0: B = Xt[:,0].min() + 0 * abs(Xt[:,1].max()/2)
    else: B = Xt[:,0].max() - 0 * abs(Xt[:,1].max()/2)
    XB = pca_kk.inverse_transform([B, 0])

    return [XA, X0, XB]


def compute_parameters(XA, X0, XB, kl, ka):
    '''
    Calculate the rotational angles from given paramters.
    '''

    A0 = XA - X0
```

```
    B0 = XB - X0

    mb_length = np.sqrt(A0.dot(A0))
    kk_length = np.sqrt(B0.dot(B0))

    angle = np.arccos(np.dot(A0, B0) / mb_length / kk_length)

    if angle > ka: angle = ka
    if kk_length > kl: kk_length = kl

    d1 = np.sin(angle) * kk_length
    d2 = np.sin(ka)*kl
    rot = np.arccos(d1 / d2)

    A0p = np.array([-A0[1], A0[0]])
    if B0.dot(A0p)<0: rot = np.pi - rot

    return [mb_length, kk_length, angle/np.pi*180, rot/np.pi*180]


def process(points, plot = False, args = {}):
    '''
    Apply the iterative PCA fitting to categorize the given points
    into two groups. One group represent the main-body, while the
    other group is for the points in the kink part.
    '''

    # Read and customize the paramters

    mainbody_init_fraction = args['mainbody-init-fraction'] if 'mainbody-init-fraction' in args else
0.5
    tube_hwidth = args['tube-hwidth'] if 'tube-hwidth' in args else 1.00

    mainbody_cut = args['mainbody-cut'] if 'mainbody-cut' in args else 4.0
    kink_cut = args['kink-cut'] if 'kink-cut' in args else 2.0

    # Copy the given points
    pts = points.copy().transpose()

    # Determine if we should reorder the points

    box = [0.0, 0.0]
    box[0], box[1] = points[:,0].max() - points[:,0].min(), points[:,1].max() - points[:,1].min()

    if box[0] < box[1]:
        pts = pts[pts[:,1].argsort(),:]
```

```
# Build up PCA fitter and generate the initial group of points in main-body

N = pts.shape[0]
N_end = int(N * 0.5 * (1.0 - mainbody_init_fraction))
mainbody_pca = pts[N_end:N-N_end,:]
pca_mb = decomposition.PCA(n_components=2)
init_mb = mainbody_pca

# Run PCA fitting for three times, and refine the main-body group

for i in range(3):
    pca_mb.fit(mainbody_pca)
    dev = pca_mb.transform(pts)

    is_mb = np.absolute(dev[:,1]) < tube_hwidth
    mainbody = pts[is_mb]

    is_mb_pca = np.logical_and(is_mb, dev[:,0] > np.min(dev[is_mb,0]) + mainbody_cut)
    is_mb_pca = np.logical_and(is_mb_pca, dev[:,0] < np.max(dev[is_mb,0]) - mainbody_cut)
    mainbody_pca = pts[is_mb_pca]

# Remove the tip portions from the remaining group to form the initial group of kink part

is_kk = np.absolute(dev[:,1]) > tube_hwidth
i_kk_tip = np.argmax(np.absolute(dev[:,1]))

if dev[i_kk_tip, 0] > 0:
    is_kk = np.logical_and(is_kk, dev[:,0] > np.max(dev[:,0]) * mainbody_init_fraction)
else:
    is_kk = np.logical_and(is_kk, dev[:,0] < np.min(dev[:,0]) * mainbody_init_fraction)

kink_pca = pts[is_kk]
pca_kk = decomposition.PCA(n_components=2)

# Run PCA fitting for three times, refine the points in the kink part

for i in range(3):
    pca_kk.fit(kink_pca)
    dev = pca_kk.transform(pts)

    is_kk = np.absolute(dev[:,1]) < tube_hwidth
    kink = pts[is_kk]
    #print(np.min(dev[is_kk,0]), np.max(dev[is_kk,0]))

    is_kk_pca = np.logical_and(is_kk, dev[:,0] > np.min(dev[is_kk,0]) + kink_cut)
```

```
    is_kk_pca = np.logical_and(is_kk_pca, dev[:,0] < np.max(dev[is_kk,0]) - kink_cut)
    kink_pca = pts[is_kk_pca]

# Generate the geometry paramters from the PCA components and the two groups

geo = []
geo = np.array(characterize(pca_mb, pca_kk, mainbody, kink))

################################################################

# Plot the results

if plot:

    markersize = args['markersize'] if 'markersize' in args else 3

    if 'plot-center' in args:
        Cx = args['plot-center'][1]
        Cy = args['plot-center'][0]
    else:
        Cx = (pts[:,1].max() + pts[:,1].min()) * 0.5
        Cy = (pts[:,0].max() + pts[:,0].min()) * 0.5

    if 'plot-span' in args:
        Lx = args['plot-span'][1]
        Ly = args['plot-span'][0]
    else:
        Lx = (pts[:,1].max() - pts[:,1].min()) * 0.5 + 40
        Ly = (pts[:,0].max() - pts[:,0].min()) * 0.5 + 40

    f, ax = plt.subplots(2,2)
    f.set_size_inches(14, int(14.0*Ly/Lx))

    if 'plot-extra-pts' in args:
        for ia in range(0,4):
            ax[ia//2, ia%2].plot(args['plot-extra-pts'][1,:], args['plot-extra-pts'][0,:],
                '.', c='#cccccc', markersize=markersize)

    for ia in range(0,4):
        ax[ia//2, ia%2].plot(pts[:,1], pts[:,0], '.', c='#666666')
        ax[ia//2, ia%2].axis('equal')

    ax[0,1].plot(mainbody_pca[N_end:N-N_end,1], mainbody_pca[N_end:N-N_end,0], 'r.',
markersize=markersize)
    ax[0,1].plot(kink_pca[:,1], kink_pca[:,0], 'g.', markersize=markersize)
```

```
    ax[1,0].plot(mainbody[:,1], mainbody[:,0], 'r.', markersize=markersize)
    ax[1,0].plot(kink[:,1], kink[:,0], 'g.', markersize=markersize)

    ax[1,1].plot(geo[:,1], geo[:,0], 'b-')
    ax[1,1].plot(geo[:,1], geo[:,0], 'bo')

    for ia in range(0,4):
        ax[ia//2, ia%2].invert_yaxis()
        ax[ia//2, ia%2].set_xlim([Cx-Lx, Cx+Lx])
        ax[ia//2, ia%2].set_ylim([Cy+Ly, Cy-Ly])

#################################################################

global coords_mainbody, coords_kink
coords_mainbody = mainbody_pca
coords_kink = kink_pca

return geo
```

Simulator.py

```
#!/usr/bin/env python

from . import *

import scipy.misc
import matplotlib.pyplot as plt
import numpy as np
import os
from math import floor

simulator_default_setting = {

    # Geometry parameters:
    'nw_radius'   : 2,     # radius
    'nw_length'   : 200,     # length of mainbody
    'kink_length' : 35,      # length of kink
    'kink_angle'  : np.pi/4, # kink angle

    # Image parameters:
    'width'       : 350,     #
    'height'      : 350,     #
    'bk_mean'     : 0.25,    #
    'bk_sigma'    : 0.08,    #
    'nw_signal'   : 0.80,    #

    # Output:
    'output_folder'  : 'SIMULATED',
    'output_format'  : '%06d',

    # Runtime control:
    'initial_tilt'   : 0.5,
    'initial_rot'    : 0.0,
    'initial_center' : [0, 0],

    # Trajectory control:

    'trajectory_rotations': [],
    'trajectory_PLs': [],
    'trajectory_tilts': [],
    'trajectory_centers': [],

    # Ending flag
    '--end--' : ''
}
```

```
class Simulator:
    '''
    A simulator to create a group of fake images that mimic the real ones.
    The simulated images can be used for ML training, as the features are
    similar to the real images.
    '''

    def __init__(self, setting = {}):
        '''
        Create the simulator with the settings, where the default values are
        list above.
        '''

        self.setting = load_user_setting(simulator_default_setting, setting)
        s = self.setting

        # Mainbody on the x axis, repeat for length, tile for width --> N*W array
        self.NW = np.stack([
            np.repeat(np.arange(0, int(round(s['nw_length']))), s['nw_radius'] * 2 + 1),
            np.tile(np.arange(-s['nw_radius'], s['nw_radius'] + 1), int(round(s['nw_length'])))
        ])

        # Kink
        self.KK = np.stack([
            np.repeat(np.arange(0, int(round(s['kink_length']))), s['nw_radius'] * 2 + 1),
            np.tile(np.arange(-s['nw_radius'], s['nw_radius'] + 1), int(round(s['kink_length'])))
        ])

        self.center = [[s['width'] / 2], [s['height'] / 2]]

        return



    def run(self, progress = False):
        '''
        Run the simulation with given settings.

        Parameter: progress - if showing progress bar on the screen.
        '''

        s = self.setting
        nw_angle, nw_center = s['initial_tilt'], s['initial_center']

        # check input
```

```
    if s['trajectory_PLs'] != [] and s['trajectory_rotations'] != []:
        raise Exception('[trajectory_PLs] and [trajectory_rotations] cannot be set at the same
time.')

    elif s['trajectory_PLs'] == [] and s['trajectory_rotations'] == []:
        raise Exception('One of [trajectory_PLs] or [trajectory_rotations] must be set.')

    elif s['trajectory_PLs'] != []:
        usingPL = True
        nstep = len(s['trajectory_PLs'])

    else:
        usingPL = False
        nstep = len(s['trajectory_rotations'])

    if nstep != len(s['trajectory_tilts']):
        raise Exception('[trajectory_tilts] has wrong size.')

    if nstep != len(s['trajectory_centers'][0]):
        raise Exception('[trajectory_centers] has wrong size.')

    # prepare folder

    if not os.path.isdir(s['output_folder']):
        os.mkdir(s['output_folder'])

    # start simulation

    for i in range(nstep) if not progress else log_progress(range(nstep), every=1,
name="Steps"):

        if usingPL:
            angle = s['kink_angle']
            ratio = 1.0

        else:
            y = np.sin(s['kink_angle']) * np.cos(s['trajectory_rotations'][i]) # DC' line/ AC
            x = np.cos(s['kink_angle'])                                        # AD line / AC
            ratio = np.sqrt(y*y + x*x)                                         # AC'/AC
            angle = np.arctan2(y, x)                                           # Angle(BAC'))

        NW, KK = self.gen_nw(ratio, angle,
                             s['trajectory_tilts'][i],
                             s['trajectory_centers'][:, i])

        # Generate NW image
```

```
        self.save_image(NW, i)

    return


def gen_nw(self, projected_ratio, projected_angle, tilt_angle, center):
    '''
    Generate the coordinates of signals (bright points) of a nanowire
    from the given geometry.
    '''

    s = self.setting
    kink_angle, nw_length = s['kink_angle'], s['nw_length']

    # Build up kink part

    T = [[  np.cos(projected_angle), np.sin(projected_angle)],
         [ -np.sin(projected_angle), np.cos(projected_angle)]]

    KK = self.KK.copy()
    KK[0] = KK[0] * projected_ratio
    KK = np.matmul(T, KK)

    # Connect kink part to mainbody

    NW = self.NW.copy()
    NW = np.concatenate([NW, KK], axis=1)
    NW = NW + [[ -nw_length / 2], [0.0]]

    # In-plane rotation

    T = [[  np.cos(tilt_angle), np.sin(tilt_angle)],
         [ -np.sin(tilt_angle), np.cos(tilt_angle)]]

    NW = np.matmul(T, NW)

    # Update in-plane difussion

    NW = NW + [[center[0]], [center[1]]]
    NW += self.center

    return NW, KK
```

```
    def save_image(self, NW, idx = 0):
        '''
        Apply a filters to create random background noises and Gaussian Blur
        to the bright region of nanowires. Save the image with the given index
        number.
        '''

        s = self.setting
        wnd_w, wnd_h = s['width'], s['height']

        bk = np.random.normal(loc = s['bk_mean'], scale = s['bk_sigma'], size = (wnd_h, wnd_w))

        fk = np.zeros([wnd_h, wnd_w])
        for i in np.arange(0, NW.shape[1]):
            fk[int(round(NW[1][i]))][int(round(NW[0][i]))] = s['nw_signal'] * 1.5

        fk = scipy.ndimage.uniform_filter(fk, size = 4)

        image = fk + bk

        scipy.misc.toimage(image).save(('%s/' + self.setting['output_format'] + '.png') %
(self.setting['output_folder'], idx))

        return
```